



UvA-DARE (Digital Academic Repository)

Quantitative and localized spectroscopy for non-invasive bilirubinometry in neonates

Bosschaart, N.

Publication date

2012

Document Version

Final published version

[Link to publication](#)

Citation for published version (APA):

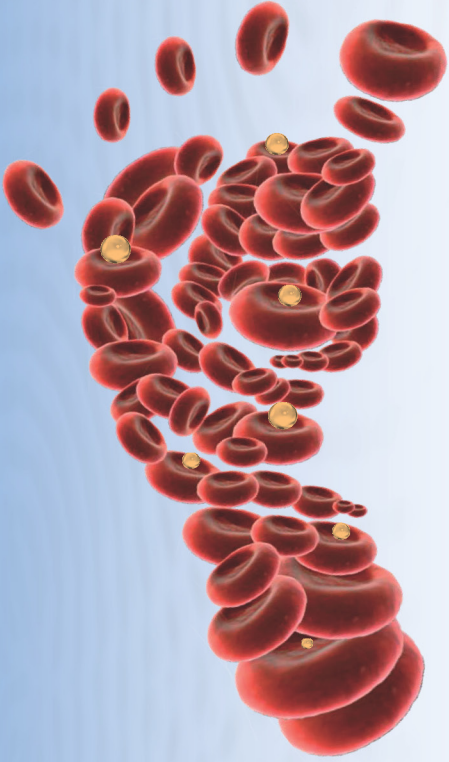
Bosschaart, N. (2012). *Quantitative and localized spectroscopy for non-invasive bilirubinometry in neonates*. [Thesis, fully internal, Universiteit van Amsterdam].

General rights

It is not permitted to download or to forward/distribute the text or part of it without the consent of the author(s) and/or copyright holder(s), other than for strictly personal, individual use, unless the work is under an open content license (like Creative Commons).

Disclaimer/Complaints regulations

If you believe that digital publication of certain material infringes any of your rights or (privacy) interests, please let the Library know, stating your reasons. In case of a legitimate complaint, the Library will make the material inaccessible and/or remove it from the website. Please Ask the Library: <https://uba.uva.nl/en/contact>, or a letter to: Library of the University of Amsterdam, Secretariat, P.O. Box 19185, 1000 GD Amsterdam, The Netherlands. You will be contacted as soon as possible.



Quantitative and localized spectroscopy for non-invasive bilirubinometry in neonates

———— Nienke Bosschaart

Quantitative and localized spectroscopy for non invasive bilirubinometry in neonates

Nienke Bosschaart

**Quantitative and localized spectroscopy for non-invasive
bilirubinometry in neonates**

Nienke Bosschaart

Quantitative and localized spectroscopy for non-invasive bilirubinometry in neonates
PhD thesis, University of Amsterdam, The Netherlands

The research described in this thesis was supported by the Vernieuwings-impuls program (AGT07547) of the Netherlands Organization of Scientific Research (NWO) and the Technology Foundation STW.

Printing of this thesis was kindly sponsored by:



Ocean Optics, Inc.

Author: Nienke Bosschaart

ISBN: 978-94-6182-065-5

Printing: Off Page, www.offpage.nl

Copyright 2012 © Nienke Bosschaart, Amsterdam, The Netherlands. All rights reserved. No part of this publication may be reproduced, stored in a retrieval system, or transmitted in any form or by any means, electronic, mechanical, photocopying, recording or otherwise, without the prior permission of the copyright owner.

**Quantitative and localized spectroscopy for non-invasive
bilirubinometry in neonates**

ACADEMISCH PROEFSCHRIFT

ter verkrijging van de graad van doctor

aan de Universiteit van Amsterdam

op gezag van de Rector Magnificus

prof.dr. D.C. van den Boom

ten overstaan van een door het college voor promoties ingestelde
commissie, in het openbaar te verdedigen in de Agnietenkapel

op donderdag 8 maart 2012, te 14:00 uur

door Nienke Bosschaart

geboren te Stede Broec

Promotiecommissie

Promotor: Prof.dr. A.G.J.M. van Leeuwen

Co-promotor: dr.ing. M.C.G. Aalders

Overige leden:
Prof.dr. M.J. Schultz
Prof.dr.ir. C. Ince
Prof.dr.ir. R.M. Verdaasdonk
Prof.dr. A. Mahadevan-Jansen
Prof.dr.ir. W. Steenbergen

Faculteit der Geneeskunde

Table of contents

Chapter 1	General introduction to the thesis	7
Chapter 2	Limitations and opportunities of transcutaneous bilirubin measurements	15
Chapter 3	Optical properties of neonatal skin measured <i>in vivo</i> as a function of age and skin pigmentation	25
Chapter 4	Quantitative measurements of absorption spectra in scattering media by low-coherence spectroscopy	43
Chapter 5	Measurements of wavelength dependent scattering and backscattering coefficients by low-coherence spectroscopy	55
Chapter 6	<i>In vivo</i> low-coherence spectroscopic measurements of local hemoglobin absorption spectra in human skin	67
Chapter 7	Improved acquisition speed in low-coherence spectroscopy by means of spectroscopic detection	75
Chapter 8	Concluding remarks and outlook	89
	List of symbols	99
	List of abbreviations	100
	List of publications	101
	Summary	102
	Samenvatting	104
	Dankwoord	106
	Curriculum Vitae	108

CHAPTER 1

General introduction to the thesis

In this introductory Chapter, we describe the shortcomings of the available optical spectroscopic techniques for the medical application of non-invasive measurements of bilirubin and hemoglobin concentrations in blood. We emphasize the need for a spectroscopic technique that can both *quantitatively* and *locally* measure absorption coefficients in tissue. Since such a technique is not readily available, we propose the development of a new spectroscopic technique called low-coherence spectroscopy (LCS). Furthermore, we introduce the problem of non-invasive bilirubinometry in neonates, which will be the primary application for the development of LCS.

1.1 Tissue spectroscopy

Light-tissue interactions are the basis of many experimental and routinely used diagnostic procedures in medicine. One of the most extensively examined interactions of light with tissue involves the absorption of light, since this can provide valuable information on the presence of chromophores (i.e. light absorbing molecules such as bilirubin, hemoglobin and melanin), which can be related to the physiological condition of the tissue and the overall condition of the body. Examples of light absorption based techniques that are frequently used in the practice of medical diagnostics are pulse oximetry [1], transcutaneous bilirubinometry [2] and near-infrared brain monitoring [3]. The existence of these non-invasive techniques substantially reduces the need for alternative, often invasive and time consuming diagnostic procedures and provides a unique insight into otherwise unknown body processes.

Although numerous techniques based on light tissue interactions are available for solving medical diagnostic problems, for some problems the existing techniques are not appropriate. One of these problems is the non-invasive measurement of bilirubin and hemoglobin concentrations in blood, for which the alternative is invasive blood sampling. This section explains the reasons for the shortcomings of existing optical techniques for this purpose.

1.1.1 Quantitative spectroscopy

For the measurement of bilirubin and hemoglobin concentrations, *quantification* of tissue absorption is needed, since the amount of tissue absorption is directly related to chromophore concentrations. To quantify absorption, the absorption coefficient is used, for which a detailed definition can be found in Section 1.3. In tissue, the absorption coefficient is wavelength dependent, as has been illustrated for the skin in Figure 1.1.

Wavelength dependent absorption coefficients are generally determined using optical spectroscopy, which measures the wavelength resolved changes in the intensity of light that is reflected by, or transmitted through the tissue. Since the absorption coefficient describes the amount of absorption along a certain photon path (Section 1.3), knowledge of the photon path is required to derive this optical property from the measured spectrum.

The determination of photon paths is one of the main challenges in tissue spectroscopy, since it is difficult to predict the amount of tissue scattering that influences both the length and direction of these paths. Most spectroscopic techniques solve this problem by making model-based assumptions on the photon path length [4-6]. Unfortunately, this introduces an inevitable error in the determination of the absorption coefficient, since model and reality rarely agree completely.

In contrast to making assumptions on the photon path, *measuring* the photon path gives a more exact determination of the absorption coefficient. Several spectroscopic techniques (i.e. time, and phase resolved spectroscopy [7,8]) have been developed for measuring photon paths, but in general these techniques require relatively long photon paths (several mm to cm), which hampers the possibility to measure the absorption coefficient within a small or thin tissue volume such as the microcirculation in the skin for the purpose of non-invasive blood analysis. Although low-coherence interferometry

techniques exist for measuring short photon path lengths (< 1 mm), the application of these techniques is mostly in imaging (i.e. OCT: optical coherence tomography [9]) or other areas [10,11], and does not, or only marginally investigate the possibility for the quantitative and *wavelength resolved* measurement of absorption coefficients.

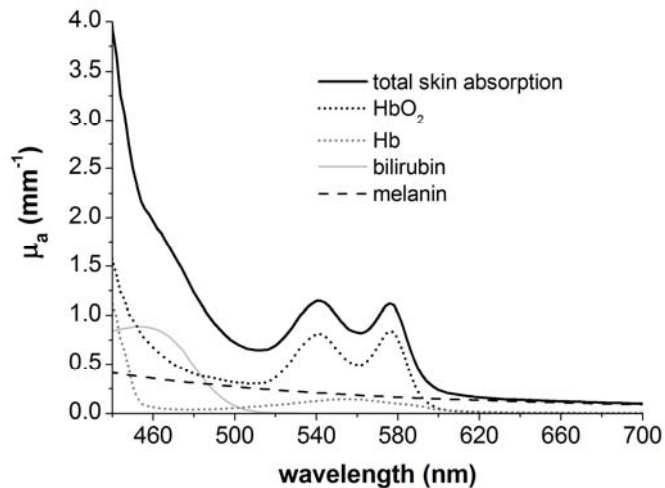


Figure 1.1 Absorption coefficient spectra of the most important skin chromophores in the visible wavelength range [14], for biologically occurring skin concentrations of hemoglobin (5 g/L, 85% oxygen saturation), bilirubin (70 μ mol/L) and melanin (0.4%).

1.1.2 Localized spectroscopy

Most tissues are optically inhomogeneous media, since they consist of numerous structures with distinct optical properties. As Figure 1.2a schematically illustrates for the case of a 'conventional' spectroscopic measurement on the skin, the light that probes the tissue passes many different tissue structures and layers before it is detected. As a consequence, the optical properties that are derived from the measurement will be (path length weighted) averaged over the probed volume, neglecting the differences in optical properties between the different structures.

For some diagnostic applications, the spatial averaging of optical properties induces an uncertainty in the parameter of interest. This is the case for the determination of bilirubin and hemoglobin concentrations in blood, since the skin cells surrounding the blood vessels in the probing volume (with lower, or absent chromophore concentrations) induce an underestimation of the true concentration. Therefore, besides measuring photon paths, it is also desired to *control* the photon path length in order to confine the probed volume to the tissue structure of interest such as a blood vessel (Figure 1.2b).

Unfortunately, the existing spectroscopic techniques that have the ability to measure the photon path length, lack the ability to precisely control it, due to the random process of tissue scattering [7,8]. However, the previously mentioned low-coherence interferometry based techniques do have the ability to precisely control the photon path lengths of the detected light. Hence, we will investigate the use of low-coherence interferometry for spectroscopic purposes.

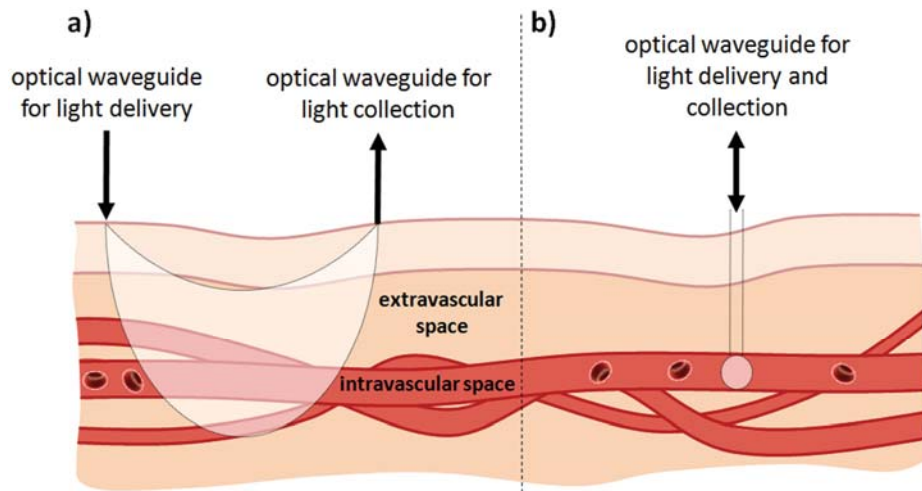


Figure 1.2 Schematic illustration of the skin volume that is probed by a.) 'conventional' spectroscopic techniques, which probe a variety of tissue structures (cell layers, blood vessels etc.); b.) the technique suggested in Section 1.2.1 (LCS), which has the ability to confine the probed volume to a structure of interest, e.g. a blood vessel.

1.2 This thesis

1.2.1 Low-coherence spectroscopy (LCS)

The objective of this thesis is to develop a method to non-invasively measure bilirubin and hemoglobin concentrations in blood. Therefore, a spectroscopic technique is needed that 1) quantifies the absorption coefficient and 2) measures it locally within a blood vessel in the skin, without the influence of surrounding tissue (Figure 1.2b). Since no existing spectroscopic technique meets with these requirements, a new spectroscopic technique will need to be designed and developed. As mentioned in Section 1.1, low-coherence interferometry offers both precise control over, and knowledge of the photon path. Therefore, we will investigate the possibility to do low-coherence interferometry based spectroscopy, which we will call low-coherence spectroscopy (LCS). This thesis will describe the essential first steps in the design, development and validation of this new technique.

1.2.2 Non-invasive bilirubinometry

Within the frame of non-invasive bilirubin and hemoglobin concentration measurements in blood, we specifically focus on non-invasive bilirubin measurements (bilirubinometry) in neonates who are admitted to the neonatal intensive care. Due to a relatively small total blood volume, required measurement frequency and often presence of other clinical complications, these patients have the highest need for a non-invasive alternative to invasive blood sampling.

Although devices based on optical spectroscopy for measuring bilirubin levels in neonates exist for over 30 years, the clinical utility of the technique is limited to a

screening method for hyperbilirubinemia, rather than a replacement for invasive blood sampling. The main reason for the limited clinical value of these devices is the fact that cutaneous bilirubin concentration measurements by spectroscopy (within a volume consisting of both intravascular and extravascular space, see Figure 1.2a) are compared to the gold standard of total serum bilirubin concentration measurements by invasive blood sampling (within a volume of whole blood, i.e. the intravascular space). Since these are two different concentrations, the current spectroscopic devices cannot equal the performances of invasive blood sampling.

If we can use LCS for the measurement of bilirubin concentrations within a single blood vessel (Figure 1.2b), a one to one comparison with total serum bilirubin concentration measurements will be achieved. Therefore, we expect that the use of LCS can significantly improve the clinical value of non-invasive bilirubinometry and lead to less pain and complications for preterm neonates.

1.2.3 Outline of the thesis

This general introduction to the thesis explained the current shortcomings of available optical spectroscopic techniques for the non-invasive measurement of bilirubin and hemoglobin concentrations in blood. In the remaining part of the thesis, we will describe the development of a new spectroscopic technique (LCS) that may aid in solving this problem. Since we primarily aim on using this technique for non-invasive bilirubinometry in neonates, the current status of non-invasive bilirubinometry, its limitations and opportunities are described in Chapter 2.

When designing a new optical technique for measurements on neonatal skin, knowledge of the optical properties of neonatal skin is required. Therefore, we measured the bulk optical properties of neonatal skin in a large patient population, as will be described in Chapter 3. A detailed definition of the optical properties of importance for this thesis will be given in the next section (Section 1.3).

Chapters 4 to 7 describe the development of LCS. First, the possibility of using LCS for the quantitative measurement of absorption coefficient spectra in tissue simulating media will be demonstrated in Chapter 4. Since LCS measures the total attenuation coefficient spectrum, which is the sum of the absorption and scattering coefficient spectra (Section 1.3), knowledge of the contribution of scattering to the LCS signal is important for accurate absorption measurements. Therefore, scattering contributions to the LCS signal will be investigated in Chapter 5. In Chapter 6, the exact control over the size and depth of the measurement volume in LCS will be demonstrated and the first *in vivo* results with this technique will be shown. To further enhance the clinical value of the technique, Chapter 7 addresses possibilities for enhancing the speed and sensitivity of LCS by introducing a new method for spectroscopic detection. Finally, Chapter 8 reflects on the current status of LCS for transcutaneous bilirubinometry and describes the necessary steps for further development of the technique.

1.3 Definition of optical properties

When light interacts with tissue, it will be attenuated by both scattering and absorption processes [12]. Light absorption occurs when photon energy is transferred to light

absorbing molecules, i.e. chromophores. The amount of absorption is quantified by the absorption coefficient μ_a in units of reciprocal distance (m^{-1}). Note that all wavelength dependent parameters in this thesis will be denoted by a bold-faced character. The reciprocal of the μ_a describes the average path length that a photon can travel in a medium before it is absorbed. For a medium with only one type of independently absorbing particles, the μ_a is defined by the cross section of the particle πr^2 (units: m^2) and the absorption efficiency Q_a (dimensionless) [12]:

$$\mu_a = N_a \cdot \pi r^2 \cdot Q_a \quad (1.1)$$

in which N_a denotes the number of absorbing particles per units of volume (m^{-3}). Figure 1.1 shows the absorption coefficient spectra of the most important skin chromophores in the visible wavelength range. When more than one type of chromophore is present in a medium, the total, or bulk absorption coefficient of the medium is the sum of all the individual chromophore contributions per unit of concentration: $\mu_{a,skin} = \sum_i (c_i \cdot \mu_{a,i})$, with c_i the relative contribution of chromophore i , assuming independent absorption events.

Light scattering by tissue occurs when photons encounter structures or particles with a higher or lower refractive index than the surrounding medium, such as cell membranes, collagen fibers and mitochondria. In this thesis, only elastic scattering processes are considered, which involve a change in the direction of photon propagation without any loss of photon energy. Similar to the absorption coefficient, tissue scattering is quantified by the scattering coefficient μ_s , from which the reciprocal describes the average path length that a photon can travel in a medium before it is scattered. For a medium with only one type of independently scattering particles it is defined as [12]:

$$\mu_s = N_s \cdot \pi r^2 \cdot Q_s \quad (1.2)$$

in which N_s is the number of scattering particles per units of volume and Q_s is the scattering efficiency of the particle. Similar to the absorption coefficient, the total, or bulk scattering coefficient of the medium is the sum of the (independent) contributions of all scattering particle types. In tissue, the bulk scattering coefficient has a power dependency on wavelength, since shorter wavelengths have a higher probability to be scattered [12]:

$$\mu_s \propto a \cdot \lambda^{-b} \quad (1.3)$$

in which a is a scaling factor and b denotes a parameter defined as the scatter power. Both absorption and scattering processes contribute to the total attenuation of light along a certain path. Hence, the attenuation coefficient μ_t is defined as the sum of μ_a and μ_s [12]:

$$\mu_t = \mu_a + \mu_s \quad (1.4)$$

The probability of a photon to be scattered under a certain angle is described by the scattering phase function $\mathbf{p}(\theta)$ [12]:

$$\int_0^{4\pi} \mathbf{p}(\Omega) \cdot d\Omega = 2\pi \int_0^\pi \sin(\theta) \mathbf{p}(\theta) \cdot d\theta = 1 \quad (1.5)$$

in which $d\Omega = d\phi \cdot d\theta$ denotes integration over the solid angle, and θ the angle in the plane of incidence.

When the scattering angle $\theta = \pi$ (or 180°), light is scattered back in the direction of incidence. In that case, we can define the back scattering coefficient μ_b :

$$\mu_b = \mu_s \cdot \mathbf{p}(\theta = \pi) \quad (1.6)$$

Note that the formal definition of μ_b by Van der Hulst includes an additional factor 4π [12]. For the LCS measurements described in Chapter 5, we define the $\mu_{b,NA}$ as the μ_b integrated over detection numerical aperture (NA) of the system (θ from $\pi-NA$ to π). Hence, the $\mu_{b,NA}$ is a measure for the amount of light that is detected after being back scattered by the sample, with a dependence on the properties of both the system and the medium.

Another parameter that is important in LCS, is the group refractive index. The group refractive index n_g depends on all wavelengths λ within the spectral bandwidth that is regarded, and is defined as:

$$n_g = n + \lambda \frac{\partial n}{\partial \lambda} \quad (1.7)$$

in which n is the wavelength dependent, or phase refractive index of the medium.

Scattering is isotropic when $\mathbf{p}(\theta)$ is independent on θ , otherwise it is anisotropic. The latter is often the case for tissue, which is why we define the scattering anisotropy \mathbf{g} as the average of the cosine of the scattering angle [13]:

$$\mathbf{g} = \langle \cos(\theta) \rangle \quad (1.8)$$

Hence, $\mathbf{g} = 1$ describes the case of purely forward scattering, $\mathbf{g} = -1$ the case of purely backward scattering, and $\mathbf{g} = 0$ the case of isotropic scattering.

When photons are scattered many times before they are detected, e.g. for diffuse photon distributions, the scattering anisotropy affects the amount of photons that are captured within the detection NA of the system. As a consequence, the 'effective' attenuation of light by scattering is lower than predicted by μ_s in forward scattering media such as tissue ($0 < \mathbf{g} < 1$). Therefore, the reduced scattering coefficient μ_s' is defined as [13]:

$$\mu_s' = \mu_s (1 - \mathbf{g}) \quad (1.9)$$

Similarly, the effective attenuation coefficient μ_{eff} becomes [13]:

$$\mu_{\text{eff}} = \sqrt{3 \cdot \mu_a (\mu_a + \mu_s')} \quad (1.10)$$

Equations 1.3 and 1.8 to 1.10 are particularly important for the measurements described in Chapter 3; equations 1.3 to 1.8 are of importance for the measurements described in Chapters 4 to 7.

References

1. J.W. Salyer, "Neonatal and pediatric pulse oximetry", *Respiratory Care* **48**, 386-398 (2003)
2. J.R. Petersen, A.O. Okorodudu, A.A. Mohammad, A. Fernando, K.E. Shattuck, "Association of transcutaneous bilirubin testing in hospital with decreased readmission rate for hyperbilirubinemia", *Clinical Chemistry* **51**, 510-544 (2005)
3. P. Rolfe, "In vivo near-infrared spectroscopy", *Annual Review of Biomedical Engineering* **2**, 715-754 (2000)
4. R. Richards-Kortum, E. Sevick-Muraca, "Quantitative optical spectroscopy for tissue diagnosis", *Annual Review of Physical Chemistry* **47**, 555-606 (1996)
5. R.M.P. Doornbos, R. Lang, M.C. Aalders, F.W. Cross, H.J.C.M. Sterenberg, "The determination of in vivo human tissue optical properties and absolute chromophore concentrations using spatially resolved steady-state diffuse reflectance spectroscopy", *Physics in Medicine and Biology* **44**, 967-981 (1999)
6. R.L.P. van Veen, A. Amelink, M. Menke-Puymers, C. van der Pol, H.J.C.M. Sterenberg, "Optical biopsy of breast tissue using differential path-length spectroscopy", *Physics in Medicine and Biology* **50**, 2573-2581 (2005)
7. D.T. Delpy, M. Cope, P. van der Zee, S. Arridge, S. Wray, J. Wyatt, "Estimation of optical pathlength through tissue from direct time of flight measurement", *Physics in Medicine and Biology* **33**, 1433-1442 (1988)
8. T.H. Pham, O. Coquoz, J.B. Fishkin, E. Anderson, B.J. Tromberg, "Broad bandwidth frequency domain instrument for quantitative tissue optical spectroscopy", *Review of Scientific Instruments* **71**, 2500-2513 (2000)
9. D. Huang, E.A. Swanson, C.P. Lin, J.S. Schuman, W.G. Stinson, W. Chang, M.R. Hee, T. Flotte, K. Gregory, C.A. Puliafito, J.G. Fujimoto, "Optical coherence tomography", *Science* **254**, 1178-1181 (1991)
10. B. Varghese, V. Rajan, T.G. van Leeuwen, W. Steenbergen, "Path-length-resolved optical Doppler perfusion monitoring", *Journal of Biomedical Optics* **12**, 060508 (2007)
11. J. Kalkman, R. Sprik, T.G. van Leeuwen, "Path-length-resolved diffusive particle dynamics in spectral domain optical coherence tomography", *Physical Review Letters* **105**, 198302 (2010)
12. H.C. van de Hulst, "Light scattering by small particles" (Dover Publications, 1981)
13. B.C. Wilson, S.L. Jacques, "Optical reflectance and transmittance of tissues: principles and applications", *IEEE Journal of Quantum Electronics* **26**, 2186-2197 (1990)
14. Data tabulated from various sources compiled by S. Prahl, <http://omlc.ogi.edu/spectra> (1999)

CHAPTER 2

Limitations and opportunities of transcutaneous bilirubin measurements

Although transcutaneous bilirubinometers exist for over 30 years, the clinical utility of the technique is limited to a screening method for hyperbilirubinemia, rather than a replacement for invasive blood sampling. This study investigates the reason for this limited clinical value and addresses possibilities for improvement. To obtain better insight into the physiology of bilirubin measurements, we developed and evaluated an optical transcutaneous bilirubinometer that determines not only the cutaneous bilirubin concentration (TcB), but also the blood volume fraction (BVF) in the investigated skin volume. For 49 neonates (gestational age 30 ± 3.1 weeks, postnatal age 6(4-10) days) at our neonatal intensive care unit, we performed 124 TcB and 55 BVF measurements. The TcB correlated well with the total serum bilirubin concentration (TSB) ($r=0.88$) with an uncertainty of $55 \mu\text{mol/L}$. The BVF in the measured skin volume ranged between 0.1–0.75%. The performance of our bilirubinometer is comparable to existing transcutaneous devices. The limited clinical value of current bilirubinometers can be explained by the low BVF in the skin volume that is probed by these devices. Since the TcB depends for over 99% on the contribution of extravascular bilirubin, it is a physiologically different parameter from the TSB. Hence, the standard method of evaluation that compares the TcB to the TSB is insufficient to fully investigate the clinical value of transcutaneous bilirubinometers, i.e. their predictive value for kernicterus. We suggest that the clinical value may be improved considerably by changing either the method of evaluation, or the technological design of transcutaneous bilirubinometers.

Part of this work has been accepted for publication in: N. Bosschaart, J.H. Kok, A.M. Newsum, D.M. Ouweneel, R.M. Mentink, T.G. van Leeuwen, M.C.G. Aalders, "Limitations and opportunities of transcutaneous bilirubin measurements", *Pediatrics* 129(4), in press (2012)

2.1 Introduction

Jaundice is a common and often harmless clinical condition in neonates. However, severe jaundice (hyperbilirubinemia) may result in kernicterus (bilirubin encephalopathy), causing irreversible brain damage to the patient. It is therefore vital to monitor the neonate's bilirubin levels to prevent hyperbilirubinemia by providing adequate treatment in case the bilirubin levels exceed the acceptable limits [1].

The current gold standard to measure bilirubin levels is invasive blood sampling, commonly performed by a heel stick, followed by laboratory analysis of the blood sample. This method provides the total serum bilirubin concentration (TSB), which can be related to the need for treatment in look-up tables that take into account the gestational age and birth weight of the neonate. Although over the years this method has been proven to be successful in preventing kernicterus [1], it has its drawbacks. Invasive blood sampling is painful and stressful for the neonate, resulting in blood loss and an increased risk of developing osteomyelitis and infections at the site of sampling [2,3]. In addition, the method is laborious and time consuming, lacking the possibility for immediate diagnosis or bed-side monitoring of bilirubin levels.

A possible alternative for invasive blood sampling is transcutaneous bilirubinometry, a non-invasive and painless method that provides an instantaneous read-out of the cutaneous bilirubin concentration (TcB). Transcutaneous bilirubinometry is based on optical spectroscopy, which relates the amount of light absorption by bilirubin (i.e. the yellow color of the skin) to the concentration of bilirubin in the skin. The first transcutaneous bilirubinometer was introduced in 1980 [4]. Since then, several other devices have been developed, and important adjustments, such as the correction for the presence of other skin chromophores (i.e. melanin and hemoglobin), were made to improve their accuracy [5-9]. These 'second generation' bilirubinometers are suitable for screening of hyperbilirubinemia, leading to a considerable decrease of the number of hospital readmissions [10] and a decrease of the amount of required blood samples from patients [11]. Hence, the use of transcutaneous bilirubinometers is recommended in clinical practice guidelines on the management of hyperbilirubinemia [12]. However, after more than 30 years of development, still no transcutaneous bilirubinometer has proven itself to be a worthy replacement for invasive blood sampling. Reasons for this limited clinical value may be diverse – e.g. the technological design of the bilirubinometers, the method of clinical evaluation and variations between patients – but have not been described or investigated thoroughly in literature. A better understanding of these reasons is important for both the interpretation of the measured TcB value from a patient, and for a possible improvement of the clinical value of transcutaneous bilirubinometers. Therefore, we developed and evaluated a new transcutaneous bilirubinometer that can aid to this understanding.

Our bilirubinometer differs from existing devices in light detection geometry and method of analysis, which enabled us to determine both the bilirubin concentration and the blood content inside the investigated skin volume. In general, the skin volume that is probed by transcutaneous bilirubinometers consists of both intravascular tissue space (within e.g. capillaries, arterioles) and extravascular tissue space, as illustrated in Figure 1.2a. Since the bilirubin concentration in the extravascular space is likely to be lower, the added information of blood content (i.e. quantification of intravascular space)

provides us with better insight into the physiology of TcB measurements. Moreover, whereas existing bilirubinometers use built-in calibration factors to correct for the concentration differences between the intravascular and extravascular space [5-9], the design of our bilirubinometer allowed us to measure the 'true' bilirubin concentration in the skin. Following this more thorough approach, we evaluate the performance of our device in a patient group of 49 neonates at our neonatal intensive care unit. Finally, we will use our findings in an effort to answer the question asked by many neonatologists and pediatricians: can transcutaneous bilirubinometry *replace* invasive blood sampling?

2.2 Methods

2.2.1 Patients

In a patient group of 49 neonates who were admitted to the neonatal intensive care unit of the Emma Children's hospital of the Academic Medical Center in Amsterdam, 124 blood samples were taken for TSB. Each blood sample was preceded by a TcB measurement with our bilirubinometer (within a time window of 30 minutes). Approval of the local medical ethical committee and informed consent from the patient's legally authorized representative was obtained. Blood samples were only taken for clinical reasons and were obtained by capillary heel stick or from arterial lines. The patient group varied in gestational age from 25 to 40 weeks (mean \pm standard deviation (SD): 30.0 ± 3.1 weeks), postnatal age from 2 to 84 days (<7 days: 65 measurements, ≥ 7 days: 59 measurements, median and 25th – 75th percentile: 6 (4-10) days), birth weight from 620 to 4140 grams (mean \pm SD: 1480 ± 660 grams) and ethnicity (Caucasian: 33, Mediterranean: 11, Negroid: 5). The majority of the patients were subjected to more than one measurement during their admission at the hospital, with a time lapse of one day to 3 weeks between measurements and a median of 2 measurements per patient.

2.2.2 Measurement device

The technical details of our transcutaneous bilirubinometer will be described in detail in Chapter 3 [13]. The device differs from other bilirubinometers in probe design, number of wavelengths, and the underlying physical model to extract the bilirubin concentration. Compared to existing bilirubinometers, this offers the unique advantage of quantifying other skin chromophore concentrations than the TcB, such as hemoglobin. In short, the device measures the skin absorption coefficient – a universal measure for the amount of light absorption in the skin (Section 1.3) – at every wavelength between 450 and 600 nm. The absorption coefficient contains the contributions of all skin chromophores (light absorbing molecules), which are bilirubin, oxygenized hemoglobin, deoxygenized hemoglobin and melanin in neonatal skin. For each individual chromophore, literature values of the chromophore-specific absorption coefficients are known for a standard concentration [14,15]. The measured skin absorption coefficient is the sum of all individual concentration dependent chromophore contributions. Therefore, by fitting the known chromophore-specific absorption coefficients to the skin absorption coefficient using a nonlinear least-square

Levenberg-Marquardt algorithm, we obtain the concentrations of bilirubin (TcB), oxygenized hemoglobin (TcHbO₂), deoxygenized hemoglobin (TcHb) and melanin.

The TcB was measured on the glabella of the forehead of the patients and was compared to their TSB, which was obtained from invasive capillary blood sampling at the heel maximally 30 minutes after the TcB measurement and analyzed by a Bilimeter 3 (Pfaff Medical, Germany). The uncertainty in the TSB determination by this device was $\pm 2.8\%$ of the measured value (95% confidence limit), which accounts for 1-11 $\mu\text{mol/L}$ in the investigated range of 40-400 $\mu\text{mol/L}$.

For 55 measurements, also the total blood hemoglobin concentration ([tHb]) was determined from the capillary blood sample by an XE-5000 analyzer (n = 34, Sysmex, Germany), or from an arterial line sample by a Rapidlab 1265 bloodgas analyzer (n = 21, Bayer Health Care, Germany). From these measurements, we determined the blood volume fraction (BVF) inside the measurement volume of the transcutaneous bilirubinometer, using $\text{BVF} = (\text{TcHb} + \text{TcHbO}_2) / [\text{tHb}] \times 100\%$. The measurement volume of this transcutaneous bilirubinometer comprises approximately 1 x 2.4 mm (depth x width) in neonatal skin [13].

2.3 Results

Figure 2.1 shows the measured TcB versus the TSB for all 49 patients and 124 measurements. Since most evaluation studies of transcutaneous bilirubinometers only regard patients in the first week after birth, difference is made between measurements on patients with a postnatal age less than 7 days (triangles) and 7 days or more (open circles). As expected, the TcB value in the investigated skin volume is approximately a factor 4 lower than the corresponding TSB value (linear regression on all 124 measurements yields $\text{TcB} = 0.26 \cdot \text{TSB} + 0.90$). Regardless of this difference, the TcB correlates well with the TSB (Spearman $r = 0.88$, $p < 0.01$, all 124 measurements), which is comparable to the clinical performance of commercial transcutaneous bilirubinometers [5-9,16]. The uncertainty in the measured TcB values is visualized in Figure 2.1 by their 95% prediction limits (PL). If we want to use these TcB measurements in clinical practice, we need to correct the measured TcB for the previously mentioned factor of ~ 4 , resulting in an uncertainty of 55 $\mu\text{mol/L}$ ($2 \cdot \text{SD}$ of the difference between the corrected TcB and the TSB). This uncertainty is also comparable to the clinical performance of commercial transcutaneous bilirubinometers [5-9,16]. The correlation between the TcB and the TSB does not alter when we regard only the measurements on patients with a postnatal age less than 7 days (Spearman $r = 0.88$, $p < 0.01$, $n = 65$), but it is lower when we regard only the measurements on patients with a postnatal age of 7 days or more (Spearman $r = 0.81$, $p < 0.01$, $n = 59$). This may be due to age related skin changes (thickening) and other, not investigated parameters. The influence of other patient characteristics (ethnicity, gestational age, birth weight) on the correlation between the TcB and the TSB was not assessed.

We found that the BVF in the measurement volume ranged between 0.1% and 0.75% (mean \pm SD: $0.35 \pm 0.12\%$), which is slightly lower than the average BVF of 2-5% in well perfused adult human skin [15], but comparable to the vessel density (vessel length*diameter per tissue area) of 0.20-0.23% observed in orthogonal polarization

spectral images of the microcirculation of neonatal skin at the inner upper arm [17]. Since the BVF accounts for the amount of intravascular space present in the measurement volume of the transcutaneous bilirubin measurement, we can conclude that over 99% of the bilirubin contributing to the measured TcB, is extravascular bilirubin. Furthermore, no correlation exists between the measured BVF and TcB (Pearson $r = 0.03$, $p > 0.05$), which implies that high TcB values cannot be associated with a higher vessel density in the measurement volume.

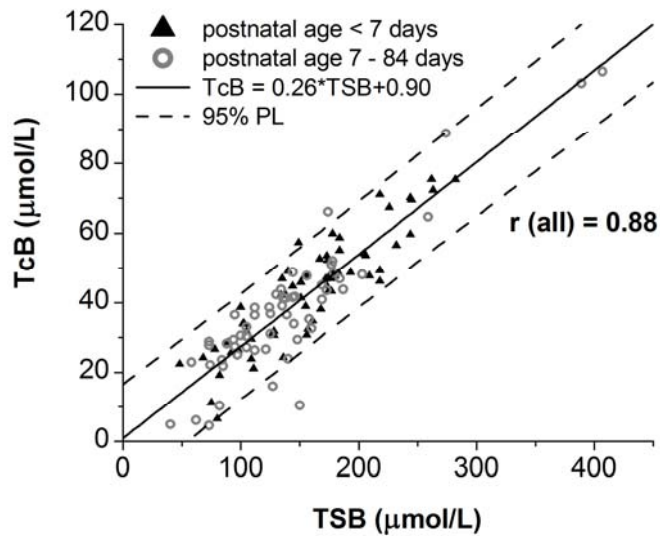


Figure 2.1 Comparison of 124 patient measurements (postnatal age < 7 days and ≥ 7 days) of the TcB to the TSB, with 95% PL of the linear regression $TcB = 0.26*TSB + 0.90$ (Spearman $r = 0.88$, $p < 0.01$). Conversion of units: $1 \mu\text{mol/L} = 0.0585 \text{ mg/dL}$ bilirubin. Note the difference in horizontal and vertical scaling.

2.4 Discussion

The evaluation of our transcutaneous bilirubinometer showed that its performance is comparable to existing devices and therefore, it does not lead directly to an improved clinical value for transcutaneous bilirubinometry. However, with our device we were able to estimate also the blood volume fraction in the probed skin volume, which aids to better understanding of the differences between transcutaneous and blood sampling bilirubin measurements. From our results we can learn two important lessons: 1) the contribution of intravascular bilirubin to the measured TcB is less than 1%, and 2) the extravascular bilirubin concentration is approximately a factor 4 lower than the TSB. Hence, we can draw the conclusion that the TcB is a physiologically different parameter from the TSB, since the first contains mainly the contribution of extravascular bilirubin and the latter equals the bilirubin concentration in the intravascular space. Awareness of this difference is important when interpreting TcB measurements on patients, because it is not straight forward to relate a TcB value to a TSB value [18]. The relation between the TcB and the TSB depends on numerous factors regulating the extravasation and clearance of bilirubin in the extravascular space. Many of these factors are difficult to model, such as the photo break-down of bilirubin by phototherapy or day light influences [19], or are still not well understood, such as the

cephalocaudal progression of jaundice [20]. This raises a new, but relevant question: is it justified to evaluate the clinical value of the TcB by comparing it to the TSB?

Any new medical diagnostic technique needs to prove that its performance is equal to, or better than that of the gold standard, in order to replace it [21]. Therefore, to test the performance of transcutaneous bilirubinometers, their outcome is commonly compared to the outcome of the total serum bilirubin measurements from invasive blood sampling. However, because of the complex nature of the processes that regulate the extravasation and clearance of bilirubin [18-20], the uncertainty in the TcB measurement is considerable when comparing it to the TSB (Figure 2.1). Since the accuracy of our bilirubinometer in measuring bilirubin absorption is approximately 15% [13], we can assume that the majority of the uncertainty in our TcB evaluation is caused by the physiological difference between the two parameters [22,23]. Because of this physiological difference, transcutaneous bilirubinometry will never equal the performances of the gold standard, invasive blood sampling [22]. This is the major reason why transcutaneous bilirubinometry has not yet replaced invasive blood sampling, and that it is primarily used as a screening method for hyperbilirubinemia. Fortunately, this does not imply that we have reached an end station in the clinical utility of transcutaneous bilirubinometry. We stress that the clinical value of transcutaneous bilirubinometry can be increased considerably, by choosing either a medical, or a technological approach to solving the problem. Both approaches will be explained in more detail below.

2.4.1 Medical approach to enhanced clinical value

In patients with hyperbilirubinemia, the clinically relevant parameter is the risk for developing kernicterus. The TSB has proven to be a good predictor for kernicterus, and extensive research and risk analyses have led to the TSB limits that we use today for treatment decision making. However, these limits are not conclusive, especially in extreme premature infants, since some patients developed kernicterus even though the TSB was well below the safety limits [24]. This explains that the debate on the exact values of these limits is still ongoing [24,25]. Thus, although the TSB is a good predictor, it is not the perfect predictor for kernicterus. An increasing amount of studies suggest that the free bilirubin (unbound to albumin) concentration is a considerably better predictor for kernicterus than the TSB [25,26]. However, since no widely available method exists to determine the free bilirubin concentration, the TSB remains the gold standard for determining the risk for developing kernicterus [12,26].

From the results in Section 2.3 we know that transcutaneous bilirubinometry measures the extravascular, rather than the intravascular bilirubin concentration. Whereas bilirubin extravasation in the skin depends on both the concentration of unconjugated bilirubin that is free, and bound to albumin, in the brain it depends only on the concentration of free, unconjugated bilirubin that extravasates through the intact blood brain barrier and enters the subcortical cells [1]. The latter is caused by the absence of extravascular albumin space in the central nervous system [18]. However, the TcB may be more closely related to the risk for developing kernicterus than the TSB, since the TcB is a measure for the extravasated (unconjugated) bilirubin concentration and the TSB is a measure for the intravascular (added conjugated and unconjugated) bilirubin concentration. The added value of the TcB in the prediction of central nervous

system symptoms has been demonstrated before [27]. The TcB may therefore even be an equally good, or better predictor for kernicterus than the TSB, as has been recognized by others as well [7,18,22]. Hence, the true clinical value of current transcutaneous bilirubinometers should not be investigated by comparing the TcB to the TSB, but rather by clinical assessment of the TcB as a predictor for kernicterus. Such a study requires an extensive risk analysis in a large variety of patients over multiple hospitals, because the incidence of kernicterus is low at present.

Since the TcB reading may be influenced by the brand of the device [16], and the accuracy of the reading is influenced by the age of the patient [28] and the measurement site on the body [7], the influence of these factors needs to be included in the proposed risk analysis. We also need to keep in mind that the reproducibility of TcB measurements (coefficient of variation $\pm 4\%$ [4,6]) is lower than the reproducibility of TSB measurements (coefficient of variation $< 2\%$ [16]), although the latter does not take into account errors that may occur in the preanalytical phase of TSB measurements, e.g. during blood sampling and sample handling [29]. The difference in reproducibility between TcB and TSB measurements may result in larger safety margins for treatment decision making based on TcB measurements, but these safety margins will primarily depend on the predictive value of the TcB on kernicterus.

2.4.2 Technological approach to enhanced clinical value

Another possibility lies within a new design for transcutaneous bilirubinometers. Until now, all transcutaneous bilirubinometers measure the TcB in a tissue volume consisting mainly of skin cells and hence, the extravascular, rather than the intravascular bilirubin concentration is measured. In order to achieve a one to one comparison with the TSB, the measurement volume of transcutaneous bilirubinometers needs to be confined to the intravascular space, i.e. a volume consisting of blood only as illustrated in Figure 1.2b. This requires a spectroscopic technique that is capable of measuring the absorption coefficient in a confined volume of choice, such as a blood vessel. As described in Chapter 1, low-coherence interferometry (LCI) based techniques have proven that precise control of photon path lengths – and therefore measurement volume, in the case of single scattering events – is possible [30-33]. The possibilities for localized spectroscopy by LCI have only been marginally investigated in optical coherence tomography studies [32,33], which aimed on image contrast enhancement with relatively low spectral resolution, rather than accurate quantification of chromophore concentrations. However, we propose that the development of an LCI based technique that is optimized for spectroscopic purposes can be realized (LCS, Chapter 1). Hence, the feasibility of such a technique for transcutaneous bilirubinometry should be investigated.

2.5 Conclusion: can transcutaneous bilirubinometry *replace* invasive blood sampling?

In this Chapter, we tried to obtain better understanding of the reasons for the limited clinical value of transcutaneous bilirubinometers by evaluating a new design for a transcutaneous bilirubinometer. Although this device did not perform better than

existing devices, it did give us better insight into the physiology related to transcutaneous bilirubin measurements. The cutaneous bilirubin concentration (TcB) measured by transcutaneous bilirubinometry is a physiologically different parameter from the total serum bilirubin concentration in blood (TSB), since the TcB consists for over 99% of the contribution of extravascular bilirubin. Due to the complex nature of the processes that regulate the supply and clearance of bilirubin in the extravascular space, a one to one comparison of the TcB to the TSB is currently impossible. Therefore, transcutaneous bilirubinometry will not replace invasive blood sampling, if the criterion for this replacement remains that the TcB should equal the TSB. However, we suggest that two approaches can result in a better clinical value for transcutaneous bilirubinometry: 1) a medical approach, requiring an extensive risk analysis for the predictive value of the TcB for the occurrence of kernicterus and 2) a technological approach, where the measurement volume of the transcutaneous bilirubinometer is confined to the intravascular space, enabling a one to one comparison with the TSB. Both approaches are worth investigating, since a non-invasive alternative to invasive blood sampling in bilirubinometry will reduce pain, complications and diagnostic time for patients with hyperbilirubinemia.

References

1. J.M. Kirk, "Neonatal jaundice: a critical review on the role and practice of bilirubin analysis", *Annals of Clinical Biochemistry* **45**, 452-462 (2008)
2. J. Dai, D.M. Parry, J. Krahn, "Transcutaneous bilirubinometry: its role in the assessment of neonatal jaundice", *Clinical Biochemistry* **30**, 1-9 (1997)
3. L.D. Lilien, V.J. Harris, R.S. Ramamurthy, R.S. Pildes, "Neonatal osteomyelitis of the calcaneus: complication of heel puncture", *The Journal of Pediatrics* **88**, 478-480 (1976)
4. I. Yamanouchi, Y. Yamauchi, I. Igarashi, "Transcutaneous Bilirubinometry: Preliminary Studies of Noninvasive Transcutaneous Bilirubin Meter in the Okayama National Hospital", *Pediatrics* **65**, 195-202 (1980)
5. S. Yasuda, S. Itoh, K. Isobe, M. Yonetani, H. Nakamura, M. Nakamura, Y. Yamauchi, A. Yamanishi, "New transcutaneous jaundice device with two optical paths", *Journal of Perinatal Medicine* **31**, 81-88 (2003)
6. R. Tayaba, D. Gribetz, I. Gribetz, I.R. Holzmann, "Non-invasive estimation of serum bilirubin", *Pediatrics* **102**, e28 (1998)
7. F.F. Rubaltelli, G.R. Gourley, N. Loskamp, N. Modi, M. Roth-Kleiner, A. Sender, P. Vert, "Transcutaneous bilirubin measurement: a multicenter evaluation of a new device", *Pediatrics* **107**, 1264-1271 (2001)
8. D. De Luca, E. Zecca, M. Corsello, E. Tiberi, C. Semeraro, C. Romagnoli, "Attempt to improve transcutaneous bilirubinometry: a double blinded study Medick BiliMed versus Respironics BiliCheck", *Archives of Disease in Childhood – Fetal and Neonatal edition* **93**, 135-139 (2008)
9. G. Bertini, S. Pratesi, E. Cosenza, C. Dani, "Transcutaneous bilirubin measurement: evaluation of Bilitest", *Neonatology* **93**, 101-105 (2008)
10. J.R. Petersen, A.O. Okorodudu, A.A. Mohammad, A. Fernando, K.E. Shattuck, "Association of transcutaneous bilirubin testing in hospital with decreased readmission rate for hyperbilirubinemia", *Clinical Chemistry* **51**, 510-544 (2005)
11. M.J. Maisels, E. Kring, "Transcutaneous bilirubinometry decreases the need for serum bilirubin measurements and saves money", *Pediatrics* **99**, 599-601 (1997)
12. American Academy of Pediatrics, Subcommittee on Hyperbilirubinemia: M.J. Maisels, R.D. Baltz, V.K. Bhutani, T.B. Newman, H. Palmer, W. Rosenfeld, D.K. Stevenson, H.B. Weinblatt, "Clinical Practice Guideline: management of hyperbilirubinemia in the newborn infant 35 weeks of gestation", *Pediatrics* **114**, 297-316 (2004)

13. N. Bosschaart, R. Mentink, J.H. Kok, T.G. van Leeuwen, M.C.G. Aalders, "Optical properties of neonatal skin measured *in vivo* as a function of age and skin pigmentation", *Journal of Biomedical Optics* **16**, 097003 (2011)
14. S.C. Kanick, C. van der Leest, J.G. Aerts, H.C. Hoogsteden, S. Kascáková, H.J. Sterenberg, A. Amelink, "Integration of single-fiber reflectance spectroscopy into ultrasound-guided endoscopic lung cancer staging of mediastinal lymph nodes", *Journal of Biomedical Optics* **15**, 017004 (2010)
15. Data tabulated from various sources compiled by S. Prahl, <http://omlc.ogi.edu/spectra> (1999)
16. K. Grohmann, M. Roser, B. Rolinski, I. Kadow, C. Muller, A. Goerlach-Graw, M. Nauck, H. Kuster, "Bilirubin measurement for neonates: comparison of 9 frequently used methods", *Pediatrics* **117**, 1174-1183 (2006)
17. O. Genzel-Boroviczeny, J. Strotgen, A.G. Harriz, K. Messmer, F. Christ, "Orthogonal polarization spectral imaging (OPS): a novel method to measure the microcirculation in term and preterm infants transcutaneously", *Pediatric Research* **51**, 386-391 (2002)
18. A. Knudsen, R. Brodersen, "Skin colour and bilirubin in neonates", *Archives of Disease in Childhood* **64**, 605-609 (1989)
19. G. Agati, F. Fusi, G.P. Donzelli, R. Pratesi, "Quantum yield and skin filtering effects on the formation rate of lumirubin", *Journal of Photochemistry and Photobiology B: Biology* **18**, 197-203 (1993)
20. N. Purcell, P.J. Beeby, "The influence of skin temperature and skin perfusion on the cephalocaudal progression of jaundice in newborns", *Journal of Paediatrics and Child Health* **45**, 582-586 (2009)
21. J.A. Knottnerus, C. van Weel, J.W.M. Muris, "Evidence base of clinical diagnosis - evaluation of diagnostic procedures", *British Medical Journal* **324**, 477-480 (2002)
22. R.E. Schumacher, "Transcutaneous bilirubinometry and diagnostic tests: the right job for the tool", *Pediatrics* **110**, 407-408 (2002)
23. D. de Luca, G.L. Jackson, A. Tridente, V.P. Carnielli, W.D. Engle, "Transcutaneous bilirubin nomograms", *Archives of Pediatrics and Adolescent Medicine* **163**, 1054-1059 (2009)
24. M. Moll, R. Goelz, T. Naegele, M. Wilke, C.F. Poets, "Are recommended phototherapy thresholds safe enough for extremely low birth weight (ELBW) infants? A report on 2 ELBW infants with kernicterus despite only moderate hyperbilirubinemia", *Neonatology* **99**, 90-94 (2011)
25. R.P. Wennberg, C.E. Ahlfors, V.K. Bhutani, L.H. Johnson, S.M. Shapiro, "Toward understanding kernicterus: a challenge to improve the management of jaundiced newborns", *Pediatrics* **117**, 474-485 (2006)
26. S.B. Amin, A.A. Lamola, "Newborn jaundice technologies: Unbound bilirubin and bilirubin binding capacity in neonates", *Seminars in Perinatology* **35**, 134-140 (2011)
27. A. Knudsen, F. Ebbesen, H. Hansen, R. Brodersen, "The increase of yellow skin colour beyond that of serum bilirubin: A proposed indicator of risk for bilirubin encephalopathy in the newborn", *Acta Paediatrica Japonica* **35**, 418-422 (1993)
28. D. de Luca, E. Zecca, P. de Turrís, G. Barbato, M. Marras, C. Romagnoli, "Using Bilicheck for preterm neonates in a sub-intensive unit: diagnostic usefulness and suitability", *Early Human Development* **83**, 313-317 (2007)
29. P. Bonini, M. Plebani, C. Ferruccio, F. Rubboli, "Errors in laboratory medicine", *Clinical Chemistry* **48**, 691-698 (2002)
30. D. Huang, E.A. Swanson, C.P. Lin, J.S. Schuman, W.G. Stinson, W. Chang, M.R. Hee, T. Flotte, K. Gregory, C.A. Puliafito, J.G. Fujimoto, "Optical coherence tomography", *Science* **254**, 1178-1181 (1991)
31. Varghese, V. Rajan, T.G. van Leeuwen, W. Steenbergen, "Path length resolved measurements of multiple scattered photons in static and dynamic turbid media using phase modulated low coherence interferometry", *Journal of Biomedical Optics* **12**, 024020 (2007)
32. B. Hermann, K. Bizheva, A. Unterhuber, B. Povazay, H. Sattman, L. Schmetterer, A.F. Fercher, W. Drexler, "Precision of extracting absorption profiles from weakly scattering media with spectroscopic time-domain optical coherence tomography", *Optics Express* **12**, 1677-1688 (2004)
33. Dubois, J. Moreau, C. Boccara, "Spectroscopic ultrahigh-resolution full-field optical coherence microscopy", *Optics Express* **16**, 17082-17091 (2008)

CHAPTER 3

Optical properties of neonatal skin measured *in vivo* as a function of age and skin pigmentation

Knowledge of the optical properties of neonatal skin is invaluable when developing new, or improving existing optical techniques for use at the neonatal intensive care. In this Chapter, we present *in vivo* measurements of the absorption μ_a and reduced scattering coefficient μ_s' of neonatal skin between 450 and 600 nm and assess the influence of age and skin pigmentation on the optical properties.

The optical properties were measured using a spatially resolved, steady state diffuse reflectance spectroscopy setup, combined with a modified spatially resolved diffusion model. The method was validated on phantoms with known values for the absorption and reduced scattering coefficient. Values of μ_a and μ_s' were obtained from the skin at four different body locations (forehead, sternum, hand and foot) of 60 neonates with varying gestational age, postnatal age and skin pigmentation.

We found that μ_a ranged from 0.02-1.25 mm^{-1} and μ_s' was in the range of 1-2.8 mm^{-1} (5th – 95th percentile of the patient population), independent of body location. In contrast to previous studies, no to very weak correlation was observed between the optical properties and gestational maturity, but a strong dependency of the absorption coefficient on postnatal age was found for dark skinned patients.

3.1 Introduction

Light-tissue interactions in the visible wavelength range are the basis of many experimental and routinely used diagnostic and therapeutic procedures at the neonatal intensive care – e.g. in transcutaneous bilirubinometry [1], pulse oximetry [2] and phototherapy during jaundice [3]. Knowledge of the optical properties of the tissue is essential when predicting or modeling light-tissue interactions, which in turn is invaluable for the development and improvement of these procedures. Although the majority of optical techniques at the neonatal intensive care depend on the interaction of light with skin, very little information can be found in literature about the optical properties (e.g. absorption and scattering coefficients) of neonatal skin.

Earlier research on the optical properties of neonatal skin was performed by Saidi *et al*, who measured the absorption coefficient and the reduced scattering coefficient as a function of age with an integrating sphere setup [4,5]. They found that the reduced scattering coefficient increases with age, due to maturation of the skin. These measurements were performed *in vitro* on excised non-pigmented skin. However, optical properties measured *in vitro* may differ substantially from those measured *in vivo* due to the unavoidable sample preparation procedures [6]. Moreover, it is expected that the absorption coefficient depends on skin pigmentation, which was not investigated. We expect that optical properties of neonatal skin, assessed by *in vivo* measurements as a function of age and skin pigmentation, can assist many optical devices such as transcutaneous bilirubinometers in improving their performance. The readings of current bilirubinometers commonly have a spread of $\pm 40 \mu\text{mol/L}$ around the bilirubin concentration (ranging from 0 – 400 $\mu\text{mol/L}$) that is measured by the gold standard for bilirubin measurements, total serum bilirubin analysis [1]. This inaccuracy may be partly caused by variations in the often unknown probed volume inside the skin. Knowledge of the optical properties can be used as input to, for example, Monte Carlo simulations of photon distributions inside the skin. These simulations can provide insight into the probed tissue volume, which in turn can lead to a more optimal design for optical diagnostic probes, methods of analysis and comparison between devices.

Steady state, spatially resolved diffuse reflectance spectroscopy has proven to be a reliable technique for measuring the optical properties of tissue and tissue simulating phantoms in the near infrared [7,8] and visible [8,9] wavelength range. When using short source-detector distances, the investigated tissue volume is small [9] and can be confined to, for instance, the skin. Therefore, in this study we used a steady state, spatially resolved diffuse reflectance spectroscopy setup and a semi-empirical 3D-diffusion model, modified for our detection geometry, to measure the absorption and reduced scattering coefficient of neonatal skin from 450 – 600 nm.

The optical properties were measured on the skin of 60 preterm neonates with varying gestational maturity, postnatal age and skin pigmentation. All measurements were performed on four body locations (forehead, sternum, hand and foot), which are common measurement sites for either transcutaneous bilirubinometry, or pulse oximetry. The method was validated on phantoms with known values for the absorption and reduced scattering coefficient.

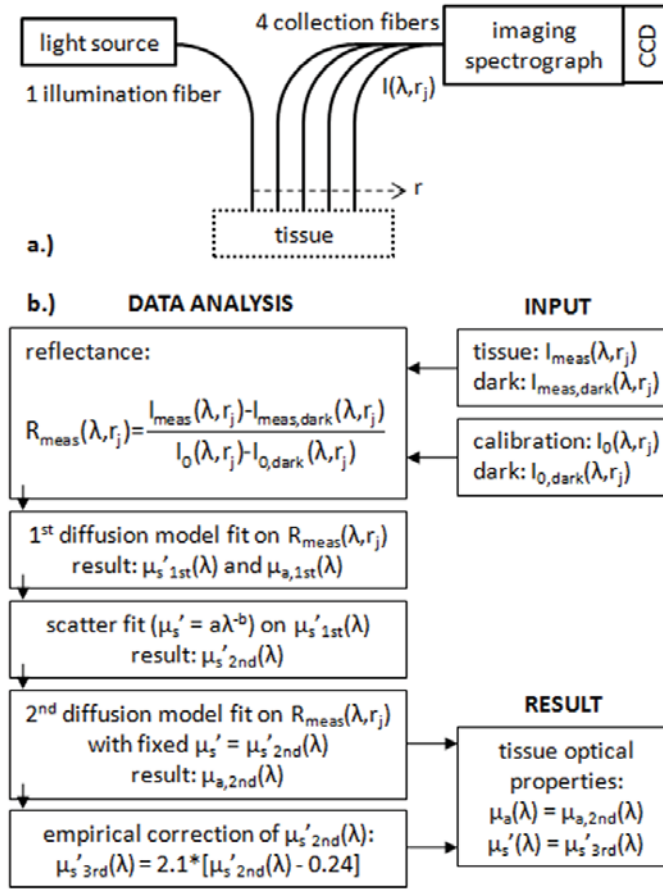


Figure 3.1 a) Illustration of the measurement setup.
 b) Schematic illustration of the data analysis.

3.2 Methods

3.2.1 Experimental setup

The diffuse reflectance spectroscopy setup (similar to that of Doornbos *et al* [7] and Nichols *et al* [8]) is shown in Figure 3.1a. Tissue illumination and detection of re-emitted light are performed by a multi-fiber probe. The probe consists of 5 fibers (400 μm core diameter, length ~ 2 m) which are cast in-line in an aluminum sensing head with a core-to-core distance of 600 μm . The first fiber acts as the illumination fiber and guides the white light from a tungsten halogen source (AvaLight-HAL, Avantes, USA) to the tissue. The other four fibers detect the re-emitted light (source-detector distances of $r_1 = 0.6$ mm, $r_2 = 1.2$ mm, $r_3 = 1.8$ mm, $r_4 = 2.4$ mm) and guide it to an imaging spectrograph (Olympus ISS, Olympus, USA). A 16-bit 128 x 1024 pixel CCD camera (DH501-18F-01, Andor Technology, USA) cooled to 0 $^{\circ}\text{C}$ detects the four spectra originating at different distances from the illumination fiber, with a wavelength resolution of 9 nm over the detection range of 400 to 820 nm. The image tracks illuminated by the fibers are averaged for each fiber to obtain four averaged spectra. The total exposure time for the

in vivo measurements ranged between 15 and 35 ms. In order to minimize system noise and to correct for temporal variation, each measurement in this Chapter consists of the average of three subsequent measurements with an interval of 1s.

3.2.2 Setup calibration

The diffuse reflectance measurements require three types of calibration: 1) wavelength calibration of the spectrograph, 2) calibration to correct for the collection efficiency of the setup and the spectral emission of the source and 3) correction for the (small amount of) ambient light and system noise.

The wavelength calibration of the spectrograph is performed by measuring the emission of a 543 nm and a 633 nm HeNe laser, and the emission of a fluorescent lamp. An additional calibration is done prior to each patient/phantom measurement by measuring the spectrum of a fluorescent light tube. The collection efficiency of the setup and the spectral emission of the source are calibrated using the method described in detail by Doornbos *et al* [7], which comprises measuring the collected intensity for each detection fiber at the entrance of an integrating sphere, illuminated by the illumination fiber of the probe. This calibration results in a calibration spectrum for each fiber distance r_j , indicated by $I_0(r_j)$ (all wavelength dependent parameters in this Chapter will be denoted by a bold-faced character).

To correct for the collection of ambient light and system noise, a dark measurement was taken prior to each patient/phantom measurement with a shielded probe. The dark measurement results in a dark spectrum for each fiber distance, indicated by $I_{\text{dark}}(r_j)$.

3.2.3 Data analysis

To extract the absorption and reduced scattering coefficient from the acquired spectra, we use the steady state diffusion approximation to the photon transport equation described by Farrell *et al* [10]. This diffusion model describes the 3D photon distribution inside a medium for photons injected by a point source, by modeling an isotropic source at a depth z_0 inside the tissue and a virtual source at a distance of $2z_b+z_0$ above the medium. The remittance R_{theor} at the tissue surface as a function of source-detector distance r , and the optical properties of the tissue is given by [10]:

$$R_{\text{theor}}(r) = \frac{1}{(4\pi)} \left[\frac{z_0}{r_1^2} \left(\mu_{\text{eff}} + \frac{1}{r_1} \right) e^{-\mu_{\text{eff}} r_1} + \frac{(z_0 + 2z_b)}{r_2^2} \left(\mu_{\text{eff}} + \frac{1}{r_2} \right) e^{-\mu_{\text{eff}} r_2} \right] \quad (3.1)$$

where $\mu_{\text{eff}} = [3\mu_a(\mu_a + \mu_s')]^{1/2}$, $r_1 = (z_0^2 + r^2)^{1/2}$, $r_2 = [(z_0 + 2z_b)^2 + r^2]^{1/2}$, $z_0 = (\mu_a + \mu_s')^{-1}$, and $z_b = 2/3 \cdot A(\mu_a + \mu_s')^{-1}$. Note that all parameters, except r , are wavelength dependent. The value of the empirical parameter A in the definition of z_b was set to $A=1$, since this gave the most reliable results (i.e. smallest residuals) when fitting our model to the data. Fitting the diffusion model to the spatially measured reflectance of the four detection fibers all together, using $R_{\text{meas}}(r_j) = \alpha \cdot R_{\text{theor}}(r_j)$ yields a single set of the parameters μ_a and μ_s' . The proportionality factor α is adapted from Doornbos *et al* [7] and contains factors like the numerical aperture and the efficiency of coupling light into the sample. The value of α was found by fitting the diffusion model to the reflectance of a phantoms with known μ_a and μ_s' (Section 3.2.4).

Our method of analysis (schematically depicted in Figure 3.1b) can be explained in the following steps, in which we adapted steps 1 to 4 from Doornbos *et al*: 1) calculation of the measured reflectance for each fiber distance: $\mathbf{R}_{\text{meas}}(r_j) = [I_{\text{meas}}(r_j) - I_{\text{meas,dark}}(r_j)] / [I_0(r_j) - I_{0,\text{dark}}(r_j)]$, 2) fitting the diffusion model to $\mathbf{R}_{\text{meas}}(r_j)$, using a nonlinear least-square Levenberg-Marquardt algorithm, which results in a first approximation for the wavelength dependent absorption and reduced scattering coefficient $\mu_{a,1st}$ and $\mu_{s',1st}$, 3) fitting the function $\mu_{s'} = a\lambda^{-b}$ (where b is the scatter power and both a and b are free running fit parameters) to the obtained $\mu_{s',1st}$ using a nonlinear least-square Levenberg-Marquardt algorithm, which results in a second approximation for the reduced scattering coefficient $\mu_{s',2nd}$, 4) re-fitting the diffusion model to $\mathbf{R}_{\text{meas}}(r_j)$ with $\mu_{s',2nd}$ as a fixed parameter, which results in a second approximation for the absorption coefficient $\mu_{a,2nd}$, 5) correction of $\mu_{s',2nd}$ for an initial underestimation using the empirically determined relation $\mu_{s',3rd} = 2.1 * (\mu_{s',2nd} - 0.24)$ (see Section 3.3.1). The obtained values for $\mu_{a,2nd}$ and $\mu_{s',3rd}$ are regarded as the bulk optical properties of the tissue in the measurement volume, from now on indicated by μ_a and $\mu_{s'}$.

The diffusion model is valid for semi-infinite, homogeneous media where scattering dominates absorption ($\mu_a/\mu_{s'} \leq \beta$, commonly with $\beta \ll 1$) and a source-detector separation that ensures a diffuse photon distribution ($r > \gamma/(\mu_a + \mu_{s'})$, commonly r is at least one mean free path, $1/(\mu_a + \mu_{s'})$, hence $\gamma=1$). Note that for our probe geometry, the value of γ depends entirely on the lowest value of $(\mu_a + \mu_{s'})$ that can be accurately measured, since the (minimal) source-detector separation r is fixed. To determine the validity and accuracy of the model for our measurement geometry and neonatal skin, we performed measurements on phantoms with optical properties in the range of neonatal skin and found the limiting values for β and γ (Section 3.3.1). In contrast to Doornbos *et al*, who could only reliably measure the optical coefficients for wavelengths larger than 600 nm, we found that $r > \gamma/(\mu_a + \mu_{s'})$ is in general only valid for wavelengths shorter than 600 nm. This can be explained by a difference in probe design (i.e. shorter source-detector separations) and the relatively low value of $\mu_{s'}$ for neonatal skin. Therefore, we only determined the optical properties in the 450-600 nm wavelength region of the signal. The homogeneity of neonatal skin was investigated by optical coherence tomography (OCT) measurements (Section 3.4.3).

3.2.4 Phantom validation study

The method of analysis described above was validated with measurements on 14 phantoms with known values for μ_a and $\mu_{s'}$. The optical properties of the phantoms ($\mu_a = 0-2.7 \text{ mm}^{-1}$, $\mu_{s'} = 0.3-3.7 \text{ mm}^{-1}$) were chosen to be in the same range as the expected values of μ_a and $\mu_{s'}$ of neonatal skin. The phantoms consisted of two series: series 1, with a fixed concentration of 1.5% Intralipid (Intralipid®20%, Fresenius Kabi, Germany) and varying concentrations of a non-scattering, absorbing magenta dye (0.125-2%, Ecoline #337, Royal Talens, The Netherlands), and series 2, with a fixed concentration of 0.25% magenta dye and varying concentrations of Intralipid (0.25-2%). The reduced scattering coefficient of the phantoms was estimated using the predictions of Van Staveren *et al* [11] for $\mu_{s'}$ of Intralipid. The absorption coefficient of the dye only was determined in a separate transmission measurement by a spectrograph (USB4000, Ocean Optics, USA). During the measurements, the probe was in contact with the phantoms to minimize reflections from the phantom surface. From these phantom

measurements, we determined the accuracy of our determination of μ_a and μ_s' and the validity limits of our analysis, i.e. the limiting values of β and γ (i.e. $\mu_a/\mu_s' \leq \beta$ and $r > \gamma/(\mu_a + \mu_s')$) for which the diffusion model can be applied in this measurement geometry.

To verify that comparison with the predicted μ_s' of Van Staveren is justified for these phantoms, we also measured the μ_s' of National Institute of Standards and Technology (NIST)-certified spheres with a diameter of 409 nm, suspended in water (0.48 volume%, $\mu_s' = 2\text{--}3 \text{ mm}^{-1}$, Thermo Scientific USA). The measured μ_s' of this phantom was compared to the theoretical μ_s' , obtained from Mie theory.

For measurements of the optical properties of neonatal skin, it is important that the measurement volume is confined to the skin only. Therefore, knowledge of the probing depth is required. To investigate the probing depth of the system, the probe was submersed at varying distances (0–5 mm, in steps of 100 μm) from the lower bottom of a phantom with μ_a and μ_s' similar to neonatal skin (1.5% Intralipid, 0.5% dye: μ_a up to 0.35 mm^{-1} , $\mu_s' = 2 - 2.6 \text{ mm}^{-1}$). The lower bottom of the liquid phantom consisted of a stationary solid layer of diffusively scattering white rubber. The measurements were repeated with a diffusively scattering black rubber layer at the lower bottom.

3.5.5 Patient study

60 Neonates of the neonatal intensive care unit in the Academic Medical Center of Amsterdam were enrolled in this study. Approval of the medical ethical committee and informed consent from the patient's legally authorized representative were obtained. The patient group varied in gestational age (i.e. pregnancy duration): 29.4 ± 3.3 weeks (mean \pm sd, normal distribution), postnatal age: 11 (6-28) days (median (25th – 75th percentile), non-normal distribution) and skin type. The skin type of the patients was classified into three categories, based on observation and ethnicity of the patient and the parents: type 1 (Caucasian or 'white': 43 patients), type 2 (Mediterranean or 'intermediate': 12 patients) and type 3 (Negroid or 'dark': 5 patients). The majority of the patients were subjected to more than one measurement during their admission at the hospital, with a time lapse of one day to several weeks between measurements and a median of 3 measurements per patient. An overview of the patient population and the number of measurements is listed in Table 3.1A.

The optical properties were determined at four locations on the skin: the glabella of the forehead, the lower end of the sternum, the plantar side of the foot and the dorsal side of the hand. The presence of visible large blood vessels in the measured volume was avoided. Due to medical reasons (e.g. presence of a ventilator, pulse oximeter and/or intravenous line), not all skin areas were accessible at all times, resulting in a different number of measurements between locations (Table 3.1A). To minimize reflections from the probe-tissue interface, the probe surface was covered with lubricating gel (Euroband Pedicat, Pollak, France). Attention was paid to keep a constant probe pressure on the skin during the measurements.

A general linear multivariate analysis model in SPSS for Windows (version 16.0, SPSS Inc.) was used to assess the influence of measurement location and skin type on the optical coefficients at three wavelengths (475, 525 and 575 nm), where we assumed a normal distribution of the data. To avoid the influence of dependent measurements in the multivariate analysis, one measurement event per patient (including all four locations) was randomly selected from our dataset.

To investigate the anatomy and homogeneity of neonatal skin compared to adult skin, Optical Coherence Tomography (OCT) B-scans were made with a 1310 nm OCT system (HSL-2000, Santec, Japan) at the four investigated skin areas of several patients and adults.

Table 3.1 Overview of the patient population and number of measurements per skin type and measurement location

	A. all measurements				B. measurements within validity limits			
	type 1	type 2	type 3	all	type 1	type 2	type 3	all
Location	# measurements				# measurements			
forehead	137	47	33	217	132	45	10	187
sternum	135	41	29	205	133	39	9	181
hand	137	47	30	214	134	41	11	186
foot	136	49	33	218	136	48	32	216
	# patients				# patients			
forehead	43	12	5	60	42	12	4	58
sternum	43	12	5	60	43	12	4	59
hand	42	12	5	59	42	12	5	59
foot	42	12	5	59	42	12	5	59
total # patients	43	12	5	60	43	12	5	60
gestational age (wks) mean (\pm sd)	29.9 (± 3.7)	29.2 (± 1.8)	27.4 (± 2.3)	29.4 (± 3.3)	29.9 (± 3.7)	29.2 (± 1.8)	27.5 (± 2.3)	29.4 (± 3.3)
postnatal age (days) median (p25-p75)	11 (6-35)	6 (4-13)	18 (9-34)	11 (6-28)	11 (6-35)	6 (4-13)	18 (10-32)	11 (6-28)

3.3 Results - phantom validation study

3.3.1 Validity and accuracy

Figure 3.2a and 3.2b show the measured $\mu_{s,2nd}'$ and μ_a versus the expected values (from Van Staveren and transmission spectroscopy, respectively) for all phantoms of series 1 and 2. Difference is made between phantoms for which the validity limits (i.e. $\mu_a/\mu_s' \leq \beta$ and $r > \gamma/(\mu_a + \mu_s')$) are valid for all wavelengths (black lines) and phantoms for which the validity limits are not valid for at least one wavelength between 450-600 nm (red lines). The obtained values for β and γ will be described below.

From Figure 3.2b, we can conclude that μ_a is predicted with 15% accuracy by our measurements up to a value of 1.7 mm^{-1} . Since the corresponding expected $\mu_s' = 2.3 \text{ mm}^{-1}$ for this value of μ_a , we conclude that the limiting ratio between μ_a and μ_s' for which the diffusion model can be applied in this measurement geometry, is $\beta = \frac{3}{4}$. This

value of β is considerably higher than the commonly used value $\beta = 1/10$ in other diffusion model based studies [7,8]. For the phantoms where $\mu_a/\mu_s' \leq 3/4$ is not valid, μ_a is underestimated by our measurement.

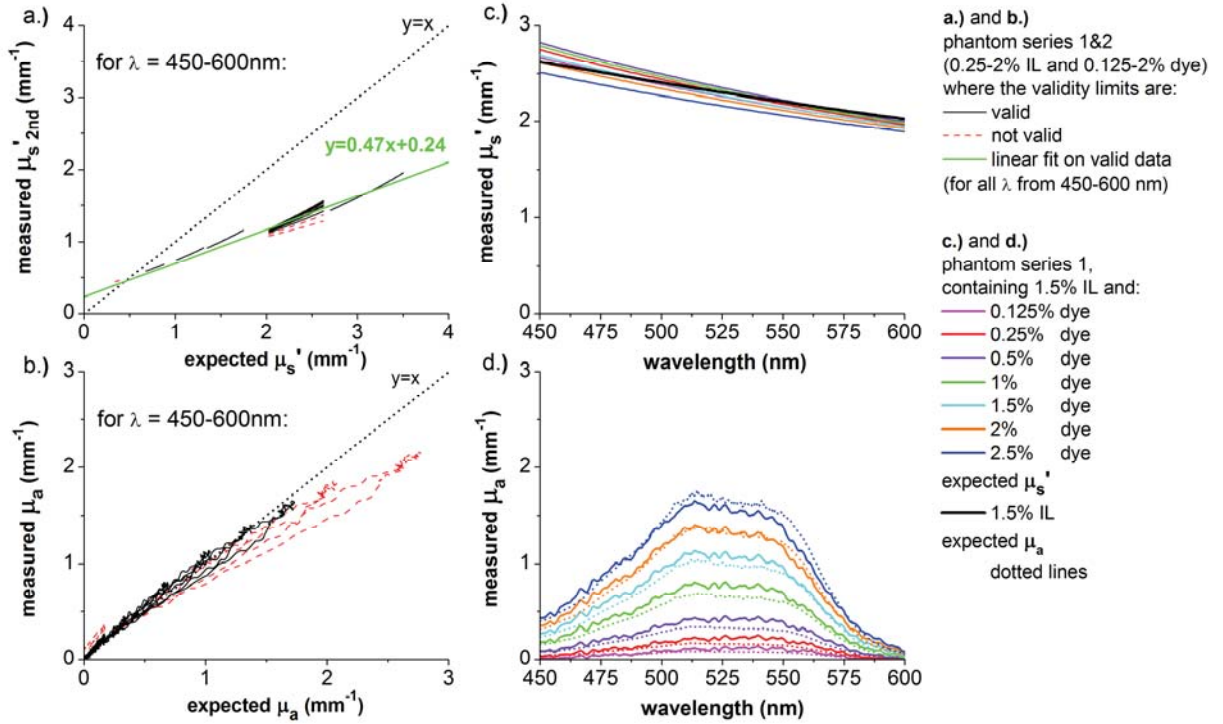


Figure 3.2 Phantom validation study. For all phantoms in series 1&2: a.) measured $\mu_{s'2nd}$ vs. expected $\mu_{s'}$, and b.) measured μ_a vs. expected μ_a . Difference is made between phantoms for which $\mu_a/\mu_{s'} \leq \beta$ and $r > \gamma/(\mu_a + \mu_{s'})$ are valid (black lines) and not valid (red lines). For all phantoms in series 1 for which $\mu_a/\mu_{s'} \leq \beta$ is valid: c.) measured $\mu_{s'}$ after correction and expected value vs. wavelength and d.) measured and expected μ_a vs. wavelength.

Figure 3.2a shows a consistent underestimation of $\mu_{s'2nd}$, which can be described by the linear relation ($\mu_{s'2nd} = 0.47\mu_{s'expected} + 0.24$) for the range of $\mu_{s'}$ -values within the validity limits. Exactly the same linear relation was found between the measured $\mu_{s'2nd}$ of the 409 nm NIST certified spheres and the expected $\mu_{s'}$ from Mie theory (no graph), indicating that the underestimation is consistent and not caused by incorrect comparison to the prediction of Van Staveren. We therefore corrected all measured $\mu_{s'2nd}$ (phantom and tissue measurements) for this underestimation, using the linear relation $\mu_{s'} = \mu_{s'3rd} = 2.1 * (\mu_{s'2nd} - 0.24)$.

Figure 3.2c and 3.2d show the measured $\mu_{s'}$ after correction and the measured μ_a versus wavelength for the phantoms of series 1 for which the validity limits are valid. Since the Intralipid concentration is fixed for the phantoms of series 1, $\mu_{s'}$ is expected to be equal for all phantoms. After correction, the measured $\mu_{s'}$ agree within 10% with the prediction of Van Staveren and a maximum variation of 10% can be observed between the measured $\mu_{s'}$ of all phantoms. As expected from Figure 3.2b, the measured μ_a in

Figure 3.2d agree within the reported accuracy with the expected μ_a from transmission spectroscopy.

We obtained the value of γ from the phantom series 2 with fixed μ_a and varying μ_s' . For these series, the μ_a and μ_s' were predicted correctly for the phantoms with $(\mu_a + \mu_s') > 0.8 \text{ mm}^{-1}$. For the phantom with $(\mu_a + \mu_s') < 0.8 \text{ mm}^{-1}$, μ_a was overestimated by our measurement. Since the minimal source-detector separation is 0.6 mm in our measurement geometry, we conclude that $\gamma = \frac{1}{2}$ in the validity limit $r > \gamma/(\mu_a + \mu_s')$.

Summarizing, our method is valid when measuring on semi-infinite homogeneous media with values of μ_a and μ_s' that meet the validity limits $\mu_a/\mu_s' \leq \frac{3}{4}$ and $(\mu_a + \mu_s') > 0.8 \text{ mm}^{-1}$. Our phantom study shows that these limits hold for this specific probe geometry and method of analysis. When measuring on neonatal skin, the validity of these limits needs to be investigated for every wavelength within the measured spectral range. Since we need to apply the empirically determined correction on the initial value of $\mu_s'_{2nd}$, our method of analysis based on the diffusion model is semi-empirical.

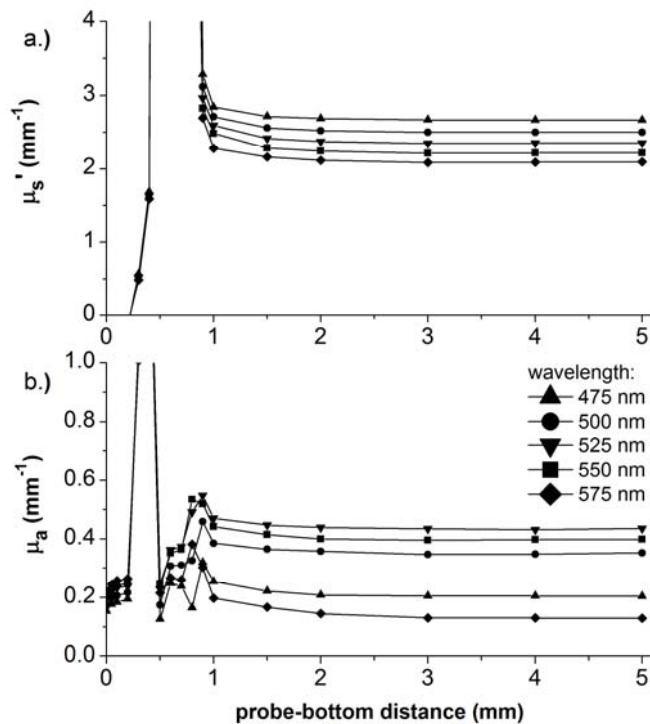


Figure 3.3 Measured values of a.) μ_s' and b.) μ_a as a function of probe-bottom distance for the 1.5%Intralipid-0.5%dye phantom and the black bottom layer. Results are shown for the wavelengths 475, 500, 525, 550 and 575 nm.

3.3.2 Probing depth

Figure 3.3 a and b show the dependency of the measured coefficients on the probe-bottom distance for the phantom with the black bottom layer. For probe-bottom distances $< 1 \text{ mm}$, the measured coefficients are inconsistent, due to presence of the black bottom layer in the measurement volume. For probe-bottom distances $\geq 1 \text{ mm}$, the measured μ_a and μ_s' are consistent and agree with the expected values within the reported accuracy. Also for the phantom with the white bottom layer, the measured μ_a and μ_s' are consistent for distances $\geq 1 \text{ mm}$. We therefore conclude that the probing

depth of the system is 1 mm for homogeneous media with optical properties comparable to the 1.5% Intralipid-0.5%dye phantom (i.e. $\mu_s' \approx 2.3 \text{ mm}^{-1}$ and $\mu_a \approx 0.4 \text{ mm}^{-1}$).

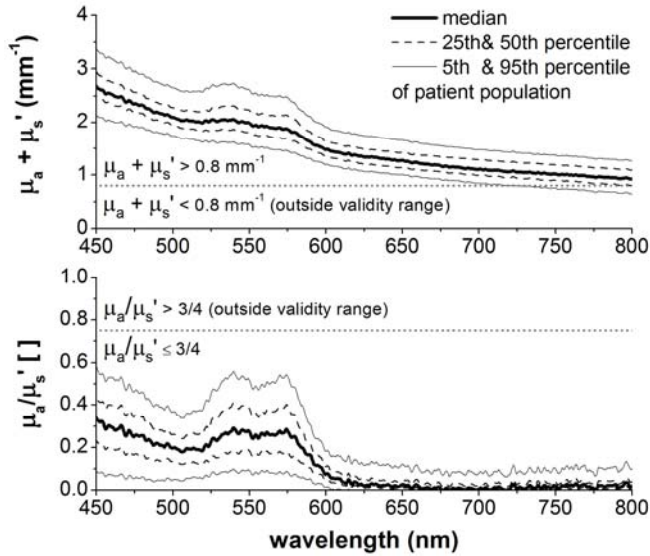


Figure 3.4 Median values and 5th, 25th, 75th and 95th percentiles for the measured μ_a/μ_s' and $(\mu_a+\mu_s')$ vs. wavelength for the patient measurements at the foot, after selection of the data between 450-600 nm by the validity limits (i.e. $\mu_a/\mu_s' \leq 3/4$ and $(\mu_a+\mu_s') > 0.8 \text{ mm}^{-1}$, Table 3.1B).

3.4 Results - patient study

3.4.1 Dependency on location and age

The validity of the diffusion model ($\mu_a/\mu_s' \leq 3/4$ and $(\mu_a+\mu_s') > 0.8 \text{ mm}^{-1}$) was checked for all patient measurements in the wavelength range of 450-600 nm, resulting in a reduction of the number of measurements and patients (Table 3.1B). Figure 3.4 shows the 5th to 95th percentiles of the selected patient measurements from Table 3.1B in the wavelength range of 450-800 nm. The validity of the limit $(\mu_a+\mu_s') > 0.8 \text{ mm}^{-1}$ is in general not valid for the longer wavelengths, hence our choice to only show the optical properties from 450 to 600 nm. Within the wavelength range of 450-600 nm, all patient measurements fall well within the validity limits of our analysis. The μ_s' and μ_a for all patients and measurements in Table 3.1B are shown in Figure 3.5 for each location, regardless of skin type. The optical coefficients from this patient population were not normally distributed for all wavelengths; therefore we present μ_s' and μ_a with the median, and 5th, 25th, 75th and 95th percentile. The median value for the scatter power b in μ_s' was 0.82 (forehead), 0.87 (sternum), 1.06 (hand) and 1.34 (foot). The multivariate analysis proved no significant differences ($p > 0.05$) in the optical coefficients between locations for each patient.

The dependencies of μ_s' and μ_a at $\lambda = 600 \text{ nm}$ on gestational maturity (gestational + postnatal age) are shown for the sternum in Figure 3.6 for all patients and measurements in Table 3.1B, regardless of skin type. After random selection of one measurement event per patient, no to very little correlation can be observed between μ_s' and gestational maturity (Spearman $r^2 = 0.14$, $p < 0.05$) and μ_a and gestational

maturity (Spearman $r^2 = 0.12$, $p < 0.05$). The same holds for the correlation between μ_s' and gestational maturity at the other locations (Spearman r^2 of 0.22 (forehead), 0.11 (hand) and 0.29 (foot), $p < 0.05$) and the correlation between μ_a and gestational maturity (Spearman r^2 of 0.06 (forehead), 0.01 (hand) and 0.10 (foot), $p < 0.05$). Similar results were obtained at other wavelengths.

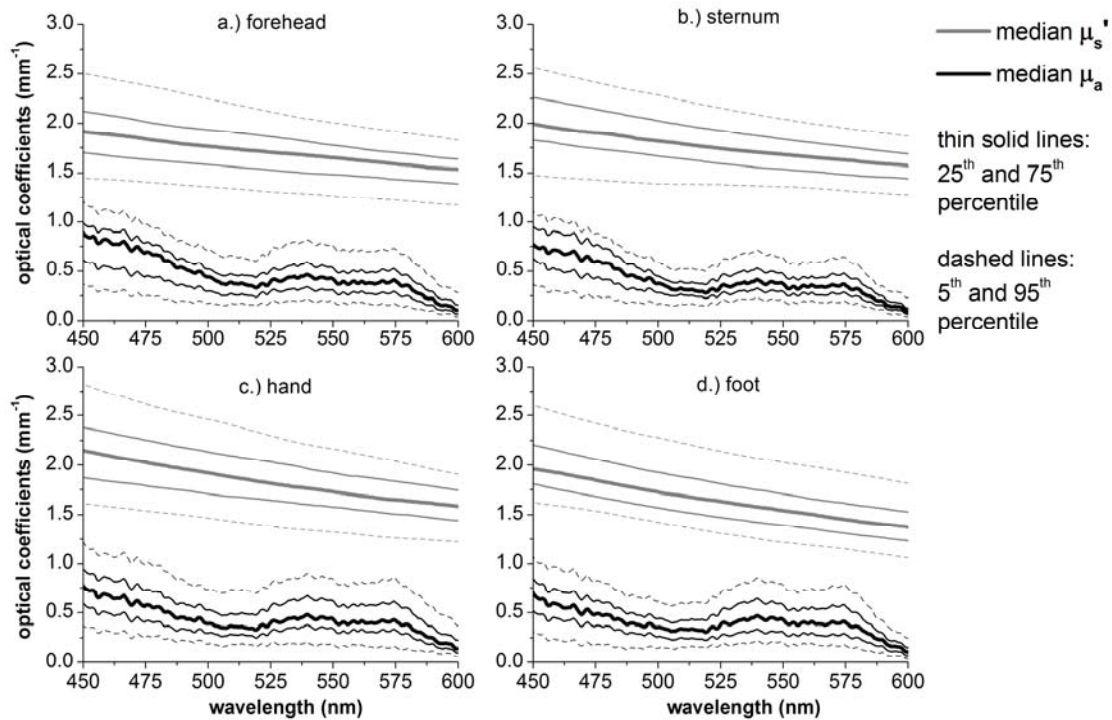


Figure 3.5 For a.) forehead, b.) sternum, c.) hand and d.) foot: median values and 5th, 25th, 75th and 95th percentiles for the measured μ_s' and μ_a vs. wavelength for all patient measurements within the validity limits (Table 3.1B).

3.4.2 Dependency on skin type

The median values of μ_a vs. wavelength are shown in Figure 3.7 for each skin type at the sternum (Figure 3.7a) and the foot (Figure 3.7b). Results for the forehead and the hand (no graph) were similar to those of the sternum. When only regarding the measurements that fall within the validity limits (solid lines, Table 3.1B), the multivariate analysis proved no significant ($p > 0.05$) influence of skin type on the measured optical properties, neither for μ_s' nor for μ_a . The latter is caused by exclusion of the highest μ_a values because of the the $\mu_a/\mu_s' \leq \frac{3}{4}$ validity limit, which is most abundant for patients with skin type 3 (Table 3.1). For the sternum, a larger difference in μ_a can be observed between the three skin types, if we analyze the median values of μ_a for all measurements in Table 3.1A (dotted lines, no elimination of measurements).

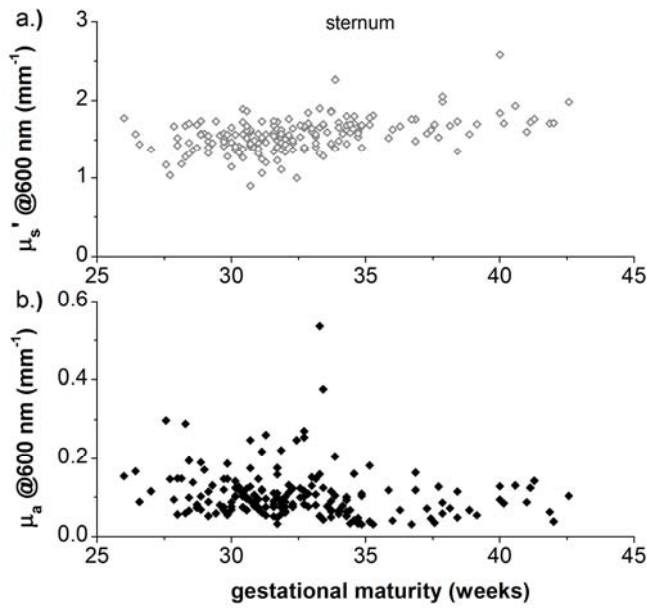


Figure 3.6 Measured values at $\lambda = 600 \text{ nm}$ of a.) μ_s' and b.) μ_a , versus gestational maturity (gestational + postnatal age) at the sternum, for all patient measurements within the validity limits (Table 3.1B).

This difference cannot be observed at the foot, which is likely to be due to the lack of melanin at this measurement site (plantar side of the foot). The results presented by the dotted lines in Figure 3.7 need to be interpreted with caution, because our model of analysis is not valid for these measurements. The presented values for μ_a are likely to be larger, considering the underestimation of μ_a for values beyond the $\mu_a/\mu_s' \leq \frac{3}{4}$ validity limit (Figure 3.2b). Hence, these results should be interpreted qualitatively (e.g. relative values, trends) rather than quantitatively.

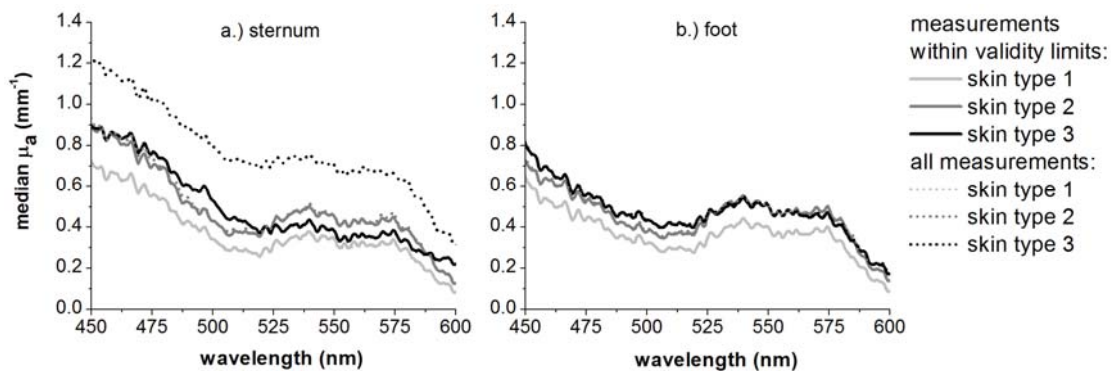


Figure 3.7 Median values of μ_a vs. wavelength at a.) the sternum (upper graphs) and b.) the foot (lower graphs) for all measurements (dashed lines, Table 3.1A) and measurements within the validity limits (solid lines, Table 3.1B). Difference is made between skin types (type 1: Caucasian, type 2: Mediterranean, type 3: Negroid).

The dependency of μ_a at $\lambda = 600$ nm on postnatal age is shown in Figure 3.8 at the sternum for each skin type. Also for these results, difference is made between the measurements where the validity limits are valid (closed symbols, Table 3.1B), and not valid (open symbols). A (qualitative) analysis of all measurements per skin type, yields a high correlation between the μ_a at 600 nm for skin type 3 and the postnatal age (Spearman $r^2 = 0.77$, $p < 0.05$). This can be ascribed to the stimulation of the production of melanin after birth [12]. The production of melanin for patients with skin type 2 and 1 is lower, resulting in less or no correlation with postnatal age (Spearman $r^2 = 0.18$ and 0.07 , respectively, $p < 0.05$). Similar trends in μ_a vs. postnatal age were observed for the forehead and hand. The μ_a of the foot for patients with skin type 3 did not depend as much on age (Spearman $r^2 = 0.43$, $p < 0.05$) as for the other locations, due the lower melanin production at the measurement site (plantar side of the foot). Similar results were obtained at other wavelengths.

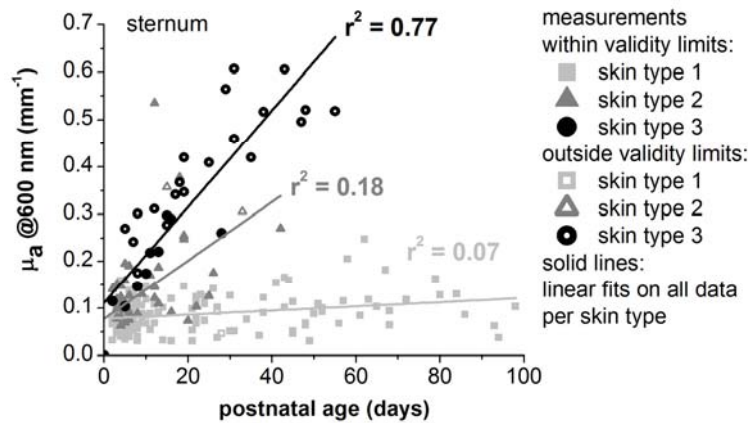


Figure 3.8 Measured values for μ_a at $\lambda = 600$ nm vs. postnatal age at the sternum, for all patient measurements within the validity limits (filled symbols, Table 3.1B) and outside the validity limits (open symbols). Difference is made between skin types (type 1: Caucasian, type 2: Mediterranean, type 3: Negroid).

3.4.3 OCT images of neonatal skin

Figure 3.9 a and b show typical OCT scans at 1310 nm of the skin at the foot of a patient (skin type 1, gestational age: 25 weeks, postnatal age: 56 days) and an adult (skin type 1, age: 25 years). No distinct layers can be observed in the skin of the neonate, which seems to extend beyond the imaging depth of approximately 1 mm. The skin of the adult shows more optical contrast between the individual skin layers and structures. Images at the sternum, forehead and hand gave similar results, as well as images for other patients and adults (results not shown).

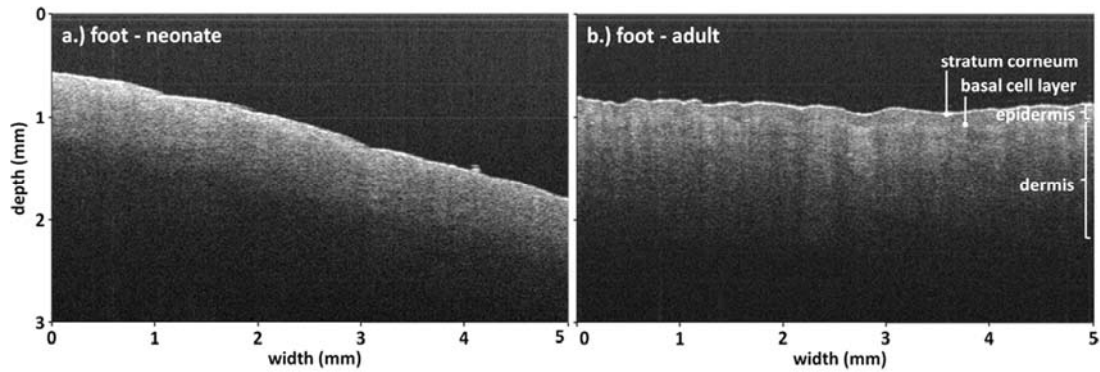


Figure 3.9 OCT scans (1310nm) of the skin at the plantar side of the foot of a neonate (skin type 1, gestational age: 25 weeks, postnatal age: 56 days) and an adult (skin type 1, age: 25 years).

3.5 Discussion

In this Chapter, we presented measurements of the optical properties of neonatal skin and assessed the influence of age and skin type on a large group of patients. This new knowledge on neonatal skin optical properties can aid to the development of optical techniques in neonatology. For instance, the measured values of μ_a and μ_s' can be used as input to Monte Carlo simulations of photon distributions inside the skin, which provide insight in e.g. optimal design for optical diagnostic probes.

3.5.1 Model validity - general

We used a spatially resolved, steady state diffuse reflectance spectroscopy setup and a steady state diffusion model to obtain the absorption and reduced scattering coefficient of the skin. Our method of analysis was validated in a phantom study (Section 3.3.1), by measuring μ_s' and μ_a of phantoms with known optical properties in the range of those of neonatal skin. We were able to measure μ_a with an accuracy of 15% and μ_s' with an accuracy of 10%, provided that the measurements were within the validity limits of the diffusion model ($\mu_a/\mu_s' \leq 3/4$ and $(\mu_a + \mu_s') > 0.8 \text{ mm}^{-1}$). Other studies that analyze the spatially diffuse tissue reflectance with a diffusion model, typically allow more constrained validity limits [7,8], thereby eliminating more measurements. Reasons for this difference may be the choice for larger uncertainty margins in the limits of validity and other study design, such as measurement geometry and method of analysis. If, for instance, we do not apply the scatter power fit on the first outcome of the diffusion model fit to the measured reflectance and merely look at $\mu_{a,1st}$ and $\mu_{s,1st}'$ (Section 3.2.3), the value of β will be considerably lower.

This use of spectral constraints in diffusion model based analysis was investigated before by Kim *et al* [13] for source-detector separations similar to ours, and was thought to be the cause of extended validity limits, comparable to the limits found in this study. Measuring optical properties at small source-detector separations (< 1 mm) is usually associated with non-diffuse photon distributions and requires adjustments with respect to common diffusion model based studies, either in measurement

geometry [14] and/or method of analysis [14,15]. In this study, the diffusion model of Farrel *et al* was modified to a semi-empirical model by correcting for the initial underestimation of the measured $\mu_s'_{2nd}$ (Figure 3.2a). This correction contributes to the validity of our analysis, as shown in our phantom study. We speculate that the initial underestimation of $\mu_s'_{2nd}$ may be caused by the back reflection of photons into the medium at the aluminum probe surface, which is not accounted for in the boundary conditions of the diffusion model [10]. This may result in a more diffuse photon distribution for the relatively short source-detector separations in our setup. Fortunately, the underestimation is consistent and does therefore not affect our determination of μ_s' , since the measured μ_s' agrees very well with the expected value for both Intralipid (Figure 3.2c) and polystyrene spheres after correction.

3.5.2 Model validity - patients

By using the diffusion model to analyze the optical properties of neonatal skin from the patient measurements, we implicitly assume that the probed volume consists of skin only, and is semi-infinite and homogeneous. It is known from literature that (preterm) neonatal skin exhibits no to little distinct variations between individual skin layers [16] and is therefore expected to be optically more homogeneous than adult human skin [17]. This difference in homogeneity between neonatal and adult skin is clearly reflected in the OCT images of Figure 3.9 a and b. The thickness of neonatal skin is not well reported in literature, but is expected to range between 0.65 and 1.5 mm [16,18]. Since the transition of the dermis into the subcutaneous tissue could not be observed in any of the OCT images of neonatal skin, we conclude that either no optical contrast exists between the dermis and the subcutaneous tissue (i.e. the optical coefficients are similar), or the skin thickness is larger than the imaging depth of the OCT system (approximately 1 mm). Therefore, we conclude that we measure the optical properties of skin only, since the probing depth of our system was assessed to be ~ 1 mm for a phantom comparable to neonatal skin (Section 3.3.2). Based on similar OCT images for other locations and patients (Section 3.4.3), we expect that our assumptions on homogeneity and semi-infinity are justified for all reported patient measurements. To further verify these assumptions, the optical properties would need to be measured at different depths in the tissue, which requires a small measurement volume from which the exact location inside the skin can be controlled. A potentially suited technique for this purpose is low-coherence spectroscopy (LCS) [19,20], although its performance *in vivo* has not yet been tested. LCS has the additional possibility of measuring the non-reduced scattering coefficient μ_s , instead of the reduced scattering coefficient μ_s' that is influenced by the scattering anisotropy g of the skin ($\mu_s' = \mu_s(1-g)$) [20].

3.5.3 Optical properties of neonatal skin

The optical properties of the skin of 60 patients were measured at the forehead, sternum, hand and foot. Comparison of the optical properties between the four measurement locations resulted in no significant differences. The spread of the optical properties is narrow for every location (Figure 3.5), ranging maximally 1.5 mm^{-1} between the 5th and 95th percentile of all measurements. However, this spread may be skewed, since the selection of patient measurements based on the validity limits results

in a reduction of measurements (Table 3.1). As a consequence, the lowest μ_s' values and the highest μ_a values are neglected in our presentation of the optical properties of neonatal skin (Figures 3.5 and 3.6). Figure 3.7 shows that the presented median values for μ_a of patients with skin type 3 should therefore be interpreted with caution, because μ_a changes considerably if the validity limits are neglected. Again, we would like to emphasize that the optical properties outside the validity limits should receive qualitative, rather than quantitative interpretation. For patients with skin type 1 and 2, very little measurements are lost and the presented values of μ_a can be trusted.

In line with the results of Saidi [4], the measured absorption coefficient spectra seem to contain mainly the contribution of oxygenized and deoxygenized hemoglobin, bilirubin and melanin. Laboratory analysis of sampled blood for a selection of patients yielded total hemoglobin levels in the range of 5 to 13 mmol/L and total serum bilirubin levels in the range of 40 to 400 $\mu\text{mol/L}$. The concentration of hemoglobin and bilirubin in the investigated tissue volume is affected by vessel density and bilirubin extravasation, and is therefore expected to be lower than in whole blood. The magnitude of the measured μ_a agrees well with the results of Saidi, who reported a range of approximately 0.2 to 1.3 mm^{-1} between 450 and 600 nm. More differences are found when comparing the measured values of μ_s' between this study and Saidi *et al* [4,5]. The reported average values of μ_s' by Saidi between 450 and 600 nm are considerably higher ($\sim 2\text{-}4 \text{ mm}^{-1}$ [4]) than the median values of μ_s' presented in this study (Figure 3.5) and the spread of the data of Saidi is larger (standard deviation of $\sim 3.6 \text{ mm}^{-1}$ at 450 nm). Another remarkable difference exists in the dependency of μ_s' on gestational maturity. Whereas we found no to weak correlation between μ_s' and gestational maturity (Figure 3.6a), Saidi *et al* found much stronger correlation, which they ascribed to an increase of collagen fiber density in the skin during maturation [5]. Although small differences exist between the investigated patient populations and skin areas (abdomen in the study of Saidi) and not all of these results were published in peer reviewed journals [4], it is most likely that the observed differences in μ_s' are caused by unavoidable sample preparation procedures [6] for the *in vitro* tissue study of Saidi. However, it is expected that μ_s' will increase at a certain age outside the investigated age range in this study, since μ_s' is considerably higher for adult skin (3 – 9 mm^{-1} , measured *in vitro* between 450 – 600 nm) [21].

The measured values of μ_a for neonatal skin are comparable to adult skin (0.2 – 1 mm^{-1} between 450 – 600 nm) [21]. The absorption coefficient at 600 nm did not depend on gestational maturity, but did depend on postnatal age for patients with skin type 2 and 3 (Figure 3.8). This can be ascribed to the stimulated production of melanin after birth [12]. It is not expected that the suggested linear relation in Figure 3.8 will hold for all ages, because the increase of μ_a will level off at a certain age, which is approximately six months for neonates with a dark skin type [12]. Since melanin is located in the epidermal layer of the skin, the skin will be an optically layered medium for pigmented skin areas in neonates with high postnatal age. The homogeneity shown in the OCT scans of Figure 3.9 will therefore be lost. The reader should keep this in mind when using the presented optical properties, as well as the underestimation of μ_a for patients with a dark skin type. An increase of absorption due to tanning of the skin has also been described for neonates (gestational age ≥ 35.5 weeks) with skin type 1, receiving photo therapy [22]. Although the majority of our patient population with skin type 1 received

photo therapy during the measurement period, no increase of μ_a at 600 nm was observed for these patients (Figure 3.6b).

3.6 Conclusion

We measured *in vivo* the absorption and reduced scattering coefficients of neonatal skin for a large group of patients with varying gestational age, postnatal age and skin pigmentation. The optical properties did not differ significantly between different locations on the body (forehead, sternum, hand and foot). No to very weak correlation was observed between the optical properties and gestational maturity, but a strong dependency of the absorption coefficient on postnatal age existed for patients with skin type 3 (Negroid), which can be ascribed to the production of melanin after birth.

Knowledge of the optical properties of neonatal skin is invaluable when developing new, or improving existing optical diagnostic and therapeutic procedures that are used at the neonatal intensive care. We therefore hope that the results presented in this Chapter can contribute to the future development and improvement of these techniques.

References

1. K. Grohmann, M. Roser, B. Rolinski, I. Kadow, C. Müller, A. Goerlach-Graw, M. Nauck, H. Küster, "Bilirubin measurement for neonates: comparison of 9 frequently used methods", *Pediatrics* **117**, 1174-1183 (2006)
2. J.W. Salyer, "Neonatal and pediatric pulse oximetry", *Respiratory Care* **48**, 386-398 (2003)
3. M. Kaplan, V. Gold, C. Hammerman, A. Hochman, D. Goldschmidt, H.J. Vreman, D.K. Stevenson, "Phototherapy and photo-oxidation in premature neonates", *Biology of the Neonate* **87**, 44-50 (2005)
4. I.S. Saidi, "Optical properties of neonatal skin", Chap. 2 in Master Thesis: *Light transport in neonatal skin*, Rice University, Houston, TX (1990)
5. I.S. Saidi, S.L. Jacques, F.K. Tittel, "Mie and Rayleigh modeling of visible-light scattering in neonatal skin", *Appl. Opt.* **34**, 7410-7418 (1995)
6. R. Graaff, A.C. M. Dassel, M.H. Koelink, F.F.M. de Mul, J.G. Aarnoudse, W.G. Zijlstra, "Optical properties of human dermis in vitro and in vivo", *Appl. Opt.* **32**, 435-447 (1993)
7. R.M.P. Doornbos, R. Lang, M.C. Aalders, F.W. Cross, H.J.C.M. Sterenborg, "The determination of in vivo human tissue optical properties and absolute chromophore concentrations using spatially resolved steady-state diffuse reflectance spectroscopy", *Physics in Medicine and Biology* **44**, 967-981 (1999)
8. M.G. Nichols, E.L. Hull, T.H. Foster, "Design and testing of a white-light, steady state diffuse reflectance spectrometer for determination of optical properties of highly scattering systems", *Appl. Opt.* **36**, 93-104 (1997)
9. D. Arifler, C. MacAulay, M. Follen, R. Richards-Kortum, "Spatially resolved reflectance spectroscopy for diagnosis of cervical precancer: Monte Carlo modeling and comparison to clinical measurements", *Journal of Biomedical Optics* **11**, 064027 (2006)
10. T.J. Farrell, M.S. Patterson, B. Wilson, "A diffusion theory model of spatially resolved, steady-state diffuse reflectance for the noninvasive determination of tissue optical properties", *Med. Phys.* **19**, 879-888 (1992)
11. H.J. van Staveren, C.J.M. Moes, J. van Marle, S.A. Prahl, M.J.C. van Gemert, "Light scattering in Intralipid-10% in the wavelength range of 400-1100 nm", *Appl. Opt.* **30**, 4507-4514 (1991)
12. R.J. Walsh, "Variation in the melanin content of the skin of New Guinea natives at different ages", *Journal of Investigative Dermatology* **42**, 261-265 (1964)

13. A. Kim, R. Mathieu, F. Dadani, B.C. Wilson, "A fiberoptic reflectance probe with multiple source-collector separations to increase the dynamic range of derived tissue optical absorption and scattering coefficients", *Optics Express* **18**, 5580-5594 (2010)
14. S. Tseng, C. Hayakawa, J. Spanier, A.J. Durkin, "Investigation of a probe design for facilitating the uses of the standard photon diffusion equation at short source-detector separations: Monte Carlo simulations", *Journal of Biomedical Optics* **14**, 054043 (2009)
15. N. Rajaram, R.H. Nguyen, J.W. Tunnell, "Lookup table-based inverse model for determining optical properties of turbid media", *Journal of Biomedical Optics Letters* **13**, 050501 (2008)
16. Y.B. Chiou, U. Blume-Peytavi, "Stratum corneum maturation – a review of neonatal skin function", *Skin Pharmacology and Physiology* **17**, 57-66 (2004)
17. J. Welzel, "Optical coherence tomography in dermatology: a review", *Skin Research and Technology* **7**, 1-9 (2001)
18. P.H. Hoeger, "Physiology of neonatal skin", Chap. 2 in *Textbook of pediatric dermatology*, J. Harper, A. Oranje, N. Prose, Eds., pp. 42-47, Blackwell Publishing, Oxford, UK (2006)
19. N. Bosschaart, M.C.G. Aalders, D.J. Faber, J.J.A. Weda, M.J.C. van Gemert, T.G. van Leeuwen, "Quantitative measurements of absorption spectra in scattering media by low-coherence spectroscopy", *Optics Letters* **34**, 3746-3748 (2009)
20. N. Bosschaart, D.J. Faber, T.G. van Leeuwen, M.C.G. Aalders, "Measurements of wavelength dependent scattering and backscattering coefficients by low-coherence spectroscopy", *Journal of Biomedical Optics Letters* **16**, 030503 (2011)
21. E. Salomatina, B. Jiang, J. Novak, A.N. Yaroslavsky, "Optical properties of normal and cancerous human skin in the visible and near-infrared spectral range", *Journal of Biomedical Optics* **11**, 064026 (2006)
22. L.L. Randeberg, E.B. Roll, L.T.N. Nilsen, T. Chrystensen, L.O. Svaasand, "In vivo spectroscopy of jaundiced newborn skin reveals more than a bilirubin index", *Acta Paediatrica* **94**, 65-71 (2005)

CHAPTER 4

Quantitative measurements of absorption spectra in scattering media by low-coherence spectroscopy

Low Coherence Spectroscopy (LCS) is a novel spectroscopic method that allows for quantitative and localized assessment of absorption spectra by combining reflection spectroscopy with low coherence interferometry. We describe absorption coefficient (μ_a) measurements by LCS in tissue simulating phantoms with varying scattering and absorbing properties. We used LCS in the 455–680 nm wavelength range with a spectral resolution of 8 nm to obtain μ_a spectra with $\pm 0.5 \text{ mm}^{-1}$ accuracy. We conclude that LCS is a promising technique for the *in vivo* determination of tissue chromophore concentrations.

Part of this work has been published in: N. Bosschaart, M.C.G. Aalders, D.J. Faber, J.J.A. Weda, M.J.C. van Gemert and T.G. van Leeuwen, "Quantitative measurements of absorption spectra in scattering media by low-coherence spectroscopy", *Optics Letters* 34(23), 3746-3748 (2009)

4.1 Introduction

Optical spectroscopy for *in vivo* determination of chromophore concentrations (e.g. hemoglobin and bilirubin) offers an alternative to frequent and invasive drawing of blood followed by time consuming laboratory analysis. However, due to lack of knowledge of the optical path in tissue, the current clinically applied spectroscopic techniques such as elastic scattering, absorption and differential path length spectroscopy [1-3] depend on photon path length models for the determination of absolute chromophore concentrations. Another limitation is the lack of localization [1,2], i.e. the measured signal originates from a large volume, which makes it difficult to confine the measurement to a preferred target volume such as the microcirculation in the skin. *Quantitative* (i.e. absolute concentrations) and localized spectroscopic measurements of tissue chromophores require knowledge of (or control over) the path length of light in tissue, because then tissue absorption coefficients, which are directly related to chromophore concentrations, can be calculated using Beer's law.

In this Chapter, we demonstrate for the first time that low-coherence spectroscopy (LCS) allows for quantitative assessment of absorption spectra in scattering media as a first step toward non-invasive *in vivo* tissue chromophore concentration measurements. LCS combines reflection spectroscopy with low coherence interferometry (LCI) to control the path length of the detected light. To validate this method, we performed *in vitro* measurements of absorption coefficient spectra on samples with known absorption and scattering properties.

LCS is a novel extension of LCI and can therefore be placed alongside techniques such as optical coherence tomography (OCT) and path length resolved optical Doppler measurements [4]. LCS recovers spectroscopic information at controlled path lengths from the sample, similar to spectroscopic OCT (sOCT) [5-8]. However, LCS is fully optimized for spectroscopy, instead of tomography. This allows a system design with high spectral resolution at the sacrifice of spatial resolution. Also, sampling intervals can be optimized for spectroscopic purposes and the measurement volume can be enlarged for better signal to noise ratios. Our LCS system operates in the visible wavelength range, because of the distinct features of important chromophores such as bilirubin and hemoglobin in this region, compared to the near infrared region (NIR). Hence, chromophore concentration alterations induce more pronounced changes in absorption. In sOCT, spectroscopy is combined with imaging, which limits the available wavelengths to the NIR to obtain sufficient imaging depth. Other path length resolved spectroscopic methods, such as time of flight [9] and phase resolved spectroscopy [10] measure the optical path length, rather than controlling it. In addition, their range of validity is limited to large path lengths, which compromises localization.

4.2 Theory

The LCS system described in this thesis is based on a Michelson interferometer (Figure 4.1). Low-coherent light originating from the source is divided by a beam splitter into a sample arm and a reference arm, with lengths x_S and x_R , respectively. Back scattering of photons by the sample in the sample arm results in a sample arm field E_S , and back

reflection of photons by a mirror in the reference arm results in a reference arm field E_R . Both fields recombine at the beam splitter and are guided towards a photo detector, where they interfere.

The photo detector current i_D is proportional to the square of the optical field at the detector E_D^2 :

$$i_D \propto \langle |E_D|^2 \rangle \propto \langle |E_S + E_R|^2 \rangle \propto \langle |E_S|^2 + |E_R|^2 + 2E_S E_R \rangle \quad (4.1)$$

in which the triangular brackets denote integration over the detector response time. The latter part of this expression, $2E_S E_R$, denotes the interferometric portion of the signal, i.e. the AC part of the detector current:

$$i_{AC} \propto \langle 2E_S E_R \rangle \quad (4.2)$$

This interferometric signal is directly related to the time (t) dependent optical path length difference between the sample arm and the reference arm, $\Delta L(t) = 2(x_S(t) - x_R(t))$. In the case of a monochromatic light source, $i_{AC}(t)$ can be described by:

$$i_{AC}(t) \propto 2\sqrt{I_S(\Delta L(t)) \cdot I_R} \cdot \cos(k \cdot \Delta L(t)) \quad (4.3a)$$

where I_S and I_R are the signal intensities in the sample and reference arm, respectively, and k is the wavenumber ($k=2\pi/\lambda$, with wavelength λ) [11].

In the case of a broad band, or low-coherent light source, $i_{AC}(t)$ is integrated over the source spectrum:

$$i_{AC}(t) \propto 2 \int \sqrt{I_S(k, \Delta L(t)) \cdot I_R(k)} \cdot \cos(k \cdot \Delta L(t)) \cdot dk = \sqrt{I_S(\Delta L(t)) \cdot I_R} \cdot \cos(k_0 \cdot \Delta L(t)) \quad (4.3b)$$

in which k_0 is the center wave number of the source spectrum. As a consequence, interference between E_S and E_R can only be observed within the coherence length l_c of the source, which is the limiting axial resolution at which $i_{AC}(t)$ can be acquired (assuming a Gaussian shaped source spectrum):

$$l_c = \frac{2 \ln 2}{\pi} \frac{\lambda_0^2}{\lambda_{FWHM}} \quad (4.4)$$

with λ_0 the center wavelength of the source spectrum and λ_{FWHM} the bandwidth, or full width at half maximum (FWHM) of the source spectrum [11].

The broad bandwidth of a low-coherent source can be used for spectroscopic purposes, which is the basic principle of LCS. Hence, we are interested in the frequency content (which is related to wavelength in LCS) of the signal i_{AC} . Therefore, we regard the power spectrum $S(f)$ of $i_{AC}(t)$, obtained by Fourier transformation of $i_{AC}(t)$:

$$S(\lambda) : \Leftrightarrow S(f) = \left| \mathfrak{F}\{i_{AC}(t)\} \right|^2 \quad (4.5)$$

In the remaining part of this Chapter, all wavelength dependent parameters will be indicated by a bold faced character, e.g $\mathbf{S} = S(\lambda)$.

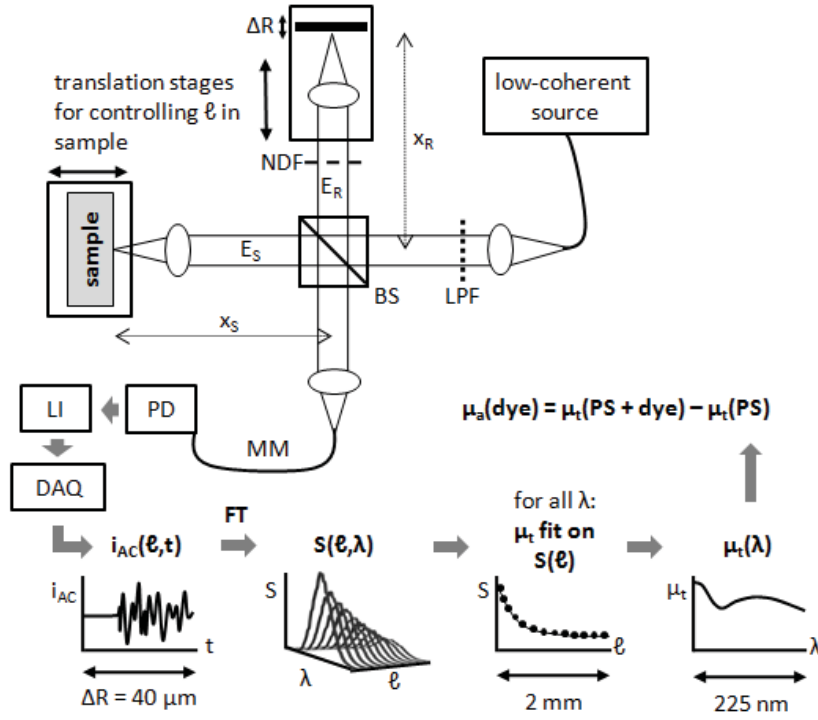


Figure 4.1 The LCS system (upper part) and a schematic overview of the signal processing (lower part). E_S/E_R : optical field in sample/reference arm, x_S/x_R : length of sample/reference arm, LPF: low pass filter, BS: beam splitter, NDF: neutral density filter, ΔR : scanning range of the piezo driven reference mirror, MM: multimode graded index detection fiber, PD: photo diode, LI: lock-in amplifier, DAQ: data acquisition card, i_{AC} : interferometric photo detector current, t : time, FT: Fourier transform, ℓ : geometrical optical path length in the sample, λ : wavelength, S : power spectrum, μ_t/μ_a : attenuation/absorption coefficient, PS: polystyrene spheres

The time dependency of ΔL in Eq. 4.3 a and b is caused by the linear translation of the mirror in the reference arm, which moves triangularly with a frequency f_R and a range ΔR , resulting in a velocity $v_R = 2f_R\Delta R$. This movement causes Doppler shifting of the reference arm field, resulting in a frequency modulation on $i_{AC}(t)$. Hence, it provides us with the relation between f and λ :

$$f = \frac{2v_R}{\lambda} = \frac{4f_R\Delta R}{\lambda} \quad (4.6)$$

The scanning range ΔR results in a roundtrip (geometrical) path length scanning window $\Delta\ell$ within the sample:

$$\Delta\ell = \frac{2\Delta R}{n_g} \quad (4.7)$$

with n_g the group refractive index of the medium. A single spectrum S is obtained from the $i_{AC}(t)$ within this scanning window (Eq. 4.5), over a time interval of $1/(2f_R)$. The axial

resolution at which \mathbf{S} is acquired ($\frac{1}{2}\Delta\ell$) is therefore $\Delta R/l_c$ times larger or ‘worse’ than the axial resolution at which $i_{AC}(t)$ can be acquired (l_c/n_g).

The spectral resolution $\Delta\lambda$ of \mathbf{S} can be derived by differentiating f to λ and by using Eq. 4.6:

$$\frac{df}{d\lambda} = -\frac{4f_R\Delta R}{\lambda^2} \Rightarrow \Delta\lambda = \left| -\frac{\lambda^2\Delta f}{4f_R\Delta R} \right| \quad (4.8)$$

In Eq. 4.8, Δf denotes the resolution in the frequency domain. Due to the time-frequency Fourier pair in Eq. 4.5 and the Nyquist criterium ($f_s < 2f$), $\Delta f = f_s/N$, with f_s the sampling frequency at which $i_{AC}(t)$ is acquired and N the number of samples. Since all N samples are acquired within one sweep of the reference mirror, $f_s = 2f_R N$ and hence, $\Delta f = 2f_R$. Substitution into Eq. 4.8 results in:

$$\Delta\lambda = \frac{\lambda^2}{2\Delta R} \quad (4.9)$$

In summary, we end up with a spectrum \mathbf{S} that is acquired over an optical path length interval $\Delta\ell$ with spectral resolution $\Delta\lambda$. The spectrum \mathbf{S} is *localized*, since $\Delta\ell$ determines the sample volume from which \mathbf{S} is acquired and the optical path length difference ΔL between the sample and reference arms determines the depth from which \mathbf{S} is acquired in the sample. Eq. 4.8 shows that a trade-off exists between the spectral and spatial resolution of \mathbf{S} . Hence, ΔR should be chosen small enough to adequately probe the sample’s spatial variation, but large enough to obtain a $\Delta\lambda$ that is sufficient to retrieve the spectral features of interest in \mathbf{S} .

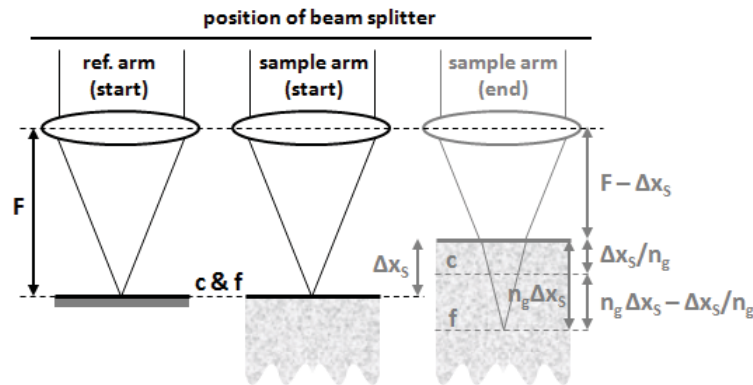


Figure 4.2 Schematic illustration of the focus tracking process. Start: the position of the coherence gate (c) and the focus (f) are matched at the sample surface. End: the sample is shifted with Δx_s towards the sample lens, which induces a mismatch between the positions of the focus and the coherence gate in the sample. Adjusting the reference arm length with $\Delta x_R = \Delta x_s(n_g^2 - 1)$ rematches the positions of the focus and the coherence gate (see text).

To determine the optical coefficients of the sample, multiple spectra \mathbf{S} are required, originating from different roundtrip geometrical path lengths ℓ (or depths $d = \ell/2$) within the sample. The geometrical path length ℓ in the sample is determined by ΔL . In this thesis, we control ΔL by varying the length of the sample arm, i.e. we displace the sample towards the sample lens with interval Δx_s , resulting in a geometrical path length shift of $\ell = 2n\Delta x_s$. Figure 4.2 illustrates the shifts in the positions of the focus ($n_g\Delta x_s$) and the location from which we acquire $i_{AC}(t)$ ($\Delta x_s/n_g$, i.e. the coherence gate) induced by a sample displacement Δx_s . In order to realign the focus with the coherence gate, we elongate the length of the reference arm with $\Delta x_R = n_g \cdot (n_g\Delta x_s - \Delta x_s/n_g) = \Delta x_s(n_g^2 - 1)$, more commonly known as ‘focus tracking’ [7].

Acquiring \mathbf{S} at multiple path lengths ℓ within the sample results in a dataset $\mathbf{S}(\ell)$ which is illustrated in Figure 4.1. When the acquired $i_{AC}(t)$ is dominated by single scattered light, \mathbf{S} decays exponentially with ℓ , which is described by Beer’s law [12]:

$$\mathbf{S}(\ell) \propto \mathbf{S}_0 \cdot e^{-\mu_t \cdot \ell} \quad (4.10)$$

in which \mathbf{S}_0 is the source power spectrum and μ_t is the attenuation coefficient of the sample, which is the sum of the absorption coefficient μ_a and scattering coefficient μ_s of the sample:

$$\mu_t = \mu_a + \mu_s \quad (4.11)$$

The values of μ_a and μ_s can be obtained by separating their individual contributions to μ_t as described in Section 4.3.2 and Chapter 6.

4.3 Materials and methods

4.3.1 System and acquisition

Our LCS system (Figure 4.1) consists of a Michelson interferometer with a low pass filtered supercontinuum light source (SC430-4, Fianium Ltd., UK). The system is optimized for a bandwidth of 455 – 680 nm, resulting in a coherence length of $\sim 1.5 \mu\text{m}$ (Eq. 4.4). The light is focused by 25 mm focal length achromatic lenses on the sample and a piezo-driven reference mirror. The reference arm power can be adjusted with a neutral density filter in the reference arm and the optical power at the sample is 2.5 mW. Both the sample and the reference mirror are mounted on motorized translation stages which are used for controlling ℓ of the light in the sample ($\ell = 0 - 2 \text{ mm}$, in steps of $27 \mu\text{m}$). Around ℓ , the signal is modulated by scanning the piezo-driven reference mirror at 23 Hz over a range of $\Delta R = 40 \mu\text{m}$. Non-linearities in reference mirror velocity are avoided by excluding the edges of the piezo sweep, resulting in an effective scanning range of $30 \mu\text{m}$ and a scanning window of $\Delta\ell \approx 44 \mu\text{m}$ within the sample (Eq. 4.7, with group refractive index $n_g = 1.35$ for aqueous solutions of polystyrene spheres, see below). Focus tracking, as described in Section 4.2, was ensured. The depth of focus of the sample arm lens is $60 \mu\text{m}$ in air.

A graded index multimode fiber ($\emptyset 62.5 \mu\text{m}$, NA=0.27, length $L = 1.1 \text{ m}$, $n_{\text{core}} \approx 1.5$, M31L01 Thorlabs, USA) guides the reflected light from both arms to a photodiode

(2001, New Focus, USA). Multimode detection sacrifices spatial resolution compared to single mode detection, but makes the system less sensitive to changes in sample geometry that affect the spectral bandwidth of the light coupled into the detection fiber. A schematic overview of the signal processing after acquisition is given in Figure 4.1. The time signal is band pass filtered by the photodiode (1-10 kHz) and demodulated by a lock-in amplifier at the spectral center frequency of 6690 Hz with a low pass frequency of 5 kHz, corresponding to a center wavelength of 550 nm and a bandwidth of 410 nm. Per scanning window, 512 samples of amplitude and phase are digitized by a 12-bit data acquisition card (USB-6009, National Instruments, USA) and multiplied by a Hanning window before applying a Fourier transform to obtain $S(\ell)$ (Eq. 4.5). The frequency axis f of the Fourier spectrum is converted to wavelength using Eq. 4.6, with $v_R = 1.84$ mm/s. Correct wavelength mapping of the spectra was verified using two narrow band pass filters at wavelengths of 510 and 577 nm. For the scanning window $\Delta\ell$ of 44 μm , the spectral resolution is $\Delta\lambda \approx 8$ nm at 680 nm (Eq. 4.9).

For each geometrical path length ℓ , the average of 400 measured spectra $S(\ell)$ is binned into wavelength regions of 8 nm to obtain equidistant data points for $S(\ell)$. Attenuation coefficients per wavelength region μ_t are determined by fitting Eq. 4.10 to $S(\ell)$ vs. ℓ (from $\ell = 80$ to 2000 μm), using a nonlinear least squares fitting algorithm. The accuracy in μ_t is quantified by the 95% confidence intervals (c.i.) of the fitted μ_t [5]. The signal to noise ratio (SNR) was 112 dB, measured on the time signal of the reflection from a mirror in the sample arm, which was attenuated by a 3.0 optical density filter.

4.3.2 Samples

We prepared two sets of samples with three different concentrations of scattering polystyrene spheres (20%, 10% and 5% dilutions from a stock of 25 mg/ml, 392 nm diameter, KI-PPS-0.4, G. Kisker GbR, Germany). Mie calculations gave an anisotropy of $g = 0.78$ and scattering coefficients of 10.9 mm^{-1} , 5.5 mm^{-1} and 2.7 mm^{-1} at the center wavelength. The first set contained only the three concentrations of polystyrene spheres; the second set contained the same concentrations of polystyrene spheres as the previous set, but also a fixed concentration of absorbing green dye (37.5% Ecoline #600, Royal Talens, The Netherlands).

The attenuation coefficient is the sum of the scattering and absorption coefficients μ_s and μ_a of the sample (Eq. 4.11). A straightforward method to derive the μ_a from the samples with dye, is by subtracting μ_s from the measured μ_t . Hence, for each sample pair (absorbing/non-absorbing) with identical concentration of polystyrene spheres (i.e. identical μ_s), we subtracted the μ_t of the non-absorbing sample from the μ_t of the absorbing sample (Figure 4.1).

An absorption spectrum of the dye only was determined in a separate transmission measurement by a spectrograph (USB4000, Ocean Optics, USA) for validation of the measured μ_a . Since Brownian motion of the polystyrene spheres causes Doppler broadening of the LCS spectra, we equally broadened the μ_a transmission spectrum to enable adequate comparison between the two. The average Doppler frequency shift Δf_D induced by the Brownian motion of a sphere with radius r is given by $(4k_B \cdot T \cdot n^2)/(3\eta \cdot r \cdot \lambda^2)$, with k_B the Boltzmann constant ($\text{m}^2 \cdot \text{kg} \cdot \text{s}^{-2} \cdot \text{K}^{-1}$), T the temperature (K), n the refractive index of the medium and η the viscosity of the medium ($\text{kg} \cdot \text{m}^{-1} \cdot \text{s}^{-1}$) [4,13]. For the

polystyrene spheres in this Chapter, $\Delta f_D = 167$ Hz, which corresponds to a wavelength broadening of 14 nm around the center wavelength of 550 nm. Hence, broadening of the μ_a transmission spectrum was achieved by convolution with a Lorentzian with a line width of 14 nm [4,13].

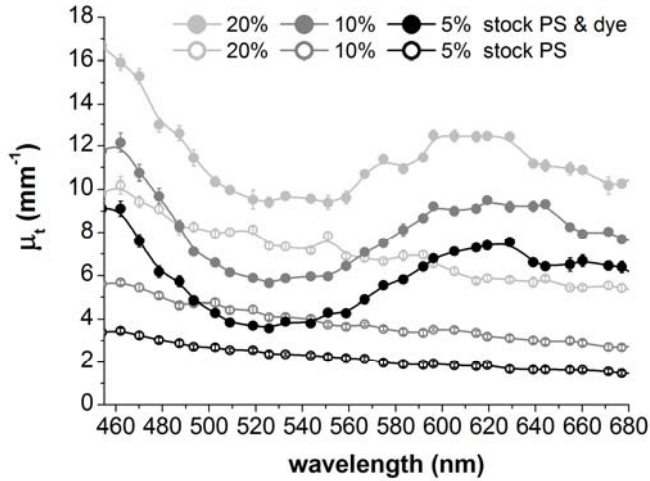


Figure 4.3 Attenuation spectra for three concentrations of polystyrene spheres (PS) with and without dye. Error bars represent the 95% c.i. of the fitted values. The lines through the data points are drawn as a guide to the eye.

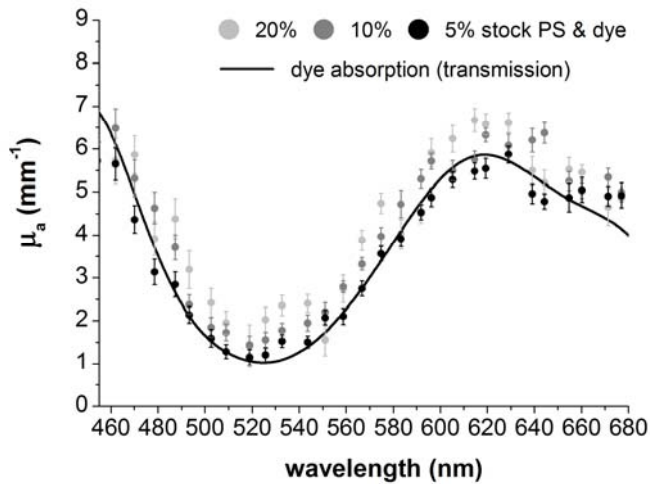


Figure 4.4 Absorption spectra for three samples with varying concentrations of polystyrene spheres (PS), but constant concentration of absorbing dye. Error bars represent the 95% c.i. of the fitted values.

4.4 Results

The measured attenuation spectra of the six samples are shown in Figure 4.3. The determined attenuation coefficients demonstrate the feasibility of LCS to extract the μ_t with an accuracy of $\pm 0.25 \text{ mm}^{-1}$. For the non-absorbing samples (only polystyrene spheres), the μ_t scale linearly with the concentration and all lie within the range of scattering coefficients of tissues [14].

The absorption spectra of the green dye derived from the three pairs of scattering samples are shown in Figure 4.4. Due to error propagation of the 95% c.i. in the subtraction, the accuracy for μ_a is approximately twice the accuracy of the μ_t determination ($\pm 0.5 \text{ mm}^{-1}$). The three spectra overlap within 2 mm^{-1} , which suggests that our method of determining μ_a holds for a broad range of scattering coefficients. Furthermore, the spectra show good agreement within 1.5 mm^{-1} with μ_a of the dye only (Figure 4.4, solid line).

4.5 Discussion and conclusion

In the preceding analysis of μ_a we assumed that the LCS signal from the non-absorbing samples decays exponentially with $\mu_s \times \ell$. Because our detection geometry may not be optimized to reject multiple scattered light (weak confocality because of low NA optics and the multimode detection fiber), the observed decay with ℓ can be shallower than predicted by μ_s . The separation of μ_s and μ_a by the subtraction of μ_t from a non-absorbing sample can still be applied, because absorption takes place along the photon's controlled path and therefore attenuates according to Beer's law [4,15].

The wavelength dependence of the sample's phase refractive index causes dispersion of the time signal, which leads to an increase of the axial resolution for large path lengths inside the sample. Correct acquisition of \mathbf{S} requires that the dispersed time signal is still sampled within our scanning window, i.e. the axial resolution ($l_c/n_g \approx 1.1 \text{ }\mu\text{m}$) at which we acquire $i_{AC}(t)$ is smaller than the axial resolution ($\frac{1}{2}\Delta\ell$) at which we acquire \mathbf{S} (Section 4.2). According to Hizenberger *et al* [16], the broadened axial resolution at a depth d in the sample is given by:

$$\frac{l_{c,\text{dispersed}}}{n_g} = \frac{1}{n_g} \sqrt{l_c^2 + (GD \cdot d \cdot \lambda_{FWHM})^2} \quad (4.12)$$

with GD the group dispersion of the sample. GD is determined by the second derivative of the phase refractive index of the sample [17]: $GD = -\lambda_0 \cdot (d^2n/d\lambda^2)$. For our system, this leads to an increase of the axial resolution of $i_{AC}(t)$ from $1.1 \text{ }\mu\text{m}$ to $8 \text{ }\mu\text{m}$ when the path length is set at 2 mm ($d = 1 \text{ mm}$). Since the dispersed $i_{AC}(t)$ will still be sampled within the axial resolution of \mathbf{S} ($22 \text{ }\mu\text{m}$), sample dispersion will not affect the power spectrum and hence, our calculation of μ_t .

Besides sample dispersion, intermodal dispersion may occur between the modes that are guided through the multimode detection fiber. The maximum number of modes M that can be guided through our multimode detection fiber is ~ 2300 , since $M \approx (\pi \cdot r \cdot NA / \lambda_0)^2$, with r the radius and NA the numerical aperture of the fiber [18]. The

modal dispersion between the first and the last mode is given by $L \cdot (NA/n_{\text{core}})^4 / 16 \approx 70 \mu\text{m}$ for our system [18], resulting in a dispersion of $70/M \approx 0.03 \mu\text{m}$ between two subsequent modes. Hence, the majority of elongated path lengths due to intermodal interference is sampled within our scanning window of $44 \mu\text{m}$ and we speculate that this effect has no substantial influence on our calculation of μ_t . In addition, we compared the system performance using a multimode detection fiber to the performance using a single mode detection fiber. This comparison gave no substantial difference in dynamic range and outcome of the μ_t measurement, indicating that modal dispersion and intermodal interference have no significant effect on our measurements.

The current accuracy of $\pm 0.5 \text{ mm}^{-1}$ of our determination of μ_a will be sufficient to measure biological variation in absorption, e.g. a 6% oxygenation change or a 2% change in hemoglobin concentration in whole blood in our wavelength range [14]. However, the variation in the absorption spectra in Figure 4.4 suggest that the accuracy may be worse than predicted by the 95% c.i.. Thus to improve the clinical value, the accuracy must be improved. Furthermore, obtaining a reference spectrum may be challenging *in vivo*, but alternative methods to separate scattering and absorption from a single attenuation profile have been proposed [2,6].

Whereas in this Chapter μ_a is measured in non-layered, homogeneous samples, LCS has potential to measure μ_a in individual layers of layered media such as human skin. The controlled path length and the confined measurement volume due to the confocality of the system, in principle allow to measure within a layer of choice. In complex media, where more than one chromophore contributes to the measured μ_a , methods such as multivariate analysis [1] are required to obtain the contribution of each individual chromophore.

In conclusion, we present absorption spectra from back scattered signals of polystyrene sphere solutions with green absorbing dye, with μ_s and μ_a within the physiological range of tissue. Our method applies for a broad range of scattering coefficients and agrees with transmission spectroscopy. Compared to other spectroscopic techniques, LCS controls the path length of the detected light inside a sample, which enables both quantitative and potentially localized measurements of absorption coefficients. Since absorption coefficients are directly related to chromophore concentrations, LCS is a promising technique for *in vivo* determination of tissue chromophore concentrations in individual tissue layers.

References

1. P. Rolfe, "In vivo near-infrared spectroscopy", *Annual Review of Biomedical Engineering* **2**, 715-754 (2000)
2. M.G. Nichols, E.L. Hull, T.H. Foster, "Design and testing of a white-light, steady state diffuse reflectance spectrometer for determination of optical properties of highly scattering media", *Applied Optics* **36**, 93-104 (1997)
3. Amelink, H.J.C.M. Sterenborg, M.P.L. Bard, S.A. Burgers, "In vivo measurement of the local optical properties of tissue by use of differential path-length spectroscopy", *Optics Letters* **29**, 1087-1089 (2004)
4. Varghese, V. Rajan, T.G. van Leeuwen, W. Steenbergen, "Path length resolved measurements of multiple scattered photons in static and dynamic turbid media using phase modulated low coherence interferometry", *Journal of Biomedical Optics* **12**, 024020 (2007)

5. D.J. Faber, T.G. van Leeuwen, "Are quantitative attenuation measurements of blood by optical coherence tomography feasible?", *Optics Letters* **34**, 1435-1437 (2009)
6. C. Xu, D.L. Marks, M.N. Do, S.A. Boppart, "Separation of absorption and scattering profiles in spectroscopic optical coherence tomography using a least-squares algorithm", *Optics Express* **12**, 4790-4803 (2004)
7. B. Hermann, K. Bizheva, A. Unterhuber, B. Povazay, H. Sattman, L. Schmetterer, A.F. Fercher, W. Drexler, "Precision of extracting absorption profiles from weakly scattering media with spectroscopic time-domain optical coherence tomography", *Optics Express* **12**, 1677-1688 (2004)
8. A. Dubois, J. Moreau, C. Boccara, "Spectroscopic ultrahigh-resolution full-field optical coherence microscopy", *Optics Express* **16**, 17082-17091 (2008)
9. D.T. Delpy, M. Cope, P. van der Zee, S. Arridge, S. Wray, J. Wyatt, "Estimation of optical pathlength through tissue from direct time of flight measurement", *Physics in Medicine and Biology* **33**, 1433-1442 (1988)
10. T.H. Pham, O. Coquoz, J.B. Fishkin, E. Anderson, B.J. Tromberg, "Broad bandwidth frequency domain instrument for quantitative tissue optical spectroscopy", *Review of Scientific Instruments* **71**, 2500-2513 (2000)
11. J.A. Izatt, M.A. Choma, "Theory of Optical Coherence Tomography", Chapter 2 in *Optical Coherence Tomography – Technology and Applications*, W. Drexler, J.G. Fujimoto, Eds., pp. 47-72 (Springer-Verlag, 2008)
12. J.M. Schmitt, A. Knüttel, R.F. Bonner, "Measurement of optical properties of biological tissues by low-coherence reflectometry", *Appl. Opt.* **32**, 6032-6042 (1993)
13. D.A. Boas, K.K. Bizheva, A.M. Siegel, "Using dynamic low-coherence interferometry to image Brownian motion within highly scattering media", *Optics Letters* **5**, 319-321 (1998)
14. A.J. Welch, M.J.C. van Gemert, "Optical-thermal response of laser-irradiated tissue" (Plenum Press, 1995)
15. A.L. Petoukhova, W. Steenbergen, T.G. van Leeuwen, F.F.M. de Mul, "Effects of absorption on coherence domain path length resolved dynamic light scattering in the diffuse regime", *Applied Physics Letters* **81**, 595-597 (2002)
16. C.K. Hitzengerger, A. Baumgartner, W. Drexler, A.F. Fercher, "Dispersion effects in partial coherence interferometry: implications for intraocular ranging", *Journal of Biomedical Optics*, **4**, 144-151 (1999)
17. M. Daimon, A. Masumura, "Measurement of the refractive index of distilled water from the near-infrared region to the ultraviolet region", *Applied Optics* **46**, 3811-3820 (2007)
18. B.E.A. Saleh, M.C. Teich, "Fiber Optics", Chapter 8 in *Fundamentals of Photonics*, pp. 272-309 (Wiley-Interscience, 1991)

CHAPTER 5

Measurements of wavelength dependent scattering and backscattering coefficients by low-coherence spectroscopy

Quantitative measurements of scattering properties are invaluable for optical techniques in medicine. However, non-invasive, quantitative measurements of scattering properties over a large wavelength range remain challenging.

We introduce low-coherence spectroscopy (LCS) as a non-invasive method to locally and simultaneously measure scattering μ_s and backscattering μ_b coefficients from 480 to 700 nm with 8 nm spectral resolution. The method is tested on media with varying scattering properties ($\mu_s = 0.15\text{-}34 \text{ mm}^{-1}$ and $\mu_b = 2.10^{-6}\text{-}2.10^{-3} \text{ mm}^{-1}$), containing different sized polystyrene spheres. The results are in excellent agreement with Mie theory.

Part of this work has been published in: N. Bosschaart, D.J. Faber, T.G. van Leeuwen and M.C.G. Aalders, "Measurements of wavelength dependent scattering and backscattering coefficients by low-coherence spectroscopy", *Journal of Biomedical Optics* 16(3), 030503 (2011)

5.1 Introduction

Quantitative determination of the optical properties of tissue is invaluable in biomedical optics. The majority of optical diagnostic techniques rely on the spectral absorption and scattering properties of tissue, which provide information on its composition and structure. The same optical properties are of essential importance for the development and optimization of optical therapeutic techniques. However, despite the existence of many spectroscopic methods it is still a challenge to do non-invasive, quantitative measurements of the absorption and scattering properties *in vivo* over a large wavelength range.

In Chapter 4, we introduced low-coherence spectroscopy (LCS) to do quantitative and localized measurements of absorption coefficients μ_a over a wavelength range of 480-700 nm with a spectral resolution of 8 nm [1] (all wavelength dependent parameters in this Chapter will be denoted by a boldfaced character). In this Chapter, we use LCS to quantitatively and simultaneously measure scattering μ_s and backscattering μ_b coefficients on a wide range of scattering media ($\mu_s = 0.15\text{-}34 \text{ mm}^{-1}$ and $\mu_b = 2.10^{-6}\text{-}2.10^{-3} \text{ mm}^{-1}$). Thereby, we demonstrate new opportunities for non-invasive scattering property measurements. *In vivo* measurements of the quantitative value of μ_s and μ_b can assist in differentiating between tissue types [2] and modeling of light-tissue interactions. The spectrally resolved information of μ_s and μ_b gives additional valuable information: e.g. the power dependency of μ_s on wavelength and wavelength dependent oscillations in μ_b , which have shown to be related to tissue morphology [3,4].

Whereas extensive research on tissue (back)scattering has been performed in the areas of light scattering spectroscopy (LSS) [3] and angle-resolved low-coherence interferometry [4], these studies lack quantification of μ_s and μ_b , since their primary aim has been to retrieve the size of the scattering particles. Quantification of μ_s and μ_b has been shown in optical coherence tomography studies [2,5], but these studies were limited to the measurement of μ_s and μ_b averaged over the bandwidth of the spectrum, i.e. no spectral information was obtained. Moreover, in these studies quantitative agreement with theory is rarely obtained for highly scattering media, due to multiple scattering contributions to the signal [5]. Other (diffuse) reflectance spectroscopy techniques are able to measure μ_b and the reduced scattering coefficient μ_s' [7], but this requires additional information on the scattering anisotropy g to obtain μ_s . Thus, compared to the existing methods for scattering property measurements, LCS offers the unique possibility for a combination of simultaneous, quantitative and spectrally resolved measurement of μ_s and μ_b . These measurements will therefore assist in more complete, and likely more accurate, characterization of the tissue of interest.

Since LCS is a low coherence interferometry technique, another advantage of LCS is the possibility to measure in a controlled and confined volume [2,5,6], which is important when measuring local optical properties in often inhomogeneous tissue. In addition, knowledge of the contribution of scattering to the measured μ_t is crucial for accurate μ_a determination, because LCS determines the μ_a from the total attenuation coefficient μ_t of the sample. Therefore, this Chapter also provides a more thorough understanding of this contribution.

5.2 Materials and methods

5.2.1 System and acquisition

Using LCS, we measured μ_b and μ_s of aqueous non-absorbing suspensions of different sized polystyrene spheres and validated our results with Mie theory. Therefore, we measured back scattered power spectra $\mathbf{S}(\ell)$ at controlled geometrical path lengths ℓ of the light in a sample. Our LCS system, which is described in detail in Chapter 4 [1], consists of a Michelson interferometer and is optimized for 480–700 nm. The geometrical roundtrip path length ℓ ($\ell=0$ –2 mm, with $\ell=0$ the sample surface) is controlled by translating the reference mirror, in steps of 27 μm . By translating the sample, focus tracking of the 64 μm^2 spot size (see Section 5.2.3) in the sample is achieved. Around ℓ , the signal is modulated by scanning the piezo-driven reference mirror (23 Hz) resulting in a scanning window of $\Delta\ell \approx 44 \mu\text{m}$ and an axial resolution for $\mathbf{S}(\ell)$ of $\frac{1}{2}\Delta\ell \approx 22 \mu\text{m}$. The optical power at the sample is 6 mW. A multimode fiber ($\phi=62.5 \mu\text{m}$) guides the reflected light from both arms to a photodiode.

5.2.2 Determination of μ_s and μ_b

Signal processing after acquisition, which is described in detail in Chapter 4 [1], results in averaged power spectra $\mathbf{S}(\ell)$ with 8 nm resolution (~ 500 averages per ℓ , to avoid any speckle influences, i.e. spectral modulations on $\mathbf{S}(\ell)$ caused by interference between scattering particles). We describe $\mathbf{S}(\ell)$ with a single exponential decay model [2]:

$$\mathbf{S}(\ell) = \mathbf{S}_0 \cdot \mathbf{T}_c \cdot \Delta\ell \cdot \mu_{b,NA} \cdot e^{-\mu_t \cdot \ell} \quad (5.1)$$

where \mathbf{S}_0 is the source power spectrum and \mathbf{T}_c the system coupling efficiency. When $\mathbf{S}(\ell)$ is dominated by single backscattered light, μ_t is the attenuation coefficient of the sample and μ_t equals μ_s for non-absorbing samples (this Chapter). The system dependent parameters will be denoted by $\zeta = \mathbf{S}_0 \cdot \mathbf{T}_c \cdot \Delta\ell$. The spectra $\mathbf{S}(\ell)$ are collected over the detection numerical aperture (**NA**) of the system, therefore we define the measured backscattering coefficient $\mu_{b,NA}$ as the product of μ_s and the phase function $\mathbf{p}(\theta)$, integrated over the solid angle of the **NA** in the medium (Section 5.2.3):

$$\mu_{b,NA} = \mu_s \cdot 2\pi \int_{\theta=\pi-NA}^{\pi} \mathbf{p}(\theta) \cdot \sin(\theta) \cdot d\theta \quad (5.2)$$

The terms $\zeta \cdot \mu_{b,NA}$ and μ_s in the single exponential decay model are obtained by fitting a two-parameter (amplitude and decay, respectively) exponential function to $\mathbf{S}(\ell)$ vs. ℓ . Uncertainties are estimated by the 95% confidence intervals (c.i.) of the fitted parameters [1]. The model is fitted to the measured $\mathbf{S}(\ell)$ starting at $\ell = 50 \mu\text{m}$, up to a path length in the sample of five times the mean free path ($5/\mu_s$ from Mie theory at 480 nm, varying from 100–1950 μm). Prior to fitting the model to $\mathbf{S}(\ell)$, a noise level is subtracted from $\mathbf{S}(\ell)$, which is the sum of the DC spectra of the sample and reference arm.

Knowledge of ζ is required to calculate $\mu_{b,NA}$ from the fitted amplitude $\zeta \cdot \mu_{b,NA}$. Hereto, ζ is determined in a separate calibration measurement in which $\mu_{b,NA}$ is exactly

known from Mie theory and Eq. 5.2. To this end we used NIST-certified polystyrene spheres of $\phi=409\pm 9$ nm (diameter \pm SD, Thermo Scientific, USA). The obtained ζ was used to determine the $\mu_{b,NA}$ in subsequent measurements.

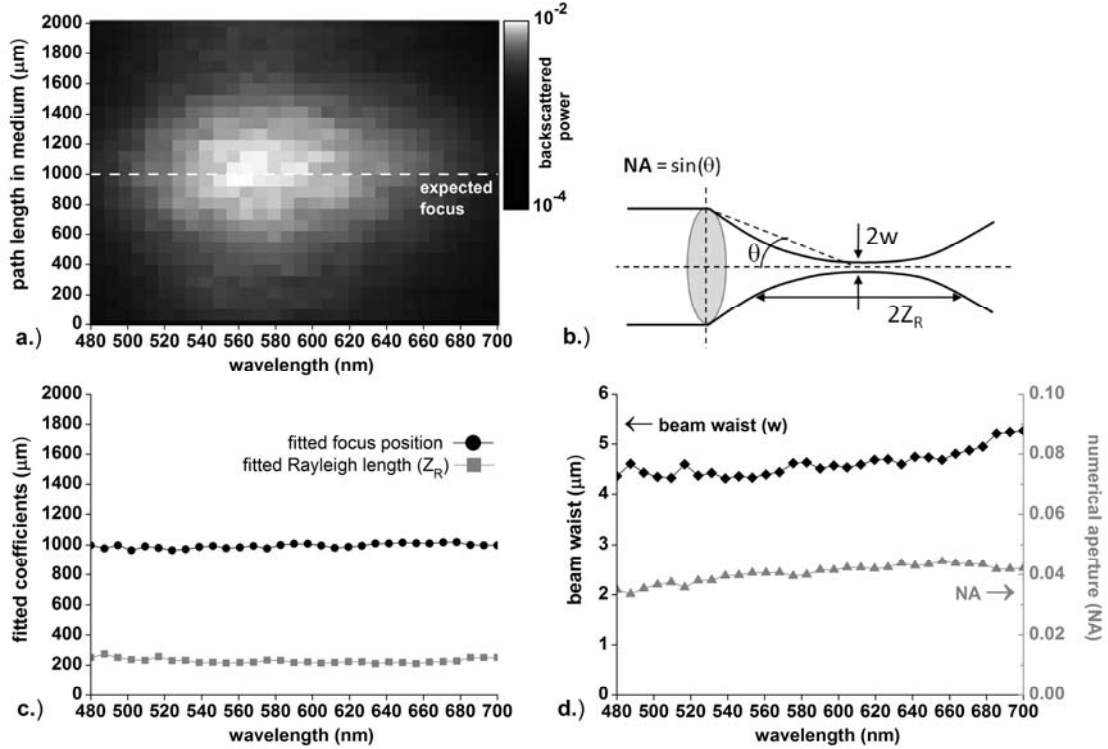


Figure 5.1 a.) point spread function measurement (PSF) on a weakly scattering sample of $\phi 198$ spheres (0.038 volume%), b.) schematic illustration of focus geometry, c.) fitted focus position (ℓ_F) and Rayleigh length (Z_R) on the measured PSF, d.) calculated beam waist (w) and numerical aperture (NA). The parameters Z_R , w and NA are defined within the medium ($n=1.35$).

5.2.3 Point spread function

In order to determine the NA of our system, we measured the wavelength dependent point spread function (PSF) of our system in a weakly scattering medium (0.038 volume% of $\phi 198$ polystyrene spheres, $\mu_s < 1 \text{ mm}^{-1}$) and corrected it for the sample's attenuation (Figure 5.1a). The PSF can be described by a Lorentzian function [6]:

$$\text{PSF}(\ell_F - \ell) = \alpha \cdot \left[\left(\frac{\ell_F - \ell}{2Z_R} \right)^2 + 1 \right]^{-1} \quad (5.3)$$

where α denotes a scaling factor, ℓ_F is the focus position in roundtrip path length units and Z_R is the Rayleigh length of the system (Figure 5.1b). Note that the parameter Z_R is defined within the medium ($n_g=1.35$); in air the Rayleigh length is a factor $2n_g$ lower [6].

Fitting this function to the measured PSF results in wavelength dependent values for ℓ_F and Z_R (Figure 5.1c). The fitted ℓ_F agrees well with the expected focus position at $\ell=1000 \mu\text{m}$. The fitted Z_R can be used to calculate the beam waist, $w = (Z_R\lambda/2\pi)^{1/2}$, and from that the **NA** can be derived, using $\text{NA} = \sin(\theta) \approx \sin(\lambda/(\pi w))$. Figure 5.1d shows that the beam waist is approximately $4.5 \mu\text{m}$ and the **NA** ranges from 0.035 to 0.045 within the investigated spectral range.

Table 5.1 Overview of sphere concentrations (volume %) in the investigated samples

sphere size (diameter \pm SD)	monodisperse samples low μ_s (Fig. 5.2)	monodisperse samples μ_s -range (Fig. 5.3 & 5.4)	polydisperse sample (Fig. 5.6)
198 \pm 5 nm	-	0.038% to 0.950%	-
409 \pm 9 nm	0.071%	0.071% to 0.950%	0.024% &
602 \pm 6 nm	0.048%	0.048% to 0.036%	0.033%
799 \pm 9 nm	0.038%	0.038% to 0.285%	-
1004 \pm 10 nm	0.033%	0.033% to 0.248%	-

5.2.4 Samples and Mie calculations

We prepared a set of four weakly scattering samples, consisting of aqueous suspensions of different sized NIST-certified polystyrene spheres (Thermo Scientific, USA), as indicated in Table 5.1. The sphere concentrations, indicated in volume percentages, were chosen such that μ_s was approximately equal for all samples ($\sim 1.5 \text{ mm}^{-1}$ at 600 nm). The sphere sizes (\varnothing 409 to 1004 nm) lie within the range of scatterer sizes in biological cells [3]. Calibration of ζ was performed with the 0.071% \varnothing 409 nm sample for all sphere sizes and concentrations and a reference measurement on water was obtained to verify the correctness of this calibration.

To test the range of validity of the single exponential decay model for determining μ_s and $\mu_{b,NA}$, it is important to validate the model also for media with higher scattering densities. Therefore, we increased the particle concentration several times for all sphere sizes and included \varnothing 198 nm spheres (Table 5.1).

The wavelength dependent oscillations in the $\mu_{b,NA}$ make it possible to derive particle size [3,4,7] and, because of the quantification of $\mu_{b,NA}$ for these LCS measurements, also concentration from a sample for which these properties are unknown. We tested this hypothesis by measuring μ_s and $\mu_{b,NA}$ from a polydisperse sample containing both 409 nm and 602 nm spheres (Table 5.1). To the measured $\mu_{b,NA}$, we performed a multicomponent, linear least-squares fit of the Mie-calculated $\mu_{b,NA}$ of six different sphere sizes (\varnothing 99, 198, 409, 602, 799 and 1004 nm) to obtain the individual contribution of all spheres on the measured $\mu_{b,NA}$.

In our Mie calculations, we used wavelength dependent refractive indices of water and polystyrene [8] and integrated over the size distribution of the spheres ($2 \cdot \text{SD}$),

given by the manufacturer. Brownian motion of the polystyrene spheres causes Doppler broadening of the measured LCS spectra. For adequate comparison, we convolved the Mie spectra with a Lorentzian, with a line width of 5 to 27 nm, depending on the sphere size-dependent Doppler frequency distribution of the Brownian motion of the spheres, similar to our analysis in Chapter 4 [1].

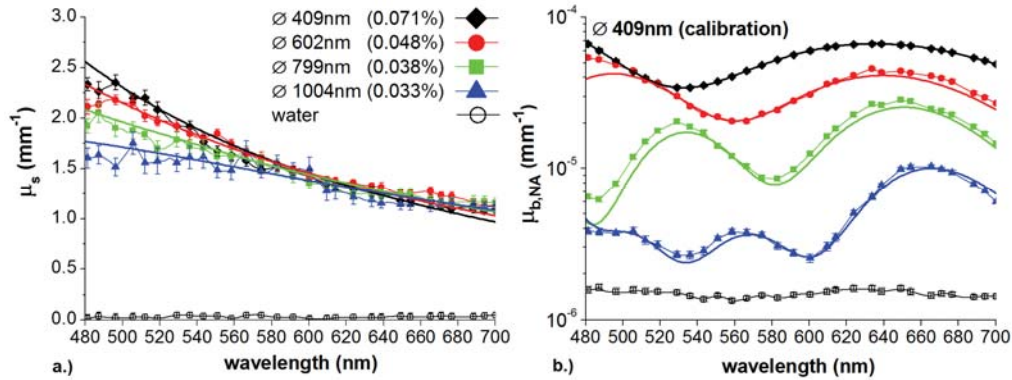


Figure 5.2 LCS (dots) and Mie (thick solid lines) results for (A) scattering coefficients μ_s , and (B) backscattering coefficients $\mu_{b,NA}$ for four aqueous suspensions of different sized polystyrene spheres, and water. Error bars, representing the 95% c.i. of the fitted values, may fall behind data points. The $\mu_{b,NA}$ were calibrated using the 409 nm sample.

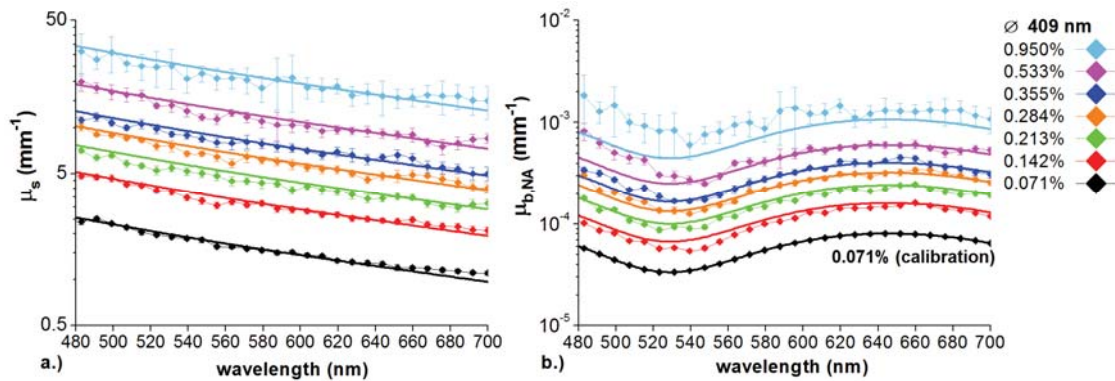


Figure 5.3 LCS (dots) and Mie (thick solid lines) results for a) scattering coefficients μ_s , and b) backscattering coefficients $\mu_{b,NA}$ for six concentrations of 409 nm polystyrene sphere suspensions. Error bars, representing the 95% c.i. of the fitted values, may fall behind data points. The $\mu_{b,NA}$ were calibrated using the 0.071% sample.

5.3 Results and discussion

5.3.1 Weakly scattering monodisperse media

Figure 5.2a shows LCS measurements (dots) of μ_s for the four weakly scattering, monodisperse samples in Table 5.1. The LCS measurements agree within 0.2 mm^{-1} with μ_s from Mie theory (thick solid lines) over the entire wavelength range of 480 – 700 nm. The scattering coefficient has a power dependence on wavelength, with different scatter power for different particle sizes. The attenuation coefficient of water is, as expected, $\sim 0 \text{ mm}^{-1}$ for all investigated wavelengths.

Figure 5.2b shows the LCS measurements (dots) of $\mu_{b,NA}$ on a logarithmic scale for the polystyrene suspensions. The error bars in this graph are in the same order of magnitude as the marker size. The $\mu_{b,NA}$ differ over an order of magnitude between samples, since the phase function changes considerably with sphere size. The measured $\mu_{b,NA}$ are in excellent agreement with Mie theory (thick solid lines), showing the characteristic sphere size dependent oscillations. The $\mu_{b,NA}$ of water shows no pronounced spectral features, which implies that our calibration method of ζ was applied correctly. We attribute the small differences between measurements and Mie calculations to uncertainties in particle size distribution and refractive index that were used as Mie-input (depending on wavelength, a 1% change in the polystyrene refractive index results in a 11-14% change in μ_s and a 11-25% change in $\mu_{b,NA}$).

5.3.2 Concentration ranges of monodisperse media

Figure 5.3 shows the measured μ_s and $\mu_{b,NA}$ for the concentration series of one of the sphere sizes ($\phi 409 \text{ nm}$). The measured μ_s agree with Mie calculations of μ_s within 14%, up to values as high as 34 mm^{-1} , which lies well within the range of tissue scattering (Figure 5.3a). Also the measured $\mu_{b,NA}$ agree well with Mie theory (Figure 5.3b), except for the two highest volume concentrations, where the measurement overestimates $\mu_{b,NA}$ at the shorter wavelengths.

Figure 5.4 shows the measured μ_s and $\mu_{b,NA}$ versus the expected μ_s and $\mu_{b,NA}$ from Mie theory for all sphere sizes at 3 wavelengths within the investigated spectral range: 480, 550 and 700 nm. In general, the measured values agree well with the expected values, but deviations at high concentrations become more apparent for short wavelengths and large sphere sizes. This combination commonly results in an underestimation of μ_s and an overestimation of $\mu_{b,NA}$, which may be explained by the contribution of multiple scattering to the LCS signal. When multiple scattering contributes to the LCS signal, more photons are detected compared to the case of single scattering. As a consequence, the assumption of single scattering in our definition of μ_t in the exponential decay model (Eq. 5.1) is not valid anymore, resulting in the observed overestimation of backscattering ($\mu_{b,NA}$) and an underestimation of attenuation (μ_s). This effect is strongest for large spheres and short wavelengths, since in that case the scattering anisotropy g is largest (Figure 5.5) and hence, multiple scattered photons are more likely to be detected within the **NA** of our LCS system.

The 409 nm concentration series demonstrates that disagreement with the Mie calculated values for the highest volume concentrations is only manifested in $\mu_{b,NA}$ and not in μ_s (i.e. μ_s agrees with the Mie calculated μ_s within the 95% c.i.). For these samples (0.533% and 0.950%), the average surface-to-surface distance between the spheres is

comparable to the wavelength: 760 nm and 556 nm, respectively. Since the effect of multiple scattering would be visible in the measured value of both coefficients, we speculate that another effect may cause this disagreement, i.e. the total scattered field cannot be treated as the superposition of the scattered field by the individual particles (dependent scattering) [9]. Our results indicate that for these sphere concentrations, $\mu_{b,NA}$ is altered to favor more backward than forward directed scattering.

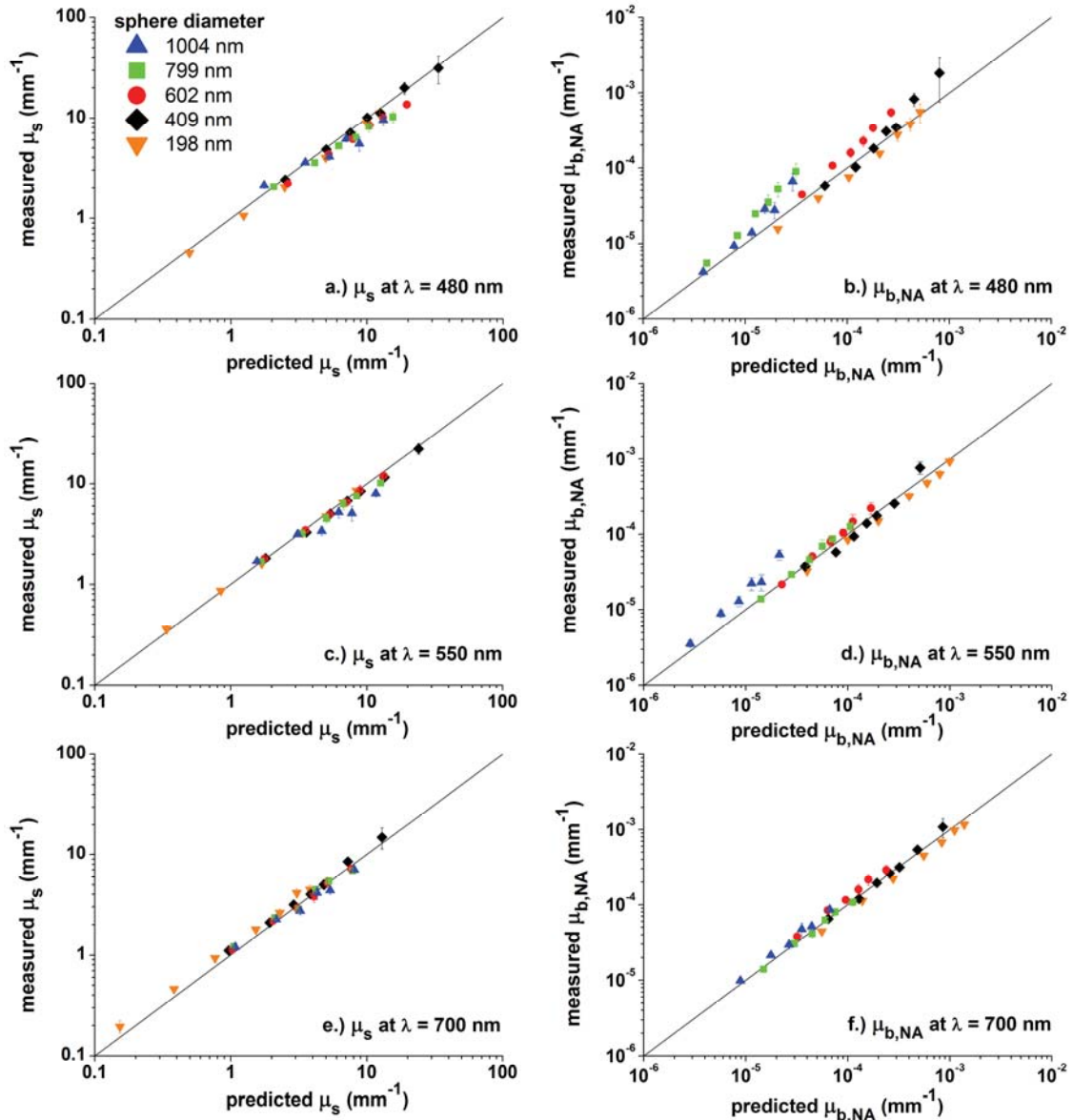


Figure 5.4 Measured (LCS) versus predicted (Mie theory) values of μ_s and $\mu_{b,NA}$ for 5 sphere sizes (198, 409, 602, 799 and 1004 nm) and various concentrations at 3 wavelengths within the investigated spectral range: 480 nm (a and b), 550 nm (c and d) and 700 nm (e and f).

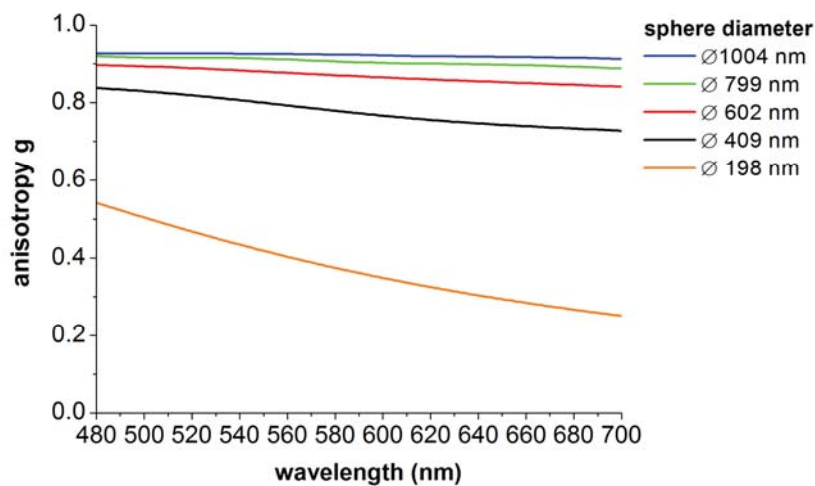


Figure 5.5 Scattering anisotropies g for all sphere sizes, obtained from Mie theory.

5.3.3 Polydisperse sample

Figure 5.6 shows the measured, Mie calculated and fitted $\mu_{b,NA}$ for the polydisperse sample consisting of two sphere sizes. The measured and Mie calculated μ_s are shown in the inset. The multicomponent fit on $\mu_{b,NA}$ gives a good identification of our sample, as shown in Table 5.2.

The fitted concentration of 602 nm spheres exactly matches the expected concentration and the concentration of 409 nm spheres is underestimated with only 8%. Although not present in the sample, small amounts of 99 nm and 1004 nm spheres contribute to the fit. Please note that the relative contribution of these spheres to the $\mu_{b,NA}$ is low (3% and 9%, respectively) compared to the contribution of the 409 nm (37%) and 602 nm (51%) spheres. We attribute the small differences between measurements and Mie calculations to uncertainties in refractive index and particle size distribution that were used as Mie-input.

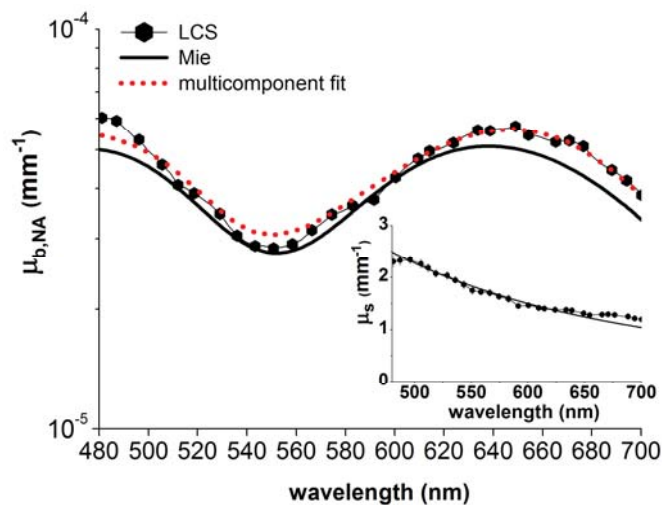


Figure 5.6 LCS and Mie backscattering coefficient spectrum $\mu_{b,NA}$ for a sample containing both 409 nm spheres (0.024%) and 602 nm spheres (0.033%). Dotted red line: multicomponent fit with 6 sphere sizes on the measured $\mu_{b,NA}$. Inset: LCS and Mie scattering coefficient spectra.

Table 5.2 Expected and fitted sphere concentrations

sphere size (diameter \pm SD)	expected concentration (vol%)	fitted concentration (vol%)
99 \pm 5 nm	-	0.002%
198 \pm 5 nm	-	-
409 \pm 9 nm	0.024%	0.022%
602 \pm 6 nm	0.033%	0.033%
799 \pm 9 nm	-	-
1004 \pm 10 nm	-	0.026%

5.4 Conclusion and outlook

The presented results show that LCS enables sample characterization based on absolute values of $\mu_{b,NA}$ and μ_s , the scatter power in μ_s and oscillations in $\mu_{b,NA}$. This very combination of optical properties is characteristic for particle or tissue type [2-7] and therefore offers new opportunities for tissue and/or particle characterization studies. Based on μ_s only, the sphere mix in Figure 5.6 could not have been characterized. In addition, clinical studies have been reported where the measurement of only one parameter was not sufficient to differentiate between tissue types, such as the value of μ_t for measuring (morphological) changes between grades of urothelial carcinoma of the bladder [10]. For these studies, the measurement of both μ_s and $\mu_{b,NA}$ by LCS may assist in better differentiation, because low contrast in μ_s can be accompanied by high contrast in $\mu_{b,NA}$ (Figure 5.1).

In non-absorbing samples, μ_s is extracted directly from the measurement and $\mu_{b,NA}$ requires calibration on a sample with known $\mu_{b,NA}$. To obtain μ_s from tissue, the measured μ_t needs to be corrected for tissue absorption. Several methods to separate μ_s and μ_a from a single attenuation profile have been proposed [11,12]. In addition, the simultaneous measurement of both μ_t and $\mu_{b,NA}$ by LCS may eventually assist in separating scattering and absorption contributions to the LCS signal, since the $\mu_{b,NA}$ is proportional to μ_s but independent of μ_a .

Whereas in this study the scattering properties are measured in non-layered, homogeneous samples, LCS has the potential to measure μ_s and $\mu_{b,NA}$ in individual layers of layered media such as human skin. The controlled path length and the confined measurement volume due to the confocality of the system, in principle allow to measure within a layer of choice, which will be a subject of further study. Even for a confined tissue volume, the $\mu_{b,NA}$ is likely to consist of the contribution of a range of scatterer sizes and it will therefore not exhibit oscillations as clear presented in Figure 5.1, 5.2 and 5.6. Nevertheless, tissue specific spectral features in backscattering have been observed [3,4] and also the absolute value of $\mu_{b,NA}$ contains information on tissue type [2].

Further study is needed to obtain better understanding of the influence of multiple and dependent scattering on the measured μ_s and $\mu_{b,NA}$ for large sphere sizes at high concentrations. Nevertheless, for the smaller sphere sizes (\varnothing 198 and 406 nm), our results are in excellent agreement with Mie theory up to scattering coefficients as high as 34 mm^{-1} .

In conclusion, we present quantitative and wavelength dependent measurements of scattering and backscattering coefficients from polystyrene sphere suspensions. Our method applies for a broad range of sphere sizes and particle densities, and is in good agreement with Mie theory. LCS measures μ_s and μ_b simultaneously, over a large wavelength range and with good spectral resolution. The combined, wavelength dependent information of μ_s and μ_b is likely to assist in more accurate tissue characterization in tissue optics.

References

1. N. Bosschaart, M.C.G. Aalders, D.J. Faber, J.J.A. Weda, M.J.C. van Gemert, T.G. van Leeuwen, "Quantitative measurements of absorption spectra in scattering media by low-coherence spectroscopy", *Opt. Lett.* **34**, 3746-3748 (2009)
2. J.M. Schmitt, A. Knuttel, R.F. Bonner, "Measurement of optical properties of biological tissues by low-coherence reflectometry", *Appl. Opt.* **32**, 6032-6042 (1993)
3. A.H. Hielscher, J.R. Mourant, I.J. Bigio, "Influence of particle size and concentration on the diffuse backscattering of polarized light from tissue phantoms and biological cell suspensions", *Appl. Opt.* **36**, 125-135 (1997)
4. A. Wax, C. Yang, V. Backman, K. Badizadegan, C.W. Boone, R.R. Dasari, M.S. Feld, "Cellular organization and substructure measured using angle-resolved low-coherence interferometry", *Biophys. J.* **82**, 2256-2264 (2002)
5. A.L. Oldenburg, M.N. Hansen, D.A. Zweifel, A. Wei, S.A. Boppart, "Plasmon resonant gold nanorods as low backscattering albedo contrast agents in optical coherence tomography", *Opt. Express* **14**, 6724-6738 (2006)
6. D.J. Faber, F.J. van der Meer, M.C. Aalders, T.G. van Leeuwen, "Quantitative measurement of attenuation coefficients of weakly scattering media using optical coherence tomography", *Opt. Expr.* **12**, 4353-4365 (2004)
7. C. Ungureanu, A. Amelink, R.G. Rayavarapu, H.J.C.M. Sterenborg, S. Manohar, T.G. van Leeuwen, "Differential pathlength spectroscopy for the quantitation of optical properties of gold nanoparticles", *ACS Nano* **4**, 4081-4089 (2010)
8. S.N. Kasarova, N.G. Sultanova, C.D. Ivanov, I.D. Nikolov, "Analysis of the dispersion of optical plastic materials", *Optical Materials* **29**, 1481-1490 (2004)
9. G. Göbel, J. Kuhn, J. Fricke, "Dependent scattering effects in latex-sphere suspensions and scattering powders", *Waves in Random and Complex Media* **5**, 413-426 (1995)
10. E.C.C. Cauberg, D.M. de Bruin, D.J. Faber, T.M. de Reijke, M. Visser, J.J.M.C.H. de la Rosette, T.G. van Leeuwen, "Quantitative measurement of attenuation coefficients of bladder biopsies using optical coherence tomography for grading urothelial carcinoma of the bladder", *JBO* **15**, 066013 (2010)
11. F.E. Robles, A. Wax, "Separating the scattering and absorption coefficients using the real and imaginary parts of the refractive index with low-coherence interferometry", *Opt. Lett.* **35**, 2843-2845 (2010)
12. C. Xu, D.L. Marks, M.N. Do, S.A. Boppart, "Separation of absorption and scattering profiles in spectroscopic optical coherence tomography using a least-squares algorithm", *Opt. Express* **12**, 4790-4803 (2004)

CHAPTER 6

In vivo low-coherence spectroscopic measurements of local hemoglobin absorption spectra in human skin

Localized spectroscopic measurements of optical properties are invaluable for diagnostic applications that involve layered tissue structures, but conventional spectroscopic techniques lack exact control over the size and depth of the probed tissue volume. We show that low-coherence spectroscopy (LCS) overcomes these limitations by measuring local attenuation, and absorption coefficient spectra in layered phantoms. In addition, we demonstrate the first *in vivo* LCS measurements of the human epidermis and dermis only. From the measured absorption in two distinct regions of the dermal microcirculation, we determine total hemoglobin concentration (3.0 ± 0.5 g/L and 7.8 ± 1.2 g/L) and oxygen saturation.

This work has been published in: N. Bosschaart, D.J. Faber, T.G. van Leeuwen and M.C.G. Aalders, "*In vivo* low-coherence spectroscopic measurements of local hemoglobin absorption spectra in human skin", *Journal of Biomedical Optics* 16(10), 100504 (2011)

6.1 Introduction

The derivation of physiological parameters from the spectroscopic determination of tissue optical properties can offer a fast and painless alternative to invasive diagnostic procedures such as tissue biopsies and drawing of blood. For instance, the absorption coefficient of the dermal microcirculation is directly related to the tissue hemoglobin concentration, which provides information on oxygen saturation, blood volume and potentially the hemoglobin concentration in whole blood. A variety of spectroscopic techniques is available for measuring tissue optical properties [1,2]. However, these techniques have limited ability to confine their probing volume to embedded structures such as the dermal microcirculation (which is located beneath the epidermis), or require long photon path lengths (several mm to cm) which exceed the adult dermal thickness of approximately 0.2–1.2 mm [3]. Consequently, many of those techniques rely on assumption-based algorithms to account for layered media [4]. Low-coherence interferometry techniques, such as low-coherence spectroscopy (LCS) [5,6] and spectroscopic optical coherence tomography (sOCT) [7,8] do not suffer from this limitation, since they control the size and position of the probed volume from which the optical properties are determined (lateral and in depth) – i.e. they reject the detection of photons that originate from outside the volume of interest.

In Chapters 4 and 5 we validated LCS on homogeneous phantoms with controlled optical properties, to quantitatively obtain the attenuation μ_t , absorption μ_a [5], scattering μ_s and backscattering μ_b [6] coefficients between 480–700 nm (bold-faced characters denote wavelength (λ) dependent parameters). In this Chapter we present, for the first time to our knowledge, quantitative measurements of local μ_t and μ_a spectra within selected volumes of inhomogeneous turbid media. The selection of a volume of interest is supported by a high resolution OCT image that is reconstructed from the LCS signal. We validate our method by retrieving the dye concentration from the measured μ_a of an Intralipid-dye phantom ($\mu_s = 4\text{--}6\text{ mm}^{-1}$, $\mu_a = 0\text{--}5\text{ mm}^{-1}$), covered by light attenuating layers with varying optical densities (0.39–0.89). Subsequently, we demonstrate the first *in vivo* LCS measurements of μ_t and μ_a of the human epidermis and dermal microcirculation, from which we determine total hemoglobin concentrations and oxygen saturation.

6.2 Materials and methods

6.2.1 System and acquisition

To obtain the μ_t and μ_a from a target volume, we measured back scattered power spectra $S(\ell)$ at controlled geometrical path lengths ℓ of the light in the medium (path length and depth related parameters in this Chapter are corrected for the group refractive index n_g of the medium). Our LCS system, which is described in detail in Chapter 4 [5], consists of a Michelson interferometer and is optimized for the wavelength range of 480–700 nm. We controlled ℓ by translating the reference mirror in steps of 27 μm . By translating the sample in the axial direction, focus tracking of the spot size ($r = 4.5\text{ }\mu\text{m}$) in the medium is achieved. Around ℓ , the signal is modulated by

scanning the piezo-driven reference mirror (23 Hz), resulting in a scanning window of $\Delta\ell \approx 44 \mu\text{m}$ in the medium. The optical power at the sample is 6 mW.

A multimode fiber ($\phi=62.5 \mu\text{m}$) guides the reflected light from both arms to a photodiode. Fourier transformation of the acquired time signal results in spectra $\mathbf{S}(\ell)$ with spectral resolution $\Delta\lambda = \lambda^2/(n\Delta\ell)$ ($4\text{nm} < \Delta\lambda < 9\text{nm}$) [5]. To minimize the influence of speckle noise on $\mathbf{S}(\ell)$, we spatially average $\mathbf{S}(\ell)$ (90-250 spectra) by translating the sample and measuring $\mathbf{S}(\ell)$ at every $5 \mu\text{m}$. Fitting the single exponential decay model $\mathbf{S}(\ell) = \alpha \cdot \exp(-\mu_t \cdot \ell)$ (free running fit parameters α and μ_t) to the background corrected $\mathbf{S}(\ell)$ vs. ℓ , results in a μ_t spectrum [6]. Uncertainties in α and μ_t are estimated by their 95% confidence intervals (c.i.).

6.2.2 Separation of μ_s and μ_a

When $\mathbf{S}(\ell)$ is dominated by single backscattered light, the attenuation coefficient $\mu_t = \mu_s + \mu_a$. Since the dependence of μ_s on wavelength can be described by $a \cdot \lambda^{-b}$, least-squares fitting of $\mu_t = a \cdot \lambda^{-b} + \sum_i (c_i \cdot \mu_{a,i})$ to the wavelength dependent μ_t -measurement results in the individual contributions of μ_s and μ_a to the measured μ_t . The free running fit parameters a , b and c_i are constraint to positive values. The wavelength dependent $\mu_{a,i}$ are the known absorption spectra (unit: mm^{-1} per unit concentration) of the contributing chromophores i with contribution c_i , which are the μ_a of the dye for the phantom measurements and the μ_a of deoxygenized hemoglobin (Hb) and oxygenized hemoglobin (HbO₂) for the *in vivo* skin measurements [9]. The μ_a of the dye was obtained from a transmission measurement as described in Chapter 4 [5]. Since we are primarily interested in the total hemoglobin concentration ($[\text{tHb}] = c_{\text{HbO}_2} + c_{\text{Hb}}$) and the oxygen saturation ($\text{SO}_2 = c_{\text{HbO}_2}/[\text{tHb}]$) with their uncertainty estimates ($\pm 95\%$ c.i.) for the *in vivo* measurements, we directly fit the $[\text{tHb}]$ and the SO_2 by substituting $c_{\text{HbO}_2} = \text{SO}_2 \cdot [\text{tHb}]$ and $c_{\text{Hb}} = (1 - \text{SO}_2) \cdot [\text{tHb}]$ in the fitting algorithm.

6.2.3 OCT image reconstruction

The volume from which we obtain μ_t is controllable in both size and position inside the medium, by choosing the region for lateral averaging and the ℓ -interval for fitting the exponential decay model. When measuring on inhomogeneous media such as skin, spatial information is needed to confine our region of interest to e.g. the epidermal or dermal layer. Therefore, we support our analysis by reconstructing an OCT image from the individual LCS time signals ($i_{\text{AC}}(t)$) within every $\Delta\ell$ in the axial and lateral direction, using depth scaling $d = \ell/2$. The axial resolution of these ‘fused’ OCT images is given by the coherence length of the light source of $\sim 1.5 \mu\text{m}$ and is therefore higher than the axial resolution of $22 \mu\text{m}$ for $\mathbf{S}(\ell)$.

6.2.4 Layered phantoms and *in vivo* skin measurement

We measured μ_t on a medium consisting of 1% Intralipid (Intralipid®20%, Fresenius Kabi, Germany) and 10% magenta dye (Ecoline #337, Royal Talens, The Netherlands), uncovered and covered by non-absorbing silicone-titanium dioxide (TiO₂) layers [10]. The three covering layers varied in thickness D and scattering, resulting in optical densities ($\text{OD} = D \cdot \mu_t$) of 0.39–0.89 (Table 6.1). The measurement volume ($1250 \times 484 \mu\text{m}^2$, width \times depth) from which we acquired μ_t was confined to the Intralipid-dye medium, directly behind the layer-medium interface.

For the *in vivo* measurement, we measured the skin of a healthy human volunteer on the palmar side of a stretched finger joint. $S(\ell)$ was acquired over a skin volume of $2000 \times 800 \mu\text{m}^2$ (width x depth). During the measurement, the finger joint was stabilized with light pressure against a glass slide. Index-matching gel (Euroband Pedicat, Pollak, France) was applied at the glass-tissue interface to minimize specular reflections.

Table 6.1 Phantom layer properties and fitted coefficients on the Intralipid-dye medium behind each layer

	D (μm)	μ_t (mm^{-1})	OD ([])	fitted b ([])	fitted dye concentration (%)
no layer	-	-	-	1.8 ± 0.1	$10.2 \pm 0.5\%$
layer 1	155	2.5	0.39	1.8 ± 0.2	$9.3 \pm 0.7\%$
layer 2	170	5	0.85	1.6 ± 0.2	$9.2 \pm 0.9\%$
layer 3	355	2.5	0.89	1.1 ± 0.3	$9.3 \pm 0.6\%$

6.3 Results and discussion

6.3.1 Layered phantoms

Figure 6.1 shows the measured μ_t (dots) on the Intralipid-dye medium, uncovered and covered by the three layers with varying OD. The μ_t agree within $\sim 10\%$ of the measured values, indicating that the measurement of μ_t is unaffected by the optical density of the layer covering the medium. Also the fits on μ_t (solid lines) and the μ_s -contribution to the fits (dotted lines) are minimally affected by the covering layers. We chose not to separately show the μ_a -contribution to the fits, since this contribution is visible in Figure 6.1 as the difference between the fits on μ_t and their μ_s -contribution. Fitted scatter powers b on the μ_t of the Intralipid-dye medium ranged from 1.1 ± 0.3 to 1.8 ± 0.2 (Table 6.1). The fitted dye concentration ranged between $9.2 \pm 0.9\%$ and $10.2 \pm 0.5\%$, resulting in a maximum deviation of 0.8% from the expected dye concentration of 10%.

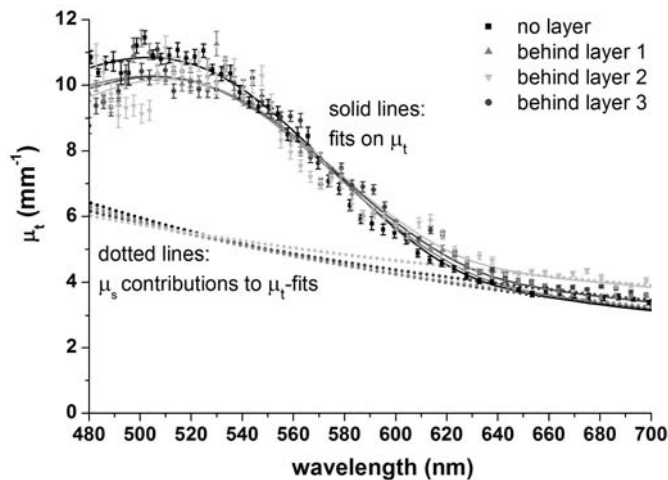


Figure 6.1 Measured μ_t (dots) of a 1% Intralipid-10% dye phantom behind no layer and three TiO_2 -silicone layers with varying OD (Table 6.1). Fits on μ_t and μ_s -contributions to the μ_t -fits are shown for all measurements.

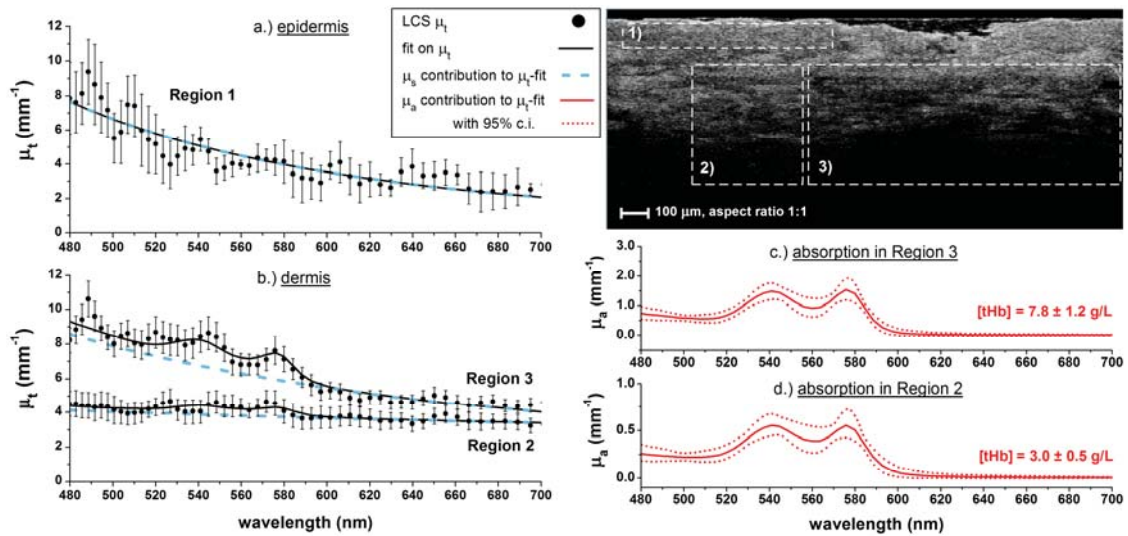


Figure 6.2 *In vivo* measurement on the skin of the palmar side of a finger joint. The measured μ_t fits on μ_t and μ_s -contributions to the μ_t -fits are shown in a.) for the epidermis (Region 1) and b.) for the dermis (Regions 2 and 3). The μ_a -contributions to the μ_t -fits are shown in c.) for Region 3 and d.) Region 2 (note the difference in vertical axis scaling). The selected regions are shown in the OCT image in the upper right corner.

6.3.2 In vivo skin measurement

The upper right corner of Figure 6.2 shows the OCT image that was reconstructed from the *in vivo* measurement on the skin of the palmar side of a stretched finger joint. Using the structural information from the image, we selected regions in the presumed epidermis (Region 1: $715 \times 88 \mu\text{m}^2$) and dermis (Region 2: $440 \times 418 \mu\text{m}^2$, Region 3: $1080 \times 418 \mu\text{m}^2$) for obtaining μ_t . The fit on the measured μ_t of the epidermis (Figure 6.2a) only shows the contribution of scattering ($b=3.5 \pm 0.3$) and neglects the absorption of hemoglobin ($[\text{tHb}] = 0 \text{ g/L}$), which agrees with the expected absence of blood vessels in this skin layer.

Within the dermis, we can distinguish two regions with relatively high (Region 2) and low (Region 3) homogeneity. The measured μ_t differ considerably between the two regions (Figure 6.2b), which can be ascribed to a difference in both scatter power ($b=0.5 \pm 0.1$ in Region 2, $b=2.0 \pm 0.1$ in Region 3) and absorption. The μ_a -spectra of both regions (i.e. the μ_a -contribution to the μ_t -fits) are shown Figure 6.2c and 6.2d. The fitted $[\text{tHb}]$ of $3.0 \pm 0.5 \text{ g/L}$ in Region 2 and $7.8 \pm 1.2 \text{ g/L}$ in Region 3 indicate the presence of blood and can be related to normal dermal blood volume fractions of 2% and 5% respectively, when assuming a fixed hemoglobin concentration of 150 g/L for whole blood [9]. The fitted SO_2 of $81 \pm 34\%$ in Region 2 and $100 \pm 31\%$ in Region 3 are also within physiological range.

Presumably, Region 3 encloses a flexure line and Region 2 encloses surrounding skin, since relative differences in hemoglobin absorption up to 63% were found between those two palmar skin regions during stretching [3], which is consistent with our $[\text{tHb}]$ results. This also explains the difference in scattering between the two regions, because tissue homogeneity and organization of collagen fiber content, the

major contributor to dermal scattering, differ significantly between these skin regions [3]. The value of the μ_s -contributions to the measured μ_t fall within the physiological range of 1-100 mm^{-1} [1], but the actual dermal μ_s may be underestimated due to the contribution of multiple scattering to the LCS signal [6]. Nevertheless, since absorption takes place along the controlled photon path, this contribution does not influence the determination of μ_a [5].

6.4 Conclusion and outlook

These *in vivo* measurements show that LCS can be used to measure hemoglobin concentration and oxygenation in the microcirculation. Although no gold standard exists to confirm our *in vivo* [tHb] and SO_2 determinations, their values are convincing biologically and the optical properties from which they were derived are within the range of optical properties that were validated in our phantom study. The accuracies at which we determined [tHb] ($\sim 15\%$) and SO_2 ($\sim 30\%$) are influenced by the homogeneity of their distribution within the investigated region, and by the accuracy of the determination of μ_t . The latter is affected by the size of the investigated region (i.e. the number of spatial averages and the length of the ℓ -interval for fitting the exponential decay model) and the **OD** of the medium covering this region, which limits the maximum probing depth of LCS to $\sim 0.5\text{--}1$ mm *in vivo*. The limiting accuracy of the *in vivo* determination of [tHb] can be expected to be 8%, because this was found to be the minimum accuracy for the determination of the dye concentration in the homogeneous Intralipid-dye layer of the phantoms. Since the epidermal **OD** (~ 0.8) is comparable to the **OD**'s of the layers in our phantom study, the extra inaccuracy of the [tHb] and SO_2 determination can be ascribed to the skin's heterogeneity [3]. Although the size of the investigated region improves accuracy, it negatively affects measurement speed. Faster acquisition can be achieved by optimizing this trade-off, and by investigating the possibility for Fourier domain acquisition. In contrast to time domain acquisition, the latter will require correction for unwanted signal attenuation due to out-of-focus detection and sensitivity roll-off in depth [8,11].

Potentially, the dermal [tHb] can be related to the hemoglobin concentration in whole blood, if the blood volume within the investigated region can be assessed. A possible method that deserves further investigation for this purpose is obtaining the blood volume from the OCT image by assessing the vessel density using advanced signal analysis, for instance as described in [12]. When measuring on other tissue types, the contribution of additional chromophores (e.g. bilirubin, melanin) to the measured μ_t may need to be incorporated in our algorithm for fitting μ_t . Also correction for Doppler broadening or shifting of the measured μ_t spectra may be needed for tissues that exhibit blood flow. We did not observe any of those influences on the measured μ_t spectra in Figure 6.2b, which can be explained by a temporary decrease of blood flow due to applied pressure on the skin.

In conclusion, we have shown that we can use LCS to locally obtain absorption coefficient spectra within confined volumes of optically inhomogeneous media. This enabled us to perform the first *in vivo* LCS measurements of hemoglobin concentration and oxygen saturation inside the dermal microcirculation. By confining the

measurement volume to specific tissue structures, LCS overcomes the limitations of conventional spectroscopic techniques. LCS therefore offers a potential alternative to invasive drawing of blood for the determination of whole blood hemoglobin concentration and oxygen saturation.

References

1. R. Richards-Kortum, E. Sevick-Muraca, "Quantitative optical spectroscopy for tissue diagnosis", *Annual Review of Physical Chemistry* **47**, 555-606 (1996)
2. R.L.P. van Veen, A. Amelink, M. Menke-Puymers, C. van der Pol, H.J.C.M. Sterenberg, "Optical biopsy of breast tissue using differential path-length spectroscopy", *Physics in Medicine and Biology* **50**, 2573-2581 (2005)
3. T.C. Wright, E. Green, J.B. Phillips, O. Kostyuk, R.A. Brown, "Characterization of a 'blanch-blush' mechano-response in palmar skin", *Journal of Investigative Dermatology* **126**, 220-226 (2006)
4. A. Kienle, M.S. Patterson, N. Dognitz, R. Bays, G. Wagnieres, H. van den Bergh, "Noninvasive determination of the optical properties of two-layered turbid media", *Applied Optics* **37**(4), 779-791 (1998)
5. N. Bosschaart, M.C.G. Aalders, D.J. Faber, J.J.A. Weda, M.J.C. van Gemert, T.G. van Leeuwen, "Quantitative measurements of absorption spectra in scattering media by low-coherence spectroscopy", *Optics Letters* **34**, 3746-3748 (2009)
6. N. Bosschaart, D.J. Faber, T.G. van Leeuwen, M.C.G. Aalders, "Measurements of wavelength dependent scattering and backscattering coefficients by low-coherence spectroscopy", *JBO* **16**, 030503 (2011)
7. D.J. Faber, E.G. Mik, M.C.G. Aalders, T.G. van Leeuwen, "Toward assessment of blood oxygen saturation by spectroscopic optical coherence tomography", *Optics Letters* **30**, 1015-1017 (2005)
8. F.E. Robles, S. Chowdhury, A. Wax, "Assessing hemoglobin concentration using spectroscopic optical coherence tomography for feasibility of tissue diagnostics", *Biomedical Optics Express* **1**, 310-317 (2010)
9. Data tabulated from various sources compiled by S. Prahl, <http://omlc.ogi.edu/spectra>
10. D.M. de Bruin, R.H. Bremmer, V.M. Kodach, R. de Kinkelder, J. van Marle, T.G. van Leeuwen, D.J. Faber, "Optical phantoms of varying geometry based on thin building blocks with controlled optical properties", *JBO* **15**, 025001 (2010)
11. F. Robles, R.N. Graf, A. Wax, "Dual window method for processing spectroscopic optical coherence tomography signals with simultaneously high spectral and temporal resolution", *Optics Express* **17**, 6799-6812 (2009)
12. L. An, J. Qin and R.K. Wang, "Ultrahigh sensitive optical microangiography for *in vivo* imaging of microcirculations within human skin tissue beds", *Optics Express* **18**, 8220-8228 (2010)

CHAPTER 7

Improved acquisition speed in low-coherence spectroscopy by means of spectroscopic detection

Low-coherence spectroscopy (LCS) is a promising technique for the non-invasive determination of blood composition, but its clinical utility may be limited by the speed of the current time domain detection scheme. In this Chapter, we investigate the possibility of spectroscopic detection in LCS (sdLCS), which has a theoretical sensitivity and/or speed advantage compared to time domain detection (tdLCS).

Since sdLCS requires the acquisition of spectra with both high spectral, and high spatial resolution, a new method of acquisition and analysis was developed. In this Chapter, we validate our method computationally in a simulation and experimentally on a phantom with known optical properties. The attenuation, absorption and scattering coefficient spectra from the phantom that were measured by sdLCS agree well with the expected optical properties and are comparable to the measured optical properties by tdLCS.

7.1 Introduction

In the previous Chapters 4 to 6, we have shown that low-coherence spectroscopy (LCS) can be used to measure local absorption, scattering and backscattering coefficient spectra in turbid media over almost the complete visible wavelength range (480 to 700 nm) [1-3]. By deriving hemoglobin concentrations from absorption coefficient spectra in the dermal microcirculation (Chapter 6), we showed that LCS is a promising technique for the localized quantification of tissue chromophore concentrations, which may lead to e.g. a non-invasive alternative for invasive blood sampling [3]. However, since most clinical applications require fast measurements for instantaneous diagnosis and the reduction of motion artifacts, the measurement speed of the current time domain LCS (tdLCS) system may limit its clinical applicability. From optical coherence tomography (OCT) studies, we know that spectroscopic detection allows for more sensitive measurements compared to time domain detection [4,5], which can be exchanged for higher acquisition speed at unaltered sensitivity. Therefore, in this Chapter we investigate the possibility for spectroscopic detection in LCS (sdLCS), focusing primarily on validating a new method of analysis that was developed for this purpose.

Spectroscopic detection in OCT commonly involves spectrographs with high spectral resolution, a narrow wavelength range and a large number of pixels, resulting in large effective imaging depths (i.e. high maximal imaging depth and weak sensitivity roll-off in depth). Consequently, an A-scan of several mm can be recovered from a single back scattered spectrum, which is used for constructing an intensity image with high spatial resolution [4,5]. In LCS, we are mainly interested in the spectral content of the signal within a confined volume and hence, LCS requires both high spatial and sufficient spectral resolution (Chapter 4). In the case of spectroscopic detection, this can be achieved either by signal processing after acquisition [6], or by adjusting the signal acquisition itself. Since the latter has not been investigated before, we developed a new approach for signal acquisition in sdLCS.

Our approach involves step-wise detection of local back scattered spectra with a spectrograph that has an effective imaging depth of only 9 μm in air. Thereby, we achieve both high spatial and sufficient spectral resolution (6 nm) and we maintain the advantage of focus tracking, as we had in our tdLCS system. The main challenge in step-wise spectroscopic detection with limited imaging depth involves removing the mirror image that originates from the complex ambiguity of the LCS signal. Methods for mirror image removal in OCT imaging commonly involve phase modulation and filtering of the modulated signal [8-10]. Similarly, our approach is to modulate the LCS signal, by using an oscillating mirror in the reference arm.

Since the primary aim of this Chapter is to validate whether we can use this new approach for the determination of local absorption and scattering coefficient spectra, we will provide proof of principle with an on-the-shelf spectrograph (USB4000, Ocean Optics, USA). Only part of the feasible speed advantage is demonstrated, since the quantum efficiency and acquisition speed of this spectrograph are not optimized for sdLCS. After describing the theory behind sdLCS, we will validate our algorithm with a simulation of an sdLCS absorption measurement, while simulating the USB4000 as the detecting spectrograph. Subsequently, we experimentally demonstrate the ability of

sdLCS to measure the attenuation, absorption and scattering coefficient spectra from a polystyrene-dye phantom, and we compare our results to a tdLCS measurement.

7.2 Theory

The main difference between sdLCS and tdLCS, is that the detector current i_D is acquired as a function of wavelength λ (e.g. by a spectrograph), instead of time by a photodiode (Chapters 4 to 6). Similar Eq. 4.1 for tdLCS, i_D is modulated by the path length difference between the sample arm and the reference arm $\Delta L = 2(x_S - x_R)$, with sample arm length x_S and reference arm length x_R . Hence, for sdLCS we can write:

$$i_D(k) \propto I_S(k) + I_R(k) + \sqrt{I_S(k) \cdot I_R(k)} \cdot 2\cos(k\Delta L) \quad (7.1)$$

where k is the wavenumber ($k = 2\pi/\lambda$) and I_S and I_R are the signal intensities in the sample and reference arm, respectively. The two left terms of Eq. 7.1 denote the ('DC') non-modulated part of $i_D(k)$ and the right term denotes the ('AC') modulated part of $i_D(k)$, as has been illustrated in Figure 7.1a. Since I_S and I_R both originate from the source spectrum S_0 , the modulation term in Eq. 7.1 can be written in terms of S_0 . In case of a single reflector at path length ℓ (depth $\ell/2$), this results in:

$$i_{D,\text{modulated}}(k) \propto \sqrt{\eta_S \cdot \eta_R} \cdot e^{-\mu_t \ell} \cdot S_0(k) \cdot 2\cos(k\Delta L) \quad (7.2)$$

with η_S and $\eta_R=1-\eta_S$ the fractions of S_0 that are guided towards the sample and reference arm, respectively, as determined by the splitting ratio of the beam splitter. The light originating from the sample arm is backscattered by a sample with an attenuation coefficient μ_t and hence, I_S is attenuated by Beer's law if the geometrical path length ℓ in the sample increases. In sdOCT, an A-scan (i.e. the backscattered intensity as a function of $d = \frac{1}{2}\Delta L$) is obtained by Fourier transformation of $i_D(k)$:

$$i_D(\Delta L) = \left| \mathfrak{F}\{i_D(k)\} \right|^2 \quad (7.3)$$

As illustrated in Figure 7.1b, the horizontal axis of $i_D(\Delta L)$ runs from $-\Delta L_{\text{max}}$ to ΔL_{max} . For every ΔL a 'mirror image' is present at $-\Delta L$, i.e. both these path length differences result in the same modulation frequency on $i_D(k)$ (Eq. 7.1 and 7.2). The Nyquist criterion defines the maximal measurable path length difference ΔL_{max} , or imaging depth $d_{\text{max}} = \frac{1}{2}\Delta L_{\text{max}}$:

$$\Delta L_{\text{max}} = \frac{\pi}{\delta k} \quad (7.4)$$

in which $\delta k = (k_{\text{max}} - k_{\text{min}})/N_p$ depends entirely on the properties of the detecting spectrograph, which are the number of pixels N_p , and the minimal and maximal detectable wave number k_{min} and k_{max} .

The path length range over which $I(\Delta L)$ can be observed not only depends on ΔL_{max} , but also on the sensitivity roll-off with ΔL of the spectrograph, caused by the finite spectrometer resolution [11]:

$$I(\Delta L) = \frac{\sin^2(\pi \Delta L / 2 \Delta L_{\max})}{(\pi \Delta L / 2 \Delta L_{\max})^2} \cdot \exp\left(-\frac{\pi^2 (\Delta k / \delta k)^2 \left(\frac{\Delta L}{\Delta L_{\max}}\right)^2}{8 \ln 2}\right) \quad (7.5)$$

in which Δk is the spectral resolution of the spectrograph.

Since we use sdLCS for doing spectroscopy, we are interested in the spectrum $i_D(k)$ itself, rather than an A-scan as in sdOCT. However, Eq. 7.4 and 7.5 are important for sdLCS, since the ΔL_{\max} and the signal roll-off determine the highest measurable modulation frequency in $i_D(k)$, and therefore the spatial resolution at which the spectrum $i_D(k)$ can be acquired. In contrast to sdOCT, sdLCS requires low values of ΔL_{\max} and a fast sensitivity roll-off to obtain good spatial resolution for $i_D(k)$ (see Section 7.4). Similar to tdLCS, this introduces a trade-off between the spectral and spatial resolution of $i_D(k)$, because a fast sensitivity roll-off is accompanied by a low spectral resolution Δk (Eq. 7.5).

7.2.1 Mirror image removal

Merely acquiring $i_D(k)$ within a confined path length range does not provide us with a spectrum that we can use for the determination of μ_t , since $i_D(k)$ contains unwanted DC (i.e. non-modulated components) and modulation components (Eq. 7.1 and 7.2). Moreover, the mirror image induces cross-talk between $i_D(\Delta L)$ and $i_D(-\Delta L)$ within the investigated path length range. This complex ambiguity can be removed by phase modulation and frequency domain filtering of the signal. Therefore, we modulate $i_D(k)$ using the oscillating mirror in the reference arm of our LCS system, which introduces a Doppler shift f_D to the signal:

$$f_D = \frac{2v_R}{\lambda} = \frac{v_R \cdot k}{\pi} \quad (7.6)$$

with v_R the velocity of the reference mirror. Acquisition of N spectra $i_D(k)$ at every integration time τ of the spectrograph results in a dataset $i_D(k,t)$, as illustrated in Figure 7.1c. The phase of the modulation on $i_D(k,t)$ changes at every τ , because the movement of the reference mirror induces a change in ΔL (vertical direction in Figure 7.1c). Figure 7.1d illustrates the time-modulation on $i_D(k,t)$ by f_D for one wavelength (horizontal direction in Figure 7.1c). Since the sensitivity of the measurement is largest around $\Delta L = 0$ or 'zero delay' (Eq. 7.5), the range of ΔL is chosen such that it crosses zero delay at $\frac{1}{2}N\tau$ (Figure 7.1e). The integration time of the spectrograph should be chosen such that the time-modulation on $i_D(k,t)$ is adequately sampled. Hence the sampling frequency $f_s = 1/\tau$ needs to be larger than $2f_{D,\max}$ (the largest value of f_D within the investigated spectral range). For the integration time, this results in:

$$\tau < \frac{\pi}{2v_R \cdot k_{\max}} = \frac{\lambda_{\min}}{4v_R} \quad (7.7)$$

with k_{\max} the largest wave number and λ_{\min} the shortest wavelength within the investigated spectral range.

Fourier transformation on $i_D(k,t)$ with respect to t provides the frequency content of the signal $i_D(k,f)$, which contains the modulation frequency f_D , its mirror image and a DC component (Figure 7.1f). By filtering out the part of $i_D(k,f)$ containing only the positive

frequencies $+f_D$, the unwanted DC component and the negative frequencies $-f_D$ are lost. Now that $i_D(k)$ is confined both in amplitude and phase, the complex ambiguity and the mirror image in the path length domain (Figure 7.1b) are lost. Inverse Fourier transformation on the filtered $i_D(k,f)$ with respect to f provides a smooth, non-modulated $i_D(k,t)$ (Figure 7.1g), and averaging of $i_D(k,t)$ over time results in the final spectrum \mathbf{S} that we can use for the determination of μ_t (Figure 7.1h).

Similar to tdLCS, a dataset $\mathbf{S}(\ell)$ is generated by step-wise alteration of the depth or geometrical round trip path length ℓ in the sample around which $i_D(k)$ is acquired (Chapter 4). Hence, the advantage of focus tracking that we had in tdLCS can still be applied in sdLCS.

7.2.2 Sensitivity and/or speed advantage

Our method for sdLCS provides a sensitivity advantage over tdLCS, which can be explained in terms of the signal to noise ratio (SNR). The SNR of any shot-noise limited LCS system is given by:

$$\text{SNR} = \frac{\epsilon \cdot \mathbf{S}}{h\nu \cdot \Delta f} \quad (7.8)$$

in which ϵ is the detection efficiency, $h\nu$ the photon energy and Δf the detection bandwidth of the system [5]. Using Eq. 4.8, we can write:

$$\Delta f = 2f_{\text{scan}} d_{\text{scan}} \frac{\Delta\lambda}{\lambda_0^2} \quad (7.9)$$

with f_{scan} the scan rate and d_{scan} the scan length for the acquisition of one spectrum. For tdLCS, $f_{\text{scan}} = 2f_R$ and $d_{\text{scan}} = \Delta R$ (Chapter 4). For sdLCS, $f_{\text{scan}} = 1/\tau$ and $d_{\text{scan}} = 2d_{\text{max}} = \Delta L_{\text{max}} = \lambda^2/(2\delta\lambda)$, if mirror image removal is applied. If we assume that in sdLCS, N_p pixels cover the bandwidth of the spectrum \mathbf{S} , i.e. $N_p \cdot \delta\lambda = \Delta\lambda$, then d_{scan} can be written into $d_{\text{scan}} = N_p \lambda^2 / 2\Delta\lambda$. Hence for sdLCS, Δf reduces to $\Delta f = N_p / f_{\text{scan}}$. As a consequence, the SNR of a tdLCS system compares to the SNR of an sdLCS system as $\text{SNR}_{\text{TD}} = (\epsilon \cdot \mathbf{S}) / (h\nu \cdot \Delta f) = (\tau \cdot \epsilon \cdot \mathbf{S}) / (h\nu \cdot N_p) = \text{SNR}_{\text{SD}} / N_p$. In conclusion, sdLCS is N_p -times more sensitive than tdLCS, provided that both systems have the same f_{scan} , d_{scan} and ϵ . This sensitivity advantage can be exchanged for a speed advantage if f_{scan} is increased, i.e. an sdLCS system can measure N_p -times faster than a tdLCS system with equal sensitivity.

A change in f_{scan} – i.e. between a ‘fast’ and a ‘slow’ LCS system – results in an SNR change with a factor $\phi = \Delta f_{\text{slow}} / \Delta f_{\text{fast}} = (f_{\text{scan,slow}} d_{\text{scan,slow}}) / (f_{\text{scan,fast}} d_{\text{scan,fast}})$, which comprises $\phi = 2f_R \tau (\Delta R / \Delta L_{\text{max}})$ for a ‘fast’ system with the sdLCS settings (but without spectral detection) and a ‘slow’ system with the tdLCS settings. If in addition, spectral detection over N_p pixels is realized for the ‘fast’ system (as for our sdLCS system), the SNR will increase with a factor N_p . As a consequence, the SNR_{SD} of an sdLCS system relates to the SNR_{TD} of a tdLCS system as:

$$\text{SNR}_{\text{SD}} = \phi \cdot N_p \cdot \frac{\epsilon_{\text{SD}}}{\epsilon_{\text{TD}}} \cdot \text{SNR}_{\text{TD}} = 2f_R \cdot \tau \cdot N_p \cdot \frac{\epsilon_{\text{SD}}}{\epsilon_{\text{TD}}} \cdot \frac{\Delta R}{\Delta L_{\text{max}}} \cdot \text{SNR}_{\text{TD}} \quad (7.10)$$

which also considers a possible difference in detection efficiency between sdLCS and tdLCS.

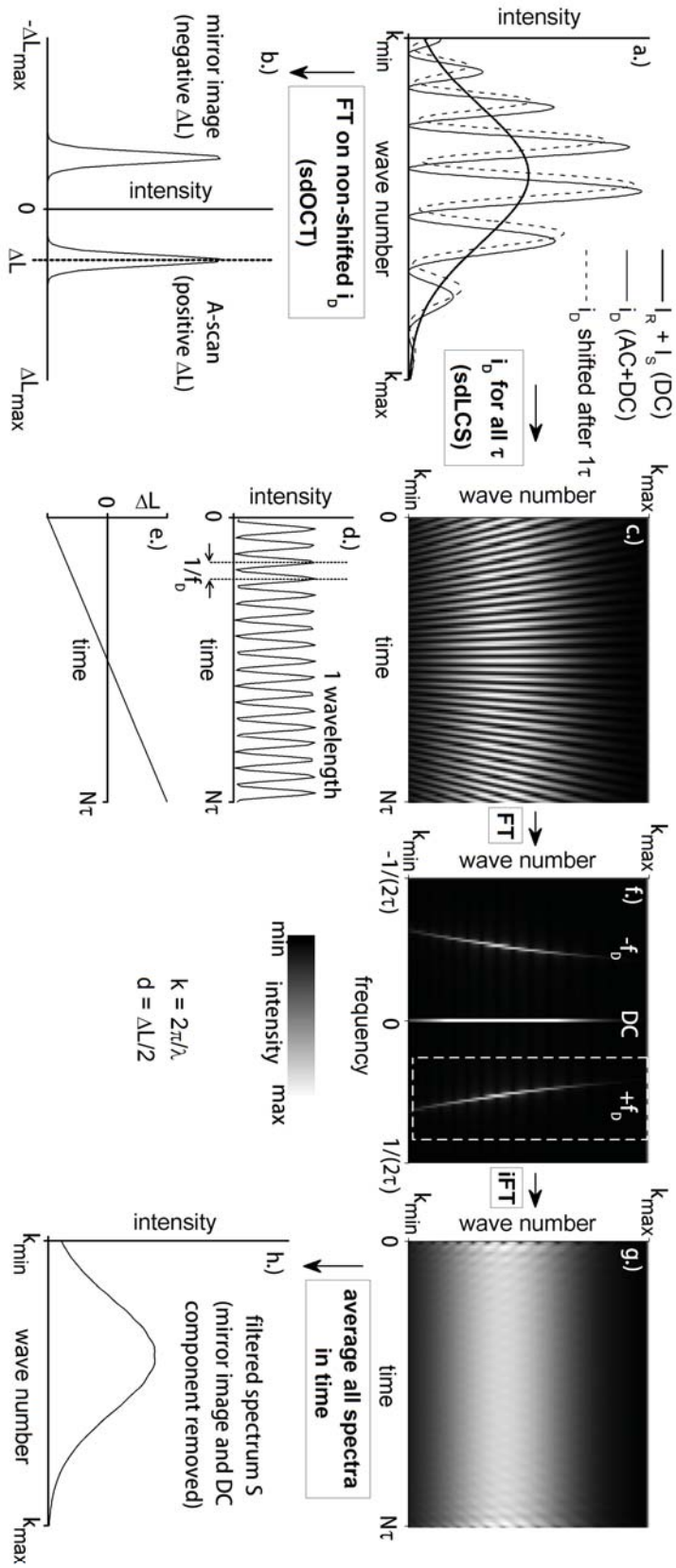


Figure 7.1 Signal acquisition and processing in sdLCS. See Section 7.2 for details.

7.3 Simulation

In order to validate the data acquisition and analysis approach described in Section 7.2, we simulated an absorption measurement on a sample containing oxyhemoglobin [12]. Since scattering was neglected in the simulation, the attenuation coefficient μ_t in Eq. 7.2 can be simplified to the absorption coefficient μ_a . The spectrum $\mathbf{S}(\ell)$ was calculated at $\ell_1 = 2$ mm and $\ell_2 = 4$ mm inside the sample, corresponding to depths $d_1 = 1$ mm and at $d_2 = 2$ mm, respectively.

The detecting spectrograph was simulated with the properties of the USB4000 ($\lambda_{\min} = 345$ nm, $\lambda_{\max} = 1042$ nm, $N_p = 3648$). The integration time was set at the minimal integration time of the USB4000 for these measurements, $\tau = 6$ ms. To meet the requirement in Eq. 7.7, the velocity of the reference mirror was set at $v_R = 6$ $\mu\text{m/s}$ (frequency $f_R = 0.3$ Hz, amplitude $\Delta R = 20$ μm). The source spectrum \mathbf{S}_0 was simulated as a Gaussian with center wavelength $\lambda_0 = 550$ nm and bandwidth $\lambda_{\text{FWHM}} = 140$ nm. The sample arm fraction was $\eta_S = 0.1$, resulting in a reference arm fraction of $\eta_R = 0.9$. A total number of $N = 125$ spectra was acquired over a time interval of $N\tau = 0.75$ s. The initial ΔL was set at -4.5 μm to achieve zero delay at $\frac{1}{2}N\tau$.

Figure 7.2 shows the result of this simulation. The $i_D(\lambda)$ at ℓ_1 and ℓ_2 show little influence of the sample's absorption (Figure 7.2a). However, after phase modulation and frequency domain filtering of $i_D(\lambda)$, the resulting spectra \mathbf{S} at ℓ_1 and ℓ_2 clearly show the presence of the oxyhemoglobin absorption peaks (Figure 7.2b). Using Beer's law, we obtain the absorption coefficient of the sample:

$$\mu_a = -\frac{1}{\frac{1}{2}(\ell_2 - \ell_1)} \ln\left(\frac{\mathbf{S}(\ell_2)}{\mathbf{S}(\ell_1)}\right) \quad (7.11)$$

From Figure 7.2c, we can conclude that our method of data acquisition and analysis for sdLCS fully recovers the input μ_a of this simulation.

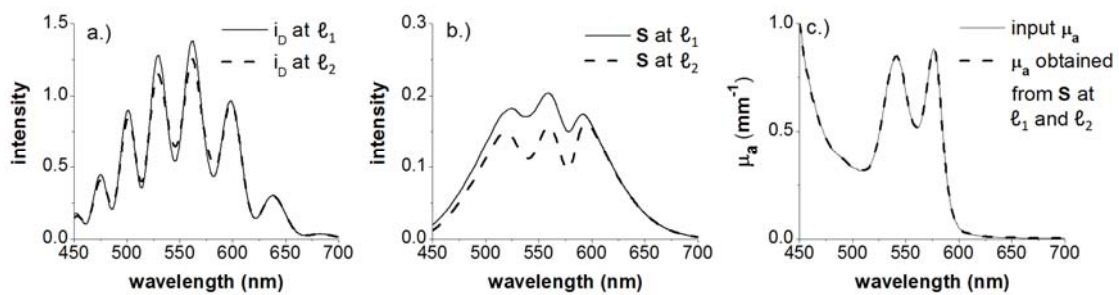


Figure 7.2 Simulation of a μ_a measurement in sdLCS. a.) input spectra i_D and b.) filtered spectra \mathbf{S} at path lengths ℓ_1 and ℓ_2 inside the sample. c.) input μ_a and recovered μ_a from Eq. 7.8.

7.4 The path length window $\Delta\ell$ in sdLCS

In sdLCS, the path length window over which $S(\ell)$ is acquired depends not only on the reference mirror scanning window in the medium ($\Delta\ell_R = 2\Delta R/n_g = 30 \mu\text{m}$ with the settings of Section 7.3 and group refractive index $n_g = 1.35$), but also on the path length window that is probed by the spectrograph $\Delta\ell_S$. The latter is a combination of $2\Delta L_{\text{max}}$ (due to mirror image removal) and the sensitivity roll-off with ΔL of the spectrograph. For the USB4000, we can calculate that $2\Delta L_{\text{max}} = 1880 \mu\text{m}$ (Eq. 7.4), but its sensitivity roll-off is not readily available.

To determine the sensitivity roll-off of the USB4000, we both calculated (Eq. 7.5) and measured its roll-off function. Since the only unknown parameter in Eq. 7.5 is the spectral resolution Δk (or $\Delta\lambda = 2\pi/\Delta k$), we measured $\Delta\lambda = 6 \text{ nm}$ as the FWHM of a 543 nm and 633 nm HeNe laser line, projected on the spectrograph. This spectral resolution results in a theoretical sensitivity roll-off with a FWHM of $18 \mu\text{m}$, indicated by the dotted line in Figure 7.3.

We experimentally determined the sensitivity roll-off by measuring the reflection from a glass slide in the sample arm as a function of ΔL between the sample arm and the reference arm, using Eq. 7.3. The measured $i_D(\lambda)$ was resampled to a linear k-scale. The resulting sensitivity roll-off function is shown in Figure 7.3 and agrees very well with the theoretical function. Note that the width (FWHM) of the reflections at each value of ΔL is close to twice the coherence length ($2 \cdot l_c \approx 3 \mu\text{m}$, Eq. 4.4) of the source (identical to the source in Chapters 4 to 6), and therefore agrees with the theoretical resolution for ΔL .

Since the FWHM of the sensitivity roll-off of the USB4000 is $18 \mu\text{m}$, which is many times smaller than the $2\Delta L_{\text{max}}$ of $1880 \mu\text{m}$, the path length window that is probed by the USB4000 can be approximated with $\Delta\ell_S = 18/n_g = 13 \mu\text{m}$. This $\Delta\ell_S$ probes a path length window around every path length ℓ in the reference mirror scanning window $\Delta\ell_R$. Hence, the full path length window that is probed in sdLCS is a convolution of $\Delta\ell_R$ with $\Delta\ell_S$, resulting in $\Delta\ell = \Delta\ell_R + \Delta\ell_S = 30 + 13 = 43 \mu\text{m}$ (inset of Figure 7.3).

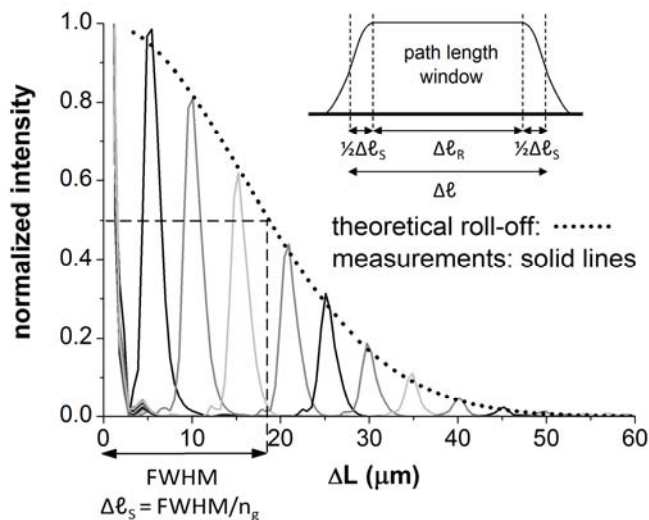


Figure 7.3 Theoretical and measured sensitivity roll-off of the USB4000. Inset: illustration of the path length window $\Delta\ell$ in sdLCS.

7.5 Experimental validation – Methods

To experimentally validate our approach for sdLCS (Section 7.2), we measured attenuation spectra μ_t from 480 to 700 nm on a phantom with known absorption μ_a and scattering μ_s coefficient spectra and we separated the individual contributions of μ_a and μ_s from the measured μ_t . In addition, we compared our sdLCS results to the results of a tdLCS measurement on the same phantom with the tdLCS system described in Chapters 4 to 6 (Figure 4.1) [1-3].

Table 7.1 Acquisition settings for sdLCS and tdLCS

acquisition parameter	sdLCS	tdLCS
$\Delta\ell$	43 μm	44 μm
$\Delta\lambda$	6 nm (all λ)	4 nm @ $\lambda=480$ nm 9 nm @ $\lambda=700$ nm
v_R	0.006 mm/s	1.84 mm/s
f_R	0.3 Hz	23 Hz
ΔR	20 μm	40 μm
N = # averages per ℓ	250	250
acquisition time of $\mathbf{S}(\ell)$	$N\tau = 1.5$ s	$N/(2f_R) = 5.4$ s

7.5.1 System and acquisition

The sdLCS system described in this Chapter is identical to the tdLCS system in Chapters 4 to 6, except for the detection end of the system, which consists of a spectrograph rather than a photodiode/lock-in amplifier combination. Hence, the multimode detection fiber is connected to the detecting spectrograph (USB4000), from which the properties have been described in Section 7.3.

For both the sdLCS and tdLCS measurements, we controlled ℓ ($\ell = 0 - 2000$ μm) by translating the reference mirror in steps of 27 μm . By translating the sample in the axial direction, focus tracking of the spot size ($r = 4.5$ μm) in the medium was achieved. At every ℓ , back scattered power spectra $\mathbf{S}(\ell)$ were obtained over a path length window in the medium of $\Delta\ell = 43$ μm for sdLCS (see Sections 7.2 and 7.4) and $\Delta\ell = 44$ μm for tdLCS (see Chapter 4). For both sdLCS and tdLCS, $\mathbf{S}(\ell)$ was temporally averaged ($N = 250$ spectra per ℓ) and corrected for the background (i.e. the LCS spectrum obtained from the non-scattering glass of the inner cuvette wall of the sample). The integration time for the sdLCS measurements was set at $\tau = 6$ ms and the reference mirror velocity at $v_R = 6$ $\mu\text{m/s}$, identical to the settings of the simulation (Section 7.3). The acquisition

settings for the tdLCS measurements were identical to the settings in Chapters 4 to 6 [1-3]. For both sdLCS and tdLCS, the most important acquisition parameters have been summarized in Table 7.1. Note that the acquisition speed for one temporally averaged spectrum $\mathbf{S}(\ell)$ is 3.6 times faster for sdLCS.

Similar to the data analysis in Chapters 4 to 6, fitting the single exponential decay model $\mathbf{S}(\ell) = \alpha \cdot \exp(-\mu_t \cdot \ell)$ (free running fit parameters α and μ_t) to the sdLCS and tdLCS acquired $\mathbf{S}(\ell)$ vs. ℓ , results in a μ_t spectrum for both detection methods [1-3]. Uncertainties in α and μ_t are estimated by their 95% confidence intervals (c.i.). Since the spectral resolution in sdLCS ($\Delta\lambda = 6$ nm, Section 7.4) is higher than the pixel width of 0.2 nm, $\mathbf{S}(\ell)$ was binned into wavelength regions of 6 nm for the sdLCS measurements. The values of μ_a and μ_s were obtained by fitting their individual contributions to the measured μ_t , as described in Chapter 6.2.2 [3].

7.5.2 Phantom

We prepared one phantom, consisting of 0.096 vol% NIST-certified polystyrene spheres ($\varnothing 602 \pm 6$ nm, Thermo Scientific, USA) and 10% magenta dye (Ecoline #337, Royal Talens, The Netherlands). The μ_s of the polystyrene spheres was calculated using Mie theory and integrated over the size distribution of the spheres ($2 \cdot SD$), as described in Chapter 5.2.4 [2]. The μ_a of the dye was determined in a separate transmission measurement on the dye only, as described in Chapter 4.3.2 [1]. For the tdLCS measurements, both reference spectra for μ_s and μ_a were convolved with a Lorentzian with a line width of 9 nm for adequate comparison to the LCS spectra that are Doppler broadened by Brownian motion (Chapters 4 to 6) [1-3]. For the sdLCS measurements, Brownian motion does not induce spectral broadening, because the Doppler shifted frequencies are still within the bounds of the frequency domain filter (Figure 7.1f). Since the reference spectrum of μ_s was obtained with the same spectral resolution as the LCS spectra, we did not broaden this spectrum. The reference spectrum of μ_s was convolved with a Lorentzian with a line width of 6 nm ($\Delta\lambda$ of the USB4000).

7.5.3 SNR comparison of sdLCS and tdLCS

In order to compare the sensitivity of the current sdLCS system to the tdLCS system, we measured the SNR of the two detection methods, using a mirror in the sample arm. The optical powers in the sample and reference arm were equal and the acquisition settings in Table 7.1 were applied. For both sdLCS and tdLCS, the spectrally resolved SNR was determined from the measured spectrum \mathbf{S} using:

$$\text{SNR} = 10 \cdot \log \left(\frac{\mathbf{S}}{\text{var}(\text{noise})} \right) \quad (7.12)$$

and normalized to zero SNR. In Eq. 7.12 $\text{var}(\text{noise})$ denotes the variance of the noise floor in \mathbf{S} for both methods, determined in the wavelength region between 310 and 385 nm where no signal was expected.

Based on Eq. 7.10, we can calculate the expected difference in SNR between both systems. The LCS spectrum covers approximately $N_p = 1150$ pixels on the USB4000. Based on a maximum number of $4 \cdot 10^6$ counts per photon and a pixel well depth of $1 \cdot 10^5$ electrons, the quantum efficiency (QE = #electrons/photon) of the USB4000 is 2.5% at 600 nm. Using the photodiode response of 0.43 A/W (2001, New Focus, USA), we can

calculate that our tdLCS detector has a QE of 89% at 600 nm. With $\tau=6$ ms for our sdLCS system, the sensitivity advantage of the sdLCS measurements described in this Chapter reduces to 0.38. Hence, when using the USB4000 as a detector for sdLCS and the settings in Table 7.1, we can expect a decrease in SNR of 4.2 dB at 600 nm with respect to tdLCS.

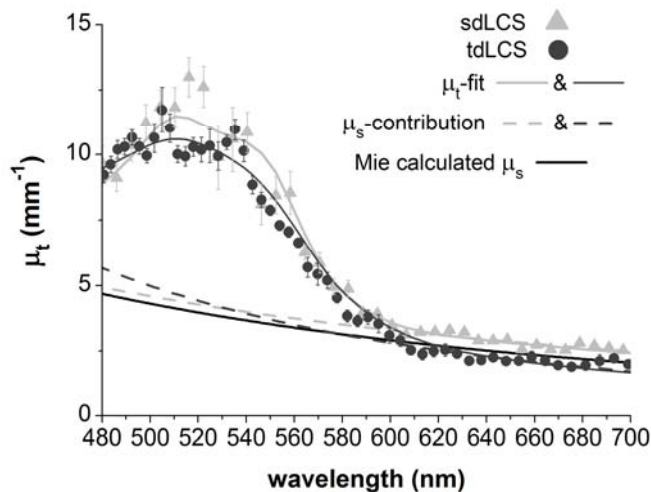


Figure 7.4 Comparison of an sdLCS measurement to a tdLCS measurement of μ_t , μ_a and μ_s on a polystyrene-dye phantom.

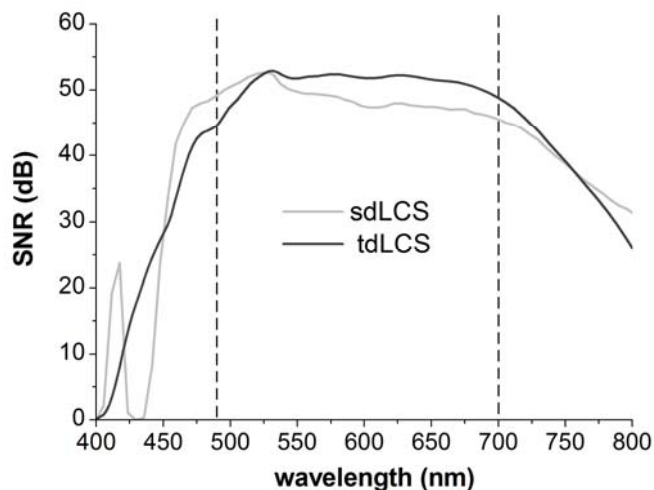


Figure 7.5 Signal to noise ratio (SNR) in sdLCS and tdLCS. The investigated spectral range for the measurements in this Chapter runs from 480 to 700 nm (dashed lines).

7.6 Experimental validation – Results

Figure 7.4 shows the measured μ_t spectra by sdLCS and tdLCS on the polystyrene-dye phantom. The μ_t spectra from both detection methods agree within the estimated uncertainties (error bars) for nearly all wavelengths. Also the fits on μ_t and the μ_s -contributions to the fits agree well, and the μ_s -contributions are in good agreement

with the Mie calculated μ_s . The fitted dye concentrations were $10.1 \pm 0.4\%$ for the sdLCS measurement and $9.5 \pm 0.4\%$ for the tdLCS measurement, which are both very close to the expected dye concentration of 10%.

Figure 7.5 shows the measured SNR on a mirror. For both sdLCS and tdLCS, the SNR is maximal within the investigated spectral range of 480 to 700 nm. For the majority of wavelengths within this region, the SNR of tdLCS is larger than the SNR of sdLCS, except for the shortest wavelengths ($\lambda < 530$ nm). The decrease in SNR for sdLCS is close to the predicted value of -4.2 dB (Section 7.5.3). Note that the SNR value for tdLCS differs from the value given in Chapter 4 (112 dB) due to a difference in method of analysis.

Whereas the SNR in Chapter 4 describes the minimally detectable signal with maximal amplification by the lock-in amplifier, the SNR in this Chapter is obtained with detection settings closer to actual measurements (e.g. with a backscatter coefficient larger than the minimal detectable reflectivity). However, the quantitative value of the SNR is of less importance here, since we primarily consider the differences in SNR in Figure 7.5 for the comparison between sdLCS and tdLCS.

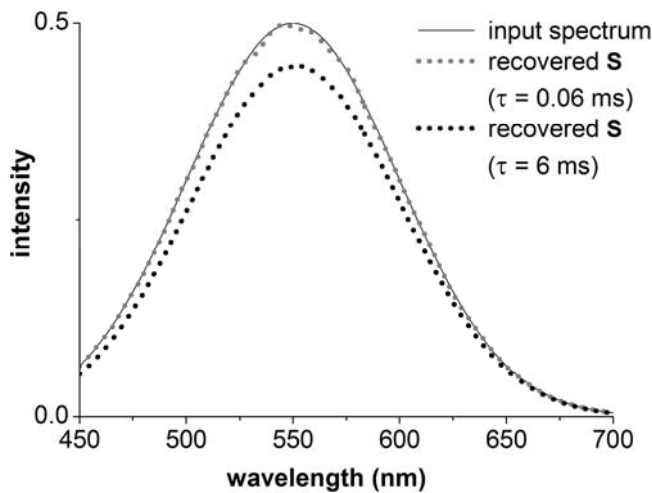


Figure 7.6 Simulation of the recovered spectrum S for two integration times: $\tau = 0.06$ ms (with $v_R = 60$ $\mu\text{m/s}$) and $\tau = 6$ ms (with $v_R = 6$ $\mu\text{m/s}$).

7.7 Discussion and conclusion

In this Chapter, we demonstrated and validated a new detection method and analysis algorithm for spectroscopic detection in LCS. We showed that this method can be used for measuring local μ_t , μ_a and μ_s spectra in turbid media. The results of the sdLCS phantom measurement agreed well with the expected optical properties of the phantom and were comparable to the measured optical properties by tdLCS (Figure 7.4).

The reason to validate this new detection method, is its theoretical sensitivity advantage compared to time domain detection (Section 7.2.2). As a consequence, the acquisition speed of the measurement can be reduced with respect to time domain detection, without reducing the signal to noise ratio. The sdLCS system that was

validated in this Chapter was more than three times faster than the tdLCS system, but not more sensitive (Figure 7.5). A sensitivity advantage for sdLCS could not be demonstrated, because the quantum efficiency of the USB4000 is not optimized for these experiments. However, if the quantum efficiency would be similar to that of our tdLCS detector, the sensitivity advantage would be $10\log(\phi N_p) = 11$ dB at equal acquisition times for tdLCS and sdLCS (Section 7.5.3).

Figure 7.5 shows a decrease in SNR of approximately 5 dB for sdLCS compared to tdLCS, which is slightly lower than the predicted decrease of 4.2 dB (Section 7.5.3) for these detection settings. The additional decrease in sensitivity can be explained by the relatively slow acquisition speed (167 Hz) of the USB4000. Slow acquisition speeds result in a decrease of the modulation depth in $i_D(\lambda)$ ('fringe wash-out'), due to the reference mirror movement induced change of ΔL within the integration time. Hence, the sensitivity of our sdLCS measurements can be improved by increasing the integration time with respect to the velocity of the reference mirror. The effect of fringe wash-out on spectral amplitude has been illustrated in Figure 7.6. Comparable to the simulation in Section 7.3, Figure 7.6 shows the recovered spectra \mathbf{S} from a simulation without absorption using integration times of $\tau = 6$ ms and $\tau = 0.06$ ms and reference mirror velocities of $6 \mu\text{m/s}$ and $60 \mu\text{m/s}$, respectively. Note that the integration times differ two orders of magnitude, whereas the reference mirror velocities only differ one order of magnitude. As a consequence, the spectrum \mathbf{S} for $\tau = 0.06$ ms has a higher amplitude ($\pm 15\%$, corresponding to 0.6 dB) and shows better agreement with the input sample arm spectrum ($\eta_s \cdot S_0$) than the spectrum \mathbf{S} for $\tau = 6$ ms. This simulation shows that, besides improvements on quantum efficiency, a faster spectrograph will further improve the performance of our sdLCS system. Since high quantum efficiency line scan cameras are available with line rates up to 140 kHz (e.g. the Basler Sprint spL4096-140km, Basler AG, Germany), enhanced sensitivity and/or acquisition speed are realizable for sdLCS.

The only technique that is reported to have comparable performance to our sdLCS system in terms of localized measurements of optical properties, is dual band sOCT [6,7]. However, this method may not be as well applicable on thin layers or small tissue volumes as our LCS system [3], since the spatial dimensions of the largest of the dual bands in this method may extend the dimensions of the volume of interest. In addition, our sdLCS system has the unique advantage of focus tracking, which prevents unwanted signal attenuation and a decrease in sensitivity at larger path lengths in the medium. This facilitates the exact determination of μ_s and μ_a contributions to the measured μ_t .

In conclusion, the new approach for sdLCS demonstrated in this Chapter has high potential to improve the accuracy and speed of localized optical property measurements by LCS. Undoubtedly, this will lead to improved clinical utility of the technique, e.g. for the non-invasive determination of blood composition (hemoglobin/bilirubin concentration and oxygen saturation).

References

1. N. Bosschaart, M.C.G. Aalders, D.J. Faber, J.J.A. Weda, M.J.C. van Gemert, T.G. van Leeuwen, "Quantitative measurements of absorption spectra in scattering media by low-coherence spectroscopy", *Optics Letters* **34**, 3746-3748 (2009)

2. N. Bosschaart, D.J. Faber, T.G. van Leeuwen, M.C.G Aalders, "Measurements of wavelength dependent scattering and backscattering coefficients by low-coherence spectroscopy", *Journal of Biomedical Optics*, **16**, 030503 (2011)
3. N. Bosschaart, D.J. Faber, T.G. van Leeuwen, M.C.G Aalders, "In vivo low-coherence spectroscopic measurements of local hemoglobin absorption spectra in human skin" *Journal of Biomedical Optics* **16**, 100504 (2011)
4. R. Leitgeb, C. K. Hitzenberger, and A. F. Fercher, "Performance of fourier domain vs. time domain optical coherence tomography", *Optics Express* **11**, 889-894 (2003)
5. D.J. Faber, T.G. van Leeuwen, "Optical coherence tomography", Chapter 18 in *Optical-Thermal Response of Laser-Irradiated Tissue*, A.J. Welch, M.J.C. van Gemert, Eds., pp. 713 - 741 (Springer Science + Business Media B.V., 2010)
6. F. Robles, R.N. Graf, A. Wax, "Dual window method for processing spectroscopic optical coherence tomography signals with simultaneously high spectral and temporal resolution", *Optics Express* **17**, 6799-6812 (2009)
7. F.E. Robles, C. Wilson, G. Grant, A. Wax, "Molecular imaging true-colour spectroscopic optical coherence tomography", *Nature Photonics*, doi:10.1038/nphoton.2011.257 (2011)
8. D.J. Faber, T.G. van Leeuwen, "Doppler calibration method for spectral domain OCT spectrometers", *Journal of Biophotonics* **2**, 407-415 (2009)
9. M. Sarunic, M.A. Choma, C. Yang, J.A. Izatt, "Instantaneous complex conjugate resolved spectral domain and swept-source OCT using 3x3 fiber couplers", *Optics Express* **13**, 957-967 (2005)
10. J. Zhang, J.S. Nelson, Z. Chen, "Removal of a mirror image and enhancement of the signal-to-noise ratio in Fourier-domain optical coherence tomography using an electro-optic phase modulator", *Optics Letters* **30**, 147-149 (2005)
11. N. Nassif, B. Cense, B. Park, M. Pierce, S. Yun, B. Bouma, G. Tearney, T. Chen, J. de Boer, "In vivo high-resolution video-rate spectral-domain optical coherence tomography of the human retina and optic nerve", *Optics Express* **12**, 367-376 (2004)
12. Data tabulated from various sources compiled by S. Prael, <http://omlc.ogi.edu/spectra>

CHAPTER 8

Concluding remarks and outlook

This Chapter reflects on the content of this thesis. The current status of LCS as a technique for non-invasive bilirubinometry is discussed and possibilities for further improvement of the technique are addressed. Since the application of LCS is not restricted to bilirubinometry on neonates, we also describe other potential applications for this new technique.

8.1 Introduction

In Chapters 1 and 2, the limitations of currently used optical techniques for transcutaneous bilirubinometry were introduced: whereas transcutaneous bilirubinometers are suited as a screening method for hyperbilirubinemia, these devices cannot serve as a replacement of invasive blood sampling. The major reason for this is the fact that these devices measure the extravascular bilirubin concentration, which cannot be directly related to the parameter of interest: the intravascular, or total serum bilirubin concentration (TSB). We suggested two approaches to solve this problem, from both a medical and a technological perspective. This thesis focused on the technological approach, by designing a spectroscopic technique (low-coherence spectroscopy, LCS) that can confine its probing volume to the intravascular space only. Thereby, a one to one comparison between the spectroscopic bilirubin measurement and the TSB can be achieved. Hence, LCS may become the technique that can completely replace invasive blood sampling for TSB determination, leading to less pain, stress and a faster diagnosis for jaundiced neonates.

Since LCS is a new technique, this thesis describes the essential first steps in the design, development and validation of the technique (Chapters 4 and 5). The measured attenuation coefficients ($0.15 - 34 \text{ mm}^{-1}$) by LCS on tissue simulating phantoms are within the range of the neonatal skin optical properties described in Chapter 3 ($\mu_t = \mu_a + \mu_s'/(1-g) \approx 10 - 20 \text{ mm}^{-1}$ when a scattering anisotropy of $g = 0.85$ is assumed [1]). In addition to the phantom experiments, we proved that we can use LCS to measure local absorption coefficient spectra in real, living tissue and that biologically relevant chromophore concentrations could be obtained from the measured absorption spectra (Chapter 6). To further improve the acquisition speed and sensitivity of the technique, Chapter 7 presented a new method for spectroscopic detection in LCS. Hence, we demonstrated that LCS is a very promising technique for non-invasive bilirubin measurements.

Before LCS can be clinically applied, further research is needed on 1) the applicability of LCS for measuring the μ_t in whole blood, 2) the quantification of bilirubin concentrations from the measured μ_t of whole blood and 3) improvements on the speed, sensitivity and design of our current LCS system. Sections 8.2 and 8.3 of this Chapter discuss these issues in detail. Since the application of LCS is not restricted to bilirubinometry, Section 8.4 discusses other potential applications for this new technique.

8.2 *In vivo* LCS measurements of whole blood

As described in Chapters 1 and 2, and Section 8.1, we intend to use LCS for measuring the absorption coefficient spectrum within a single blood vessel. From the measured spectrum, we want to obtain the bilirubin concentration in whole blood, comparable to our method of obtaining the hemoglobin concentration in Chapter 6.2.2. Naturally, this raises the question: is LCS sensitive enough to measure the high attenuation associated with the large absorption and scattering in whole blood?

Based on the measured SNR of our tdLCS system (~ 50 dB, Figure 7.5), we should be able to measure optical densities ($\text{OD} = \mu_t \cdot \ell$) of maximally $\ln(10^5) = 11.5$. The epidermal OD measured in Chapter 6 was approximately 0.8. Hence, if we measure inside a blood vessel located beneath the epidermis, the remaining maximal OD for our measurement is $11.5 - 0.8 = 10.7$. If we assume a diameter of 0.1 mm ($\ell = 0.2$ mm) for this blood vessel, the maximal attenuation coefficient that LCS can measure over the full diameter of this vessel is $\mu_t = 10.7/0.2 = 53.5 \text{ mm}^{-1}$.

Around the center wavelength of our LCS system, whole blood has an absorption coefficient of $\sim 30 \text{ mm}^{-1}$ and a scattering coefficient of $\sim 300 \text{ mm}^{-1}$ [2], resulting in a total attenuation coefficient of $\mu_t \approx 330 \text{ mm}^{-1}$. This μ_t for whole blood is larger than the maximal attenuation coefficient that LCS can measure. However, when measuring on such a highly scattering medium with large anisotropy ($g = 0.99$) [2], multiple scattering contributions to the LCS signal are inevitable. As was discussed in Chapter 5, these contributions can lower the effective μ_s -contribution to the μ_t that is measured by LCS, while the μ_a -contribution remains unaffected, since absorption takes place along the photon's path (Chapter 4). Although we do not know the exact influence of these and other effects on LCS measurements on whole blood, we will show an experimental validation of the performance of LCS on whole blood in the next section.

8.2.1 Experimental validation

To validate the performance of LCS in whole blood, we performed an *in vivo* tdLCS measurement on the nail and the underlying nail bed of the index finger of a healthy human volunteer. The measurement settings and method of analysis were identical to the methods described in Chapter 6.2. Figure 8.1 shows the resulting OCT image, with three dark regions in the nail bed, which are presumably blood vessels. A region of interest within one of the presumed blood vessels was selected (dashed rectangle: $200 \times 110 \mu\text{m}^2$, width \times depth) for the determination of μ_t . The measured attenuation coefficient spectrum (dots) within this region was fitted with a μ_t -fit (solid line) as described in Chapter 6.2.2, assuming the presence of oxygenized and deoxygenized hemoglobin in the vessel. The OD of the tissue covering the blood vessel was approximately 0.75.

The highest measured μ_t -values within the vessel (57 mm^{-1}) are close to the predicted maximal measurable value of 53.5 mm^{-1} . The μ_s -contribution to the μ_t -fit ($\sim 5 \text{ mm}^{-1}$) is low compared to the expected μ_s for whole blood, which may be explained by the contribution of multiple scattering to the LCS signal. Strikingly, the measured and fitted values of μ_t are very similar to the absorption coefficient of whole blood [2]. In fact, the fitted total hemoglobin concentration ([tHb]) was $143 \pm 24 \text{ g/L}$, which is within the physiological [tHb] range of 134 to 173 g/L for whole blood [2]. In addition, the fitted oxygen saturation (SO_2) of $60 \pm 29 \%$ resembled the SO_2 of venous blood [3].

These results show that *in vivo* LCS measurements on whole blood within a blood vessel are possible. Although the current accuracy of the measurement is too low for clinical applications, this accuracy is likely to be improved when the configuration for sdLCS is optimized (Chapter 7 and Section 8.3.1).

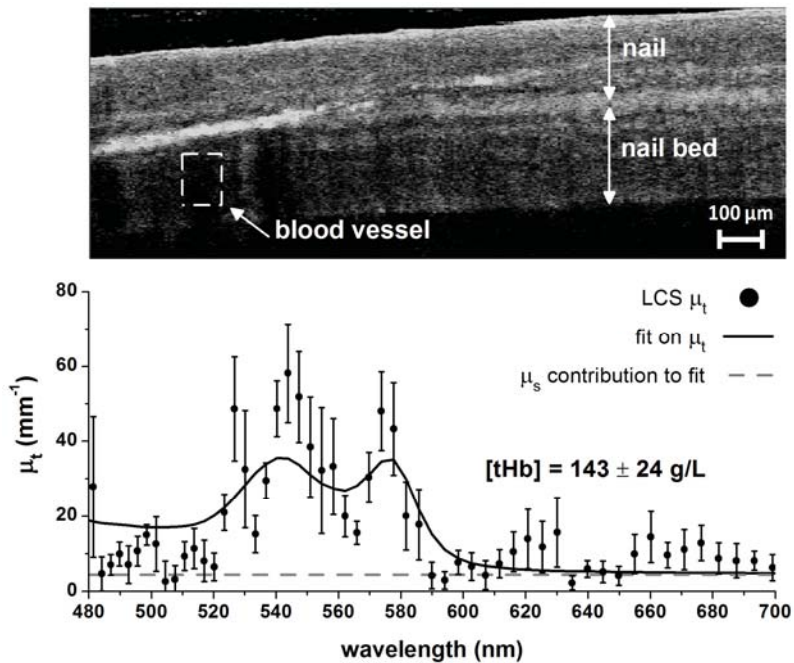


Figure 8.1 In vivo LCS measurement on a blood vessel under the nail of an index finger. The upper OCT image shows the nail, the nail bed and the selected blood vessel region for the determination of μ_t (dashed rectangle). The lower graph shows the attenuation spectrum within the selected region, the fit on μ_t and the μ_s -contribution to the μ_t -fit. The fitted total hemoglobin concentration $[tHb]$ (143 ± 24 g/L) is within the physiological $[tHb]$ range of 134 to 173 g/L for whole blood.

8.2.2 Blood flow influences on the LCS signal

Blood flow induces Doppler shifting of the modulation frequency of the LCS signal. This has different consequences for tdLCS and sdLCS. Since the frequency shifted signals are remapped to a wavelength axis in tdLCS, Doppler shifting by blood flow induces a translation of the LCS spectrum along the wavelength axis, comparable to the spectral broadening by Brownian motion (Chapter 4). This may not only induce an error in the determination of the optical coefficients, it may also lead to a complete loss of signal if the frequency shift extends the bounds of the lock-in filter. Although we did not encounter any influences of blood flow induced Doppler shifting in the measurements presented in Chapter 6 and Section 8.2.1, the influences of blood flow should not be overlooked when using tdLCS. To avoid Doppler shifting of the LCS signal, the angle of incidence on the blood vessel can be set to 90 degrees. Since this may be difficult to realize in practice, a temporary stop of blood flow can be realized during the measurement by a (manual) occlusion of the vessel.

For sdLCS, Doppler shifting by blood flow has less influence on the measured spectrum compared to tdLCS. Since a Doppler frequency shift will be negligible compared to the frequency of light, a translation of the measured spectrum along the wavelength axis will not occur. However, a Doppler frequency shift extending the bounds of the frequency domain filter (Figure 7.1f) can induce loss of signal. The latter

may be avoided by a careful choice of the modulation frequency and filter bounds, a 90 degree angle of incidence or temporary occlusion of the vessel. Another effect of blood flow on the sdLCS signal may be a decrease of the modulation depth in $i_D(\lambda)$ ('fringe wash-out', see Chapter 7.7), since the scattering red blood cells move during the integration time of the spectrograph. This problem may be solved by faster acquisition (Section 8.3.1).

8.2.3 Bilirubin concentration measurements by LCS

The *in vivo* LCS measurements described in Chapter 6 and Section 8.2.1 focused on the measurement of oxygenized and deoxygenized hemoglobin concentrations. Although this does not directly demonstrate the capability of LCS to measure bilirubin concentrations, it proves the capability of the technique to derive biologically relevant tissue chromophore concentrations from an attenuation coefficient spectrum. The bilirubin absorption peak around 460 nm (Figure 1.1) falls just outside the spectral range of our LCS measurements, because of the decrease in SNR in this region (Figure 7.5). Although the SNR around 460 nm of the sdLCS system shows an improvement with respect to tdLCS, further improvements in LCS system design may be needed for accurate bilirubin concentration measurements (Section 8.3.1).

For the clinical assessment of whole blood bilirubin concentrations in neonates, an accuracy of at least 10 $\mu\text{mol/L}$ within the range of 40 to 400 $\mu\text{mol/L}$ is desired, which translates into an accuracy of 0.13 mm^{-1} for the determination of μ_a . Although the current accuracy in μ_a of 0.5 mm^{-1} is close to this required value (Chapter 4), further improvements on LCS accuracy are needed (Section 8.3.1). Nevertheless, with the current accuracy in μ_a we would be able to measure bilirubin concentration changes of 40 $\mu\text{mol/L}$, which is comparable to the accuracy of existing transcutaneous bilirubinometers [4]. Hence, further research on LCS for non-invasive bilirubinometry is justified.

In contrast to the existing bilirubinometers, LCS can potentially be applied for continuous monitoring of bilirubin levels, which may provide more insight into bilirubin physiology and reduces the time for treatment decision making. Existing devices cannot be used for this purpose, because photo bleaching of bilirubin decreases the bilirubin concentration in the extravascular space [5], introducing an additional measurement error. Since LCS will be applied for bilirubin concentration measurements on flowing blood in the intravascular space, the effect of photo bleaching will be negligible.

8.3 Possibilities for LCS system improvement

8.3.1 Speed and sensitivity

As mentioned in Chapter 7 and Section 8.2, the speed and sensitivity of the current LCS system need to be improved. In Section 7.2.2, we showed that spectroscopic detection with sdLCS induces a theoretical sensitivity advantage compared to tdLCS. Furthermore, a trade-off exists between the speed and sensitivity of an LCS system, since acquisition speed can be enhanced by sacrificing sensitivity.

Since the quantum efficiency and acquisition speed of the USB4000 spectrograph, used for spectral detection, are not optimized for sdLCS, we could not demonstrate a

sensitivity advantage compared to tdLCS in Chapter 7. However, we did demonstrate that our method for spectroscopic detection in LCS is feasible. Therefore, the most straightforward method to realize a speed and sensitivity enhancement in LCS, is by implementing a spectrograph that is optimized for sdLCS. The maximal sensitivity advantage that can be achieved with an sdLCS system will depend on the number of pixels, the quantum efficiency, and the ΔL_{\max} of the spectrograph (Eq. 7.10). Hence, these parameters should be considered when optimizing the sdLCS system, as well as the trade-off between acquisition speed and sensitivity. In addition, sensitivity may be improved by (lateral) averaging of spectra, which increases the SNR with the square root of the number of averages.

As demonstrated in Chapter 7.7, a spectrograph with 17 kHz acquisition rate (100 times faster than the USB4000) matches the acquisition speed requirements for sdLCS. With this acquisition rate, the determination of the attenuation spectrum in the blood vessel of Section 8.2.1 would only take 12 ms. Since 140 kHz line rate cameras with high quantum efficiency are available [6], such an sdLCS system is realizable.

For the purpose of bilirubinometry, it may be advantageous to enhance the sensitivity of the sdLCS system for wavelengths around 460 nm (Section 8.2.3). The current SNR in this wavelength band is relatively low due to a combination of detector quantum efficiency and source power. Detector quantum efficiency around 460 nm can be enhanced by choosing a detector that is optimized for this wavelength range, e.g. visible/UV-enhanced detectors that have a considerably higher quantum efficiency compared to regular silicon based detectors below 500 nm [7,8]. Recently, supercontinuum sources became available with higher output power around 460 nm compared to the source in our LCS system [9]. Furthermore, collimated broad band LED's are available with high output power around the bilirubin absorption peak [10]. However, since these LED's do not have a single mode output spectrum, the effects of modal dispersion and intermodal interference need to be reevaluated when implementing these sources in our LCS system.

8.3.2 Compactness and clinical utility

Before LCS can be introduced into the clinic, several adjustments to the current bench-top system design are necessary. To reduce the size of the system, the open air optical paths can be replaced by fiber optic paths. In addition, the development of a fiber based probe in the sample arm will be necessary to facilitate clinical measurements. A fiber based LCS system requires careful design and choice of optical components, since a large wavelength bandwidth needs to be guided through single mode and/or multimode fibers while avoiding signal loss and the effects of modal dispersion and intermodal interference. Recent advances in the field of integrated optics have lead to e.g. chip-based spectrographs [11]. Therefore, further reduction of the LCS system size may be achieved by integrating several or more system components on a chip.

As was demonstrated in Chapter 6, lateral scanning of the sample is needed for spatial averaging of the LCS signal. The current implementation for lateral sample scanning involves movement of the sample with respect to the sample arm beam. For clinical purposes, it will be advantageous to scan the sample arm beam with respect to the sample. This can be achieved by implementing x/y-lateral scanning mirrors, as is

commonly done in clinical OCT systems [12]. The implementation of x/y-lateral scanning introduces the additional possibility to make a volume scan of the sample, instead of a single B-scan as in Figure 8.1, which facilitates the localization of blood vessels (Section 8.3.3). Also the current method for axial scanning of the sample, involving movement of the sample with respect to the sample lens, needs to be replaced by translation of the sample lens with respect to the sample. The latter will require an adjustment of the focus tracking scheme described in Chapter 4.

8.3.3 Blood vessel localization

In Chapter 6 and Section 8.2.1, the localization of the region of interest for the determination of μ_t was supported by an OCT image that was reconstructed from the LCS signal. Since only the spectral information within the region of interest is required, the relatively slow step-wise LCS scanning outside the region of interest may be replaced by other imaging modalities for blood vessel localization. Possible imaging modalities for this purpose are conventional OCT imaging, photoacoustic tomography [13] and side stream dark field (SDF) imaging [14]. Naturally, this requires precise coalignment of these modalities with the LCS signal. Although such a design has consequences for the compactness of the system, it is likely to result in a considerably faster localization of blood vessels that are suited for LCS μ_t -determination.

8.4 Other potential applications of LCS

Besides its value for non-invasive bilirubin measurements, LCS creates new opportunities within and outside the field of tissue spectroscopy. Supported by the structural tissue information of an OCT image, LCS offers the possibility to accurately and simultaneously quantify a unique set optical property spectra (μ_t , μ_a , μ_s and μ_b) and tissue chromophore concentrations within a very confined and controllable tissue volume of choice. No other spectroscopic technique is capable of doing such a determination. As a consequence, LCS solves many methodological problems related to conventional reflectance spectroscopy, e.g. assumptions on photon path lengths, probing volume and homogeneity of the investigated tissue. This offers new opportunities for tissue diagnostic applications.

Recent advances in the field of spectroscopic optical coherence tomography (sOCT), which is closely related to LCS (Chapter 4.1), further emphasize the need for techniques like LCS by showing progression in localized measurements of optical properties [15]. Since the focus of this research is on OCT image contrast enhancement, the quantification and localization of chromophore concentrations and attenuation spectra is not as accurate and well-validated as in LCS. Nevertheless, the research area of LCS and LCS-related research is becoming increasingly important in the field of tissue optics. This section describes other potential applications for LCS.

8.4.1 Applications based on absorption

In Chapter 6 and Section 8.2, we showed that LCS can be used for the determination of other chromophore concentrations than bilirubin. By measuring hemoglobin absorption spectra, not only the total hemoglobin concentration could be determined,

but also the oxygen saturation within the investigated tissue volume. Accurate determination of total hemoglobin concentrations and oxygen saturation within blood vessels can potentially replace the need for this determination by invasive blood sampling in both neonates and adults. In addition, knowledge of the hemoglobin concentration and oxygen saturation within confined tissue volumes consisting of both intravascular and extravascular tissue space can provide valuable information on tissue physiology and pathology, e.g. during shock.

The current LCS system was optimized for the visible wavelength range. As a consequence, only concentrations of chromophores with distinct absorption features within this wavelength region could be quantified. However, LCS is not limited to the visible range and may be extended to the ultraviolet and (near) infrared region for the quantification of e.g. water concentration (related to skin hydration) and potentially glucose concentration (for the monitoring of diabetic patients). Also the delivery and distribution of exogenous therapeutic and contrast agents with distinct absorption, or scattering features may be monitored by LCS.

8.4.2 Applications based on scattering

Chapter 5 demonstrated that LCS is not only a promising technique for the determination of local absorption coefficient spectra, but also for the determination of local scattering, and backscattering coefficient spectra. Based on this determination, we showed that LCS can be used for the characterization of samples, in terms of particle size and concentration. This may be an interesting application within the field of particle science. Furthermore, the quantitative and wavelength dependent measurement of μ_s and μ_b makes the technique sensitive for changes in cell morphology and organization, which may be relevant for (early) cancer detection and monitoring of tumor development [16]. The additional absorption coefficient based information on hemoglobin concentration and oxygen saturation, related to tumor vascularization [17], results in an extensive and unique set of 'tumor sensitive' parameters that can only be measured simultaneously by LCS. Hence, also the application of cancer diagnosis by LCS deserves further investigation.

In addition to the quantitative measurement of optical coefficients, LCS can also be used for deriving path length resolved blood flow, or perfusion related parameters from the back scattered signal. These parameters can be quantified by measuring the blood-flow related speckle decorrelation rate of the LCS signal, or the Doppler frequency shift (see also Section 8.2.2), as has been demonstrated before with other low-coherence interferometry based modalities [18,19].

8.5 Concluding remarks

Summarizing, this thesis described the essential first steps in the design, development and validation of LCS as a method for the quantitative and localized determination of tissue optical properties and chromophore concentrations. As an outlook, following the suggested steps on improving the speed and sensitivity of the technique is required before LCS can be introduced into the clinic for the purpose of non-invasive bilirubinometry and other potential applications. Nevertheless, even with the sub-

optimal sensitivity of the current time domain LCS system, we can already show that LCS can be used for measuring the μ_a within a single blood vessel in human skin, and that the derived hemoglobin concentration is well within the range of normal human whole blood hemoglobin concentrations. Therefore, LCS is a very promising technique that deserves further development and can potentially lead to less pain and complications for preterm neonates.

References

1. M.J.C. van Gemert, S.L. Jacques, H.J.C.M. Sterenborg, W.M. Star, "Skin Optics", *IEEE Transactions on Biomedical Engineering* **36**, 1146-1154 (1989)
2. A. Roggan, M. Friebel, K. Dörschel, A. Hahn, G. Müller, "Optical properties of circulating human blood in the wavelength range 400-2500 nm", *Journal of Biomedical Optics* **4**, 36-46 (1999)
3. A. Keys, "The oxygen saturation of the venous blood in normal human subjects", *American Journal of Physiology*, 13-21 (1938)
4. K. Grohmann, M. Roser, B. Rolinski, I. Kadow, C. Muller, A. Goerlach-Graw, M. Nauck, H. Kuster, "Bilirubin measurement for neonates: comparison of 9 frequently used methods", *Pediatrics* **117**, 1174-1183 (2006)
5. G. Agati, F. Fusi, G.P. Donzelli, R. Pratesi, "Quantum yield and skin filtering effects on the formation rate of lumirubin", *Journal of Photochemistry and Photobiology B: Biology* **18**, 197-203 (1993)
6. Basler Sprint line scan camera: www.baslerweb.com
7. Princeton Instruments CCD camera's: www.princetoninstruments.com
8. Andor Technology CCD camera's: www.andor.com
9. Fianium supercontinuum sources: www.fianium.com
10. Thorlabs collimated LED sources: www.thorlabs.de
11. V.D. Nguyen, B.I. Akca, K. Worhoff, R.M. de Ridder, M. Pollnau, T.G. van Leeuwen, J. Kalkman, "Spectral domain optical coherence tomography imaging with an integrated optics spectrometer", *Optics Letters* **36**, 1293-1295 (2011)
12. E.A. Swanson, J.A. Izatt, M.R. Hee, D. Huang, C.P. Lin, J.S. Schuman, C.A. Puliafito, J.G. Fujimoto, "In vivo retinal imaging by optical coherence tomography", *Optics Letters* **18**, 1864-1866 (1993)
13. L.V. Wang, "Multiscale photoacoustic microscopy and computed tomography", *Nature Photonics* **3**, 503-509 (2009)
14. P.T. Goedhart, M. Khalilzada, R. Bezemer, J. Merza, C. Ince, "Sidestream dark field (SDF) imaging: a novel stroboscopic LED ring-based imaging modality for clinical assessment of the microcirculation", *Optics Express* **15**, 15101-15114 (2007)
15. F.E. Robles, C. Wilson, G. Grant, A. Wax, "Molecular imaging true-colour spectroscopic optical coherence tomography", *Nature Photonics*, doi:10.1038/nphoton.2011.257 (2011)
16. H. Subramanian, H.K. Roy, P. Pradhan, M.J. Goldberg, J. Muldoon, R.E. Brand, C. Sturgis, T. Hensing, D. Ray, A. Bogojevic, J. Mohammed, J. Chang, V. Backman, "Nanoscale cellular changes in field carcinogenesis detected by partial wave spectroscopy", *Cancer Research* **69**, 5357-5363 (2009)
17. P. Vaupel, F. Kallinowski, P. Okunieff, "Blood flow, oxygen and nutrient supply, and metabolic microenvironment of human tumors: a review", *Cancer Research* **49**, 6449-6465 (1989)
18. J. Kalkman, R. Sprik, T.G. van Leeuwen, "Path-length-resolved diffusive particle dynamics in spectral domain optical coherence tomography", *Physical Review Letters* **105**, 198302 (2010)
19. B. Varghese, V. Rajan, T.G. van Leeuwen, W. Steenbergen, "Path-length-resolved optical Doppler perfusion monitoring", *Journal of Biomedical Optics* **12**, 060508 (2007)

List of symbols

<u>general</u>		<u>LCS system and geometry</u>	
t	time	x_S	sample arm length
f	frequency	x_R	reference arm length
λ	wavelength	ΔL	optical path length difference
k	wave number	λ_0	center wavelength
d	depth	λ_{FWHM}	wavelength bandwidth
ℓ	geometrical path length	l_c	coherence length
$\Delta\lambda$	wavelength resolution	S_0	source power spectrum
Δk	wave number resolution	T_c	system coupling efficiency
Δf	frequency resolution	ζ	system calibration constant
h ν	photon energy	α	scaling factor
\varnothing	diameter	ℓ_F	focus position in path length units
r	radius	Z_R	Rayleigh length
D	thickness	w	beam waist
<u>optical properties</u>		Ω	solid angle
μ_t	attenuation coefficient	θ	(focusing) angle
μ_a	absorption coefficient	M	number of modes
μ_s	scattering coefficient	<u>LCS acquisition</u>	
μ_s	reduced scattering coefficient	Δx_S	sample arm displacement
μ_b	backscattering coefficient	Δx_R	reference arm displacement
$\mu_{b,NA}$	NA-corrected μ_b	v_R	reference mirror velocity
μ_{eff}	effective attenuation coefficient	f_R	reference mirror scanning frequency
$p(\theta)$	scattering phase function	ΔR	reference mirror scanning amplitude
g	scattering anisotropy	$\Delta\ell$	path length scanning window
n	phase refractive index	N	number of samples
n_g	group refractive index	f_s	sampling frequency
a	scattering scaling factor	<u>Brownian motion</u>	
b	scatter power	Δf_D	Doppler frequency shift
c	chromophore concentration	k_B	Boltzmann constant
<u>diffusion theory</u>		T	temperature
I	spectral intensity	η	viscosity
R	remittance	<u>LCS spectroscopic detection</u>	
r_j	fiber distance from source	η_S, η_R	sample/reference arm fraction
z_0	modeled source position	$d_{max}, \Delta L_{max}$	imaging depth/path length
z_b	modeled virtual source position	$\delta k, \delta\lambda$	spectrometer pixel width
A	empirical parameter	N_p	# pixels
α	proportionality factor	τ	integration time
β, γ	validity limiting parameters	f_D	Doppler frequency
<u>LCS signal description</u>		ϵ	detection efficiency
E_S	electric field in the sample arm	$\Delta\ell_R$	reference mirror scanning window
E_R	electric field in the reference arm	$\Delta\ell_S$	spectrograph probing window
E_D	electric field at the detector	(bold-faced printed characters in this thesis denote wavelength dependent parameters)	
I_S	sample arm intensity		
I_R	reference arm intensity		
i_D	photo detector current		
i_{AC}	AC photo detector current		
S	power spectrum		

List of abbreviations

LCS related abbreviations

LCS low-coherence spectroscopy
 tdLCS time domain LCS
 sdLCS spectroscopic detection LCS

OCT optical coherence tomography
 sOCT spectroscopic OCT

FWHM full width at half maximum
 PSF point spread function
 NA numerical aperture
 OD optical density
 GD group dispersion

FT Fourier transform
 SNR signal to noise ratio
 QE quantum efficiency
 AC alternating current
 DC direct current

NIST National Institute of Standards and
 Technology
 PS polystyrene
 IL Intralipid
 TiO₂ titanium dioxide

error estimation

c.i. confidence interval
 SD standard deviation
 PL prediction limit
 var variance

physiology

Hb deoxygenized hemoglobin
 HbO₂ oxygenized hemoglobin
 [tHb] total hemoglobin concentration
 SO₂ oxygen saturation

TcB cutaneous bilirubin concentration
 TSB total serum bilirubin concentration
 TcHb cutaneous Hb concentration
 TcHbO₂ cutaneous HbO₂ concentration
 BVF blood volume fraction

other

CCD charge coupled device

List of publications

- N. Bosschaart, M.C.G. Aalders, D.J. Faber, J.J.A. Weda, M.J.C. van Gemert, T.G. van Leeuwen, "Quantitative measurements of absorption spectra in scattering media by low-coherence spectroscopy", *Optics Letters* **34**(23), 3746-3748 (2009)
- N. Bosschaart, D.J. Faber, T.G. van Leeuwen, M.C.G Aalders, "Measurements of wavelength dependent scattering and backscattering coefficients by low-coherence spectroscopy", *Journal of Biomedical Optics*, **16**(3), 030503 (2011)
- N. Bosschaart, R. Mentink, J.H. Kok, T.G. van Leeuwen, M.C.G. Aalders, "Optical properties of neonatal skin measured *in vivo* as a function of age and skin pigmentation", *Journal of Biomedical Optics* **16**(9), 097003 (2011)
- N. Bosschaart, D.J. Faber, T.G. van Leeuwen, M.C.G Aalders, "*In vivo* low-coherence spectroscopic measurements of local hemoglobin absorption spectra in human skin" *Journal of Biomedical Optics* **16**(10), 100504 (2011)
- N. Bosschaart, J.H. Kok, A.M. Newsum, D.M. Ouweneel, R.M. Mentink, T.G. van Leeuwen, M.C.G. Aalders, "Limitations and opportunities of transcutaneous bilirubin measurements", *Pediatrics* **129**(4), in press (2012)
- N. Bosschaart, D.J. Faber, M.C.G. Aalders, T.G. van Leeuwen, "Spectroscopic detection in low-coherence spectroscopy", in preparation

Summary

Due to underdeveloped organ functions at birth, preterm neonates have an increased risk on developing jaundice. Jaundice (hyperbilirubinemia) is related to elevated bilirubin concentrations in blood and may result in brain damage (kernicterus) if bilirubin levels rise to levels that cause extravasation of bilirubin through the blood-brain barrier. It is therefore essential to accurately monitor bilirubin levels in jaundiced neonates.

The current gold standard to measure bilirubin levels is invasive blood sampling, commonly by a heel stick, which may be needed up to 3 times a day. Subsequent laboratory analysis of the blood sample provides the total blood, or serum bilirubin concentration (TSB). Naturally, this is a very painful and stressful procedure for the neonate. In addition, the method is laborious and time consuming, lacking the possibility for immediate diagnosis.

A possible alternative for invasive blood sampling is transcutaneous bilirubinometry, which is a non-invasive and painless method that provides an instantaneous read-out of the cutaneous bilirubin concentration (TcB). Transcutaneous bilirubinometry is based on optical spectroscopy, which relates the amount of light absorption around 460 nm by bilirubin in the skin (i.e. the yellow color of the skin) to the concentration of bilirubin in blood. Although bilirubinometers based on this principle have been developed since 1980, no device has been found accurate enough to completely replace the heel stick. The focus of this thesis is therefore 1) to investigate the reasons for the limited accuracy of current bilirubinometers and 2) to design a bilirubinometer that can replace invasive blood sampling.

To investigate the reasons for the limited accuracy of current bilirubinometers, we built a transcutaneous bilirubinometer that determines not only the TcB, but also the blood volume fraction (BVF) in the investigated skin volume. In an exploratory patient study, we found that the TcB consists primarily (>99%) of bilirubin in the tissue *surrounding* the blood vessels in the skin, instead of bilirubin inside the blood vessels themselves. Since the bilirubin concentration in the surrounding tissue is difficult to relate to the concentration in blood (TSB), this introduces an inevitable inaccuracy in the comparison of existing bilirubinometers to the heel stick determination (Chapters 1 and 2).

One way to solve this problem is by designing a transcutaneous bilirubinometer that excludes the influence of the surrounding skin tissue, i.e. a bilirubinometer that can confine its probing volume to the inner lumen of a blood vessel only. Current spectroscopic techniques are unable to do such a determination, since light scattering from the surrounding tissue always contributes to the measured value. Therefore, we developed a new spectroscopic technique – low coherence spectroscopy (LCS) – which, based on low coherence interferometry, allows for very careful control over the size and location of the investigated tissue volume (axial x lateral resolution: 22 μm x 9 μm).

When designing a new optical technique for measurements on neonatal skin, knowledge on the optical properties of neonatal skin is required. Therefore, we used

the bilirubinometer from our patient study also for the determination of the optical properties of neonatal skin, as described in Chapter 3.

The remaining Chapters 4 to 7 of this thesis describe the development and validation of LCS. This validation involves the demonstration of 1) that we can use LCS for the *quantitative* determination of absorption coefficient spectra μ_a , which is needed to derive chromophore concentrations such as bilirubin and 2) that we can use LCS for the *localized* determination of μ_a , which is needed for confining the measurement volume to a single blood vessel.

In Chapter 4, we demonstrate that LCS can quantitatively measure μ_a in tissue simulating phantoms from which the exact optical properties are known. Since LCS measures the total attenuation coefficient of the sample – which is the sum of the scattering and absorption coefficient – knowledge of the contribution of scattering to the LCS signal is important for accurate measurements of μ_a . Therefore, scattering contributions to the LCS signal are investigated in Chapter 5.

The localized determination of μ_a is validated in Chapter 6 on layered tissue simulating phantoms. In addition to these phantom measurements, the first *in vivo* results for LCS are demonstrated on human skin, from which the μ_a and chromophore concentrations are determined within distinct skin volumes (the dermal and the epidermal layer). The measured concentration of the chromophore hemoglobin in the dermis is comparable to normal hemoglobin concentrations found in human skin, as is the oxygen saturation that was derived from the hemoglobin absorption.

To enhance the clinical value of LCS, improvements on the acquisition speed and accuracy may be needed. Therefore, Chapter 7 describes the possibility of replacing the time domain detection scheme of our current LCS system by spectroscopic detection, which provides a theoretical speed and/or sensitivity advantage.

In summary, this thesis describes the essential first steps in the design, development and validation of LCS as a potential non-invasive alternative for invasive bilirubin measurements. Before LCS can be clinically applied for this purpose, future research is needed, primarily on the optimization of the suggested configuration for spectroscopic detection. Nevertheless, even at this early stage of development, we can already show that the current time domain LCS system can be used for measuring the μ_a within a single blood vessel in human skin, and that the derived hemoglobin concentration is well within the range of normal human whole blood hemoglobin concentrations (Chapter 8). Therefore, LCS is a very promising technique that deserves further development and can potentially lead to less pain and complications for preterm neonates.

Samenvatting

Te vroeg geboren babies hebben een verhoogde kans op het ontwikkelen van geelzucht, omdat hun orgaanfuncties bij de geboorte nog niet volledig ontwikkeld zijn. Geelzucht ontstaat doordat er te veel bilirubine (een lichaamseigen, gele stof) aanwezig is in het bloed en in de huid, waardoor de huid geel kleurt. Het is erg belangrijk om de bilirubinewaarde goed in de gaten te houden, want bij te hoge bilirubinewaarden kan er hersenschade (kernicterus) optreden.

Om de bilirubinewaarde te meten is een bloedmonster nodig, dat in de meeste gevallen wordt afgenomen door middel van een hielprik – soms tot wel drie keer per dag. Vervolgens wordt het bloedmonster in het lab geanalyseerd, waarbij de totale serum bilirubineconcentratie (TSB) bepaald wordt. Vanzelfsprekend is dit een pijnlijke en schadelijke procedure voor de patiënt. Daarnaast eist de methode veel tijd en personeel, waardoor het onmogelijk is om de bilirubinewaarde continu te meten.

Een mogelijk alternatief voor de hielprik is transcutane bilirubinometrie: een niet-invasieve methode die snel en pijnloos de bilirubinewaarde in de huid (TcB) meet. Transcutane bilirubinometrie is gebaseerd op optische spectroscopie, waarbij de hoeveelheid licht die rond 460 nm wordt geabsorbeerd in de huid (de 'gele kleur' van de huid) wordt gerelateerd aan de bilirubinewaarde in bloed. Al sinds 1980 worden er bilirubinometers ontwikkeld die gebaseerd zijn op dit principe, maar tot nu toe is nog geen enkel apparaat nauwkeurig genoeg gebleken om de hielprik volledig te vervangen. Het doel van dit proefschrift is daarom 1) om te onderzoeken waarom de huidige bilirubinometers een beperkte nauwkeurigheid hebben en 2) om een bilirubinometer te ontwerpen die de hielprik wél kan vervangen.

Om te onderzoeken waarom de huidige bilirubinometers een beperkte nauwkeurigheid hebben, ontwikkelden we zelf een transcutane bilirubinometer die niet alleen de TcB kan meten, maar ook de bloedvolume fractie (BVF) in het gemeten huidvolume. Uit een verkennende patientenstudie bleek dat de gemeten TcB-waarde voornamelijk bestaat uit de bijdrage van bilirubine die zich *rondom* de bloedvaatjes in de huid bevindt (>99%), in plaats van in de bloedvaatjes zelf. Omdat de bilirubineconcentratie rondom de bloedvaatjes (TcB) moeilijk te herleiden is tot de bilirubineconcentratie in het bloed (TSB), ontstaat er een onvermijdelijke onnauwkeurigheid wanneer de TcB vergeleken wordt met de TSB (Hoofdstuk 1 en 2).

Een manier om dit probleem op te lossen, is door de bilirubinometer zó te ontwerpen, dat alleen de bilirubinewaarde in de vaatjes wordt gemeten – bijvoorbeeld door het meetvolume van de bilirubinometer te beperken tot het binnenste van één enkel bloedvat. De bestaande spectroscopische technieken kunnen hier niet voor worden gebruikt, omdat de verstrooiing en absorptie van licht in het weefsel rondom de vaatjes altijd de meting beïnvloedt. Daarom hebben we een nieuwe spectroscopische techniek ontwikkeld – laag coherente spectroscopie (LCS) – die, gebaseerd op laag-coherente interferometrie, heel nauwkeurig de grootte en de locatie van het gemeten weefselvolume kan regelen (axiale x laterale resolutie: 22 μm x 9 μm).

Bij het ontwikkelen van een nieuwe optische techniek voor metingen op babyhuid is het belangrijk om gedegen kennis te hebben van de optische eigenschappen van babyhuid. Daarom hebben we de bilirubinemeter van de patientenstudie tevens gebruikt om deze optische eigenschappen te bepalen (hoofdstuk 3).

De overige hoofdstukken (4 tot 7) van dit proefschrift beschrijven de ontwikkeling en de validatie van LCS. Deze validatie houdt onder andere in 1) dat we LCS kunnen gebruiken voor de *kwantitatieve* bepaling van absorptiecoëfficiëntspectra μ_a , omdat we daar concentraties van chromoforen (licht-absorberende stoffen, zoals bilirubine) uit kunnen herleiden en 2) dat we LCS kunnen gebruiken voor de *gelocaliseerde* bepaling van μ_a , omdat we het meetvolume willen kunnen beperken tot één enkel bloedvat.

Om te beginnen laten we in hoofdstuk 4 zien dat LCS inderdaad gebruikt kan worden voor de kwantitatieve bepaling van μ_a . Dat doen we met behulp van 'weefselfantomen': een stof met ongeveer dezelfde optische eigenschappen als babyhuid, maar waarvan we heel precies weten welke μ_a de stof heeft, zodat we kunnen controleren of de meting klopt.

LCS meet niet direct de μ_a in het weefsel, maar het attenuatiecoëfficiëntspectrum: de som van het absorptie, en verstrooiingscoëfficiëntspectrum. Voor een goede bepaling van de μ_a is het daarom belangrijk om te weten wat de invloed is van de weefselverstrooiing op de meting. Ook dit hebben we onderzocht met behulp van weefselfantomen, zoals beschreven in hoofdstuk 5.

Dat LCS gelocaliseerd de μ_a kan meten, laten we zien in hoofdstuk 6, waarbij we de optische eigenschappen van gelaagde weefselfantomen bepalen. In dit hoofdstuk laten we ook de eerste *in vivo* ('in het lichaam') meting zien van LCS op mensenhuid. Bij deze *in vivo* meting tonen we aan dat LCS de μ_a kan bepalen in verschillende huidlagen en dat uit de μ_a de concentratie van het chromofoor hemoglobine (de rode stof in bloed) bepaald kan worden. De gemeten hemoglobineconcentratie is vergelijkbaar met de normale waarden voor hemoglobineconcentraties in de huid, evenals de zuurstofsaturatie die we uit de absorptie van hemoglobine kunnen herleiden.

Om de klinische waarde van LCS verder te verbeteren zijn er wellicht aanpassingen nodig aan de snelheid en de gevoeligheid van het huidige systeemontwerp. Daarom beschrijven we in hoofdstuk 7 de mogelijkheid om de huidige 'tijd domein' detectiemethode te vervangen door spectroscopische detectie, wat theoretisch een voordeel oplevert in meetsnelheid en/of gevoeligheid.

Als samenvatting van de samenvatting: dit proefschrift beschrijft de essentiële eerste stappen in het ontwerp, de ontwikkeling en de validatie van de nieuwe techniek LCS als een mogelijk alternatief voor de hieprijk. Meer onderzoek is nodig voordat LCS hier daadwerkelijk voor gebruikt kan worden. Desondanks kunnen we zelfs in dit vroege ontwikkelingsstadium van de techniek al laten zien dat we LCS kunnen gebruiken voor de bepaling van de μ_a in één enkel bloedvat in de huid, en dat de hemoglobineconcentratie die daaruit bepaald wordt goed klopt met normale hemoglobineconcentraties in bloed (hoofdstuk 8). Daarom is LCS een veelbelovende techniek die het waard is om verder ontwikkeld te worden, zodat te vroeg geboren babies uiteindelijk minder pijn en complicaties hebben bij de bepaling van hun bilirubinewaarde.

Dankwoord

Ik ben een aantal mensen oprecht heel erg dankbaar voor hun bijdrage aan de tot stand koming van dit proefschrift, in welke vorm dan ook. Tijdens het overgrote deel van de afgelopen vier jaar heb ik volop kunnen genieten, wat mede mogelijk gemaakt is door:

Maurice. Dankjewel voor je begeleiding, je goede ideeën en je enthousiasme. Ik heb ontzettend veel van je geleerd en – ook al deed je me er soms aan twijfelen – na vier jaar heb ik nog steeds bloed onder mijn nagels zitten (Figuur 8.1)!

Ton. Heel erg bedankt voor dat je me attendeerde op dit onderzoek, het vertrouwen dat je in me had en natuurlijk ook jouw begeleiding. Je was een van de eersten die mij liet kennismaken met de biomedische optica, en daar ben ik nog steeds blij om.

Dirk. Bedankt voor al je goede ideeën bij de ontwikkeling van LCS en daar omheen. Speciaal voor jou een flauwe woordgrap: mede dankzij jouw bijdrage hebben we er zo'n coherent geheel van kunnen maken!

Joke Kok. Ontzettend bedankt voor je bijdrage aan de klinische kant van dit verhaal. De samenwerking met de neonatologie verliep altijd soepel, wat natuurlijk ook mogelijk gemaakt werd door de inspanningen van Sabine Beuger, Debbie Nuytemans en alle betrokken verpleegkundigen en artsen. Allemaal bedankt!

Rosaline, Astrid, Dagmar. Ik had me geen betere stagiaires kunnen wensen. Bedankt voor al het vroege opstaan, het enthousiasme en de zorgvuldigheid waarmee jullie de patiëntmetingen hebben gedaan. Het was erg leuk om met jullie samen te werken. Jelmer. Jij was natuurlijk ook een geweldige stagiair en collega. Je vertrek blijft een gemis.

Niet onbelangrijk: alle patiënten van de neonatologie die deel hebben genomen aan de patiëntenstudie en hun ouders. Dankzij jullie zijn we weer een stapje dichterbij een beter leven voor toekomstige babies.

Dat geldt natuurlijk ook voor alle anderen die (een deel van) hun lichaam beschikbaar hebben gesteld aan dit onderzoek – dankjewel!

Lieve Bar, Annie, Merel, Lida – laserbabes – bedankt voor de enorme gezelligheid en afleiding tijdens en na het werk. Zonder jullie is de BEPH maar jurkloos. Gelukkig liggen er nog talloze dagjes Antwerpen/Sydney/... in de toekomst!

Duc! Thank you for feeding me. And thank you for breaking the silence every once in a while with candle light music and your inspiring views on Dutch/Vietnamese culture. You have been a wonderful roommate!

Nogmaals Barbara en Rosaline! Dankjewel dat jullie de zware taak van het paranimfschap op jullie hebben genomen. En Bar, dankjewel voor de lasagne – ik hoop niet dat ik hem terug hoef te geven.

Daarnaast natuurlijk alle andere collega's van de afdeling Biomedical Engineering & Physics. Bedankt voor alle gezelligheid, koffieautomaatgesprekken, lunches, uitjes en de momenten waarop jullie meedachten bij dit onderzoek. Martijn, ik vind het onwijs gezellig dat we voorlopig nog naast elkaar werken en Roy, ik hoop dat je nog even door gaat met het volgen van mij. Vitali, het was uitmuntend om het licht met jou te mogen delen. Rolf, bedankt voor al je tips rondom de afronding van een promotie en Jeroen (damkampioen), je bent inmiddels een verre buur maar een goede vriend. Angela, het was geweldig om met jou en Annie het uitje te organiseren en Judith, het was supergaaf om samen met jou te zingen! En natuurlijk iedereen die in de kelder zit: Edwin, Gerda, Jasmin, Annemieke en Saskia, het is altijd een feestje om jullie serene oase van rust binnen te lopen en een kopje thee te drinken. Martin van Gemert en Jeroen Kalkman, jullie ook bedankt voor alle adviezen en interesse in dit onderzoek. Tenslotte Jetty: zonder jou achter de schermen zouden maar weinig van ons promoveren.

Het is ook ontzettend fijn om af en toe eens niet met je onderzoek bezig te zijn. Ik wil al mijn (schoon)familie, vriendinnen en vrienden bedanken voor hun steun, interesse, wijze woorden en bijdrage aan het doen van dingen die hier helemaal niets mee te maken hebben. Lieve Saskia, Heleen, Simone, Marije, Charlotte, Ingeborg, Renske, mannen+Ciska, broers, Afke, veel van de bovengenoemden en nog meer ongenoemden: ik zou nog wel een heel boek vol kunnen schrijven met waar ik jullie allemaal dankbaar voor ben.

Papa en mama, bedankt voor jullie onvoorwaardelijke steun en vertrouwen, en dat jullie het zo leuk vinden wat ik doe.

En Ronald, natuurlijk. Met jou is alles sowieso leuker.

Nienke

Curriculum vitae

Nienke Bosschaart was born on April 17th 1984 in Grootebroek, The Netherlands. After finishing the Gymnasium at the Martinuscollege in Grootebroek, she moved to Enschede (The Netherlands) to study Biomedical Engineering at the University of Twente. She obtained her Bachelor degree in 2005, which included a research thesis on *Photoacoustic imaging of venous valves in superficial veins*. During her Master education in Biomedical Engineering, she went to the University of L'Aquila (Italy) for three months to study muscle oxygenation with near-infrared spectroscopy. She conducted part of the research for her master graduation thesis on *Combining Raman spectroscopy and optical coherence tomography for the non-invasive evaluation of skin cancer* at Vanderbilt University (Nashville TN, USA) and graduated in November 2007. In December 2007, she started her PhD at the Academic Medical Center of the University of Amsterdam, which resulted in this thesis. For her PhD work, she received the Simon Stevin Leerling award 2010.